MASTER THESIS

Herr
Martin Kürbis

On Aspects of Massive MIMO Under Realistic Propagation Conditions and in Internet of Things Scenarios

2017

MASTERARBEIT

On Aspects of Massive MIMO Under Realistic Propagation Conditions and in Internet of Things Scenarios

Autor:

Martin Kürbis

Studiengang:
Elektro - und Informationstechnik

Seminargruppe:
ET15w1-M

Erstprüfer:
Prof. Dr.-Ing. Alexander Lampe

Zweitprüfer:
Prof. Dr.-Ing. Lutz Lampe (University of British Columbia, Canada)

Mittweida, 2017

Referat

Massive multiple-input multiple-output (MIMO), eine Technik bei der die Basisstation einer Mobilfunkzelle mit einer großen Anzahl an Antennen ausgestattet ist, wird derzeit als eine vielversprechende Schlüsseltechnologie zur Erfüllung der Anforderungen zukünftiger drahtloser Kommunikationsnetze der fünften Generation betrachtet. Die zuversichtlichen Angaben über die Leistung solcher Systeme beruht allerdings auf einer theoretischen, bisher kaum praktisch verifizierten Annahme, dass die drahtlosen Übertragungskanäle verschiedener Nutzer aufgrund der hohen Anzahl an Antennen voneinander unabhängig sind. Das heißt, dass sogenannte *günstige Übertragungsbedingungen* herrschen. Die vorliegende Masterarbeit untersucht diese neuartigen Systeme unter zwei verschiedenen Perspektiven.

Im ersten Teil dieser Arbeit wird der Einfluss von realistischen Übertragungsbedingungen auf die Performance von massive MIMO Systemen evaluiert. Dazu werden entsprechende numerische Systemsimulationen durchgeführt und mit den Ergebnissen von praktischen massive MIMO Messkampagnen verglichen. Die Untersuchungen ergeben, dass die sogenannten günstigen Übertragungsbedingungen in realistischen Umgebungen nur bedingt beobachtet werden können. Daher führen traditionelle Kanalmodelle zu einer ungenauen Abschätzung der Leistung von praktischen massive MIMO Systemen. Um diesem Problem zu begegnen, wird deshalb eine neuartige Parametrisierung des traditionellen Kronecker-Modells vorgeschlagen, sodass relevante Kenngrößen realistischer Kanäle mit diesem Modell präzise widergespiegelt werden. Anschließend folgt eine Untersuchung verschiedener Methoden zur Kanalschätzung in massive MIMO Systemen unter den verschiedenen Kanalmodellen mittels numerischer Simulationen. Die Experimente zeigen auf, dass Schätzmethoden, welche speziell für massive MIMO unter der Annahme von günstigen Übertragungsbedingungen hergeleitet wurden, eine signifikante Leistungsminderung unter realistischen Kanalmodellen erfahren.

Im zweiten Teil dieser Arbeit liegt der Fokus auf der Anwendung von massive MIMO Systemen in sogenannten Internet of Things (IoT) Netzwerken. Die typischerweise hohe Anzahl an aktiven IoT-Geräten macht die Anwendung von effizienten Scheduling-Algorithmen notwendig. Daher wird ein Downlink-Scheduling-Algorithmus präsentiert, welcher sich die Eigenschaften von massive MIMO Systemen und die typischen Anforderungen an die Datenraten von IoT-Geräten zunutze macht. Im Speziellen wird vorgeschlagen, die IoT-Nutzer in Gruppen aufzuteilen und die verschiedenen Gruppen nacheinander zu versorgen. Die Gruppengröße wird dabei mit Hilfe asymptotischer Eigenschaften von massive MIMO Systemen hergeleitet. Um die Gruppenmitglieder zu selektieren, wird eine modifizierte Version des populären Semi-Orthogonal-User-Selection (SUS) Algorithmus vorgeschlagen. Die anschließend durchgeführten numerischen Simulationen bestätigen, dass die modifizierte Version von SUS die Nachteile des originalen Algorithmus eliminiert, was wiederum zu verbesserten Datenraten in dem betrachteten System führt.

Abstract

Massive multiple-input multiple-output (MIMO) transmission is considered as a promising key technology fulfilling the requirements of future wireless communication systems of the fifth generation. The auspicious performance predictions of such systems, however rely on so called *favourable propagation conditions*, which means that the channels of the users are independent of each other due to the large number of antennas at the base station. This thesis investigates such novel systems from two different perspectives.

In the first part of this work, the influence of realistic propagation conditions on the performance of massive MIMO systems is evaluated. To this end, important characteristics of different channel models available in literature are evaluated by means of numerical simulations. The comparison of these results with data from practical measurement campaigns indicate that favourable propagation conditions are not always a property of realistic environments. Therefore, traditional channel models lead to inaccurate performance estimates for practical massive MIMO systems. In order to overcome this issue, a new parameterization of the well-known Kronecker model is proposed, which enables an accurate modelling of important characteristics of realistic propagation environments. Subsequently, the influence of the underlying channel model on various channel estimation techniques in massive MIMO systems is studied by means of numerical simulations. The experiments demonstrate that estimation techniques specifically designed for massive MIMO systems experience a performance degradation under realistic channel models.

In the second part ot this thesis, the focus is on the application of massive MIMO transmission in so-called Internet of Things (IoT) networks. The typically high number of IoT devices requires the application of efficient user scheduling algorithms. Thus, a downlink scheduling algorithm is presented, which exploits special properties of massive MIMO systems and IoT devices. In particular, it is proposed to serve the IoT devices consecutively in groups, where the group sizes are derived by means of asymptotic properties of massive MIMO systems. To select the group members, a modified version of the popular semi-orthogonal user selection algorithm is proposed. The performed numerical simulations demonstrate that the modified version of the algorithm eliminates the shortcomings of its original counterpart which leads to improved sum rate performance in the system.

Contents

List of Abbreviations

BS

Base Station

CDF

Cumulative Distribution Function

DFT

Discrete Fourier Transform

FLOPS

Floating Point Operations

i.i.d.

independent identical distributed

IoT

Internet of Things

JGS

Joint Grouping And Scheduling

LS

Least Squares

MIMO

Multiple-Input Multiple-Output

MMSE

Minimum Mean Square Error

MPC

Multi Path Component

MTC

Machine-Type Communication

NMSE

Normalized Mean Squared Error

OFDM

Orthogonal Frequency-Divison Multiplexing

PEACH

Polynomial Expansion Channel Estimator

SINR

Signal-to-Interference-Plus-Noise Ratio

SNR

Signal-to-Noise Ratio

SUS

Semi-Orthogonal User Selection

SVS

Singular Value Spread

TDD

Time-Division Duplex

UE

User Equipment

ZFBF

Zero-Forcing Beamforming

ZFS

Zero-Forcing Beamforming with User Selection

1 Introduction

1.1 Motivation and Goals

Within the last couple of years, we have witnessed rapid developments and tremendous advancements in the electronic and computer industry. As a result, electronic devices are nowadays prevalent in virtually every aspect of life in our modern society. Recently, a new trend is to equip the devices with more powerful processors and transceivers for wireless communication which facilitates the integration of all these devices into a wide-reaching information processing network [1]. Such networks will enable the automation and remote control of processes in industry, traffic, and our daily life at home, thereby improving the productivity of industry and society [2].

The envisioned interconnection of sensors, actuators and other information processing devices to the so-called Internet of Things (IoT) necessitates new powerful communication infrastructures and is an integral part in the development of new fifth generation (5G) cellular networks [3–5]. In IoT scenarios, the cells of a wireless communication system are expected to be densely populated by a very large number of IoT devices [3,4,6]. For instance the authors in [4] state that up to $480\,000$ devices might be served by one Base Station (BS). In order to manage the challenges arising from such a large number of devices, massive Multiple-Input Multiple-Output (MIMO) transmission is considered as a promising candidate for future cellular wireless communication systems as it allows spatial multiplexing of a significant number of users [7]. In theoretical studies, it has been shown that massive MIMO systems are capable to arbitrarily increase the system performance by adding more and more antennas at the BS [8–10]. Recently, investigations of massive MIMO systems in practical experiments revealed, that theoretic performance predictions of such systems are often too optimistic and deviate from the performance of such systems measured under practical conditions [11–13].

In this thesis, we aim to study massive MIMO systems under two different aspects. Our first goal is to analyze the influence of realistic propagation conditions on the performance of massive MIMO systems. As a second goal, we apply massive MIMO transmission in an IoT systems and investigate methods to manage the new challenges arising from the very large number of devices which gain access to the communication infrastructure in such systems.

1.2 Outline and Contributions of Thesis

The work presented in this thesis is divided into two main parts. In Chapter 2 and Chapter 3 we study typical properties of practical massive MIMO propagation environments and their influence on the system performance. The second part presented in Chapter 4 of this thesis focuses on downlink user scheduling in massive MIMO IoT systems.

In Chapter 2 we first introduce the concepts of various well established channel models which are typically used for the evaluation of massive MIMO systems. As a fist contribution of this thesis, we introduce a parameterization of the well-known Kronecker model which we derive based

on the properties of real-world propagation environments. Then, we present a detailed comparison of different channel modelling approaches under massive MIMO configurations in terms of system-level parameters such as correlation among the user channels and achievable sum rates. This comparison constitutes the second main contribution of Chapter 2 and provides important insights on channel modelling for realistic massive MIMO systems. In Chapter 3 we investigate the influence of the underlying channel models on the performance of massive MIMO channel estimation techniques. We evaluate traditional and massive MIMO-specific techniques in a multi-cell environment and draw conclusions about the impact of the underlying channel model on the individual estimators.

In the second main part of our thesis presented in Chapter 4, we propose a new fair user scheduling algorithm for the downlink in massive MIMO IoT systems. The suggested strategy serves all the users in the cell by means of user grouping. For our derivations, we exploit asymptotic properties of massive MIMO systems and typical characteristics of IoT devices. Our new approach also eliminates flaws of a popular user scheduling algorithm which occur when operating under massive MIMO systems. Performed numerical simulations demonstrate that our proposed methods exhibits very competitive performance compared to existing strategies.

1.3 Notation

In our thesis, we use boldface small letters for vectors, boldface capital letters for matrices and calligraphic letters for sets. We refer to the i-th element of a vector $\boldsymbol{a}$ with $a[i]$ and to the entry of a matrix $\boldsymbol{A}$ in row i and column j with $A[i,j]$. We denote with $(\cdot)^T$, $(\cdot)^H$ and $(\cdot)^*$ the transpose, the complex conjugate transpose and the complex conjugate of a matrix or vector. Moreover, the inverse and pseudo-inverse of a matrix is indicated by $(\cdot)^{-1}$ and $(\cdot)^\dagger$, respectively. The symbol $\boldsymbol{I}_K$ denotes the identity matrix of size K.

2 Channel Models

Massive MIMO transmission is considered a key technology driving the 5G evolution, which improves the network performance by employing a large number of antennas at the BS. A key component in the evaluation of massive MIMO systems is the underlying channel model. In many theoretical works, uncorrelated channels which facilitate an analytic examination of the system are considered. However, such models do not necessarily reflect the properties of true propagation channels which can results in misleading conclusions about the performance of massive MIMO systems. This chapter provides an overview of different channel models commonly used in massive MIMO related literature and characterizes the models based on their proximity towards massive MIMO measurement campaigns. As a result of the investigations, a channel model with only two parameters is proposed, which accurately models realistic propagation environments from a system-level perspective.

Selected parts of this chapter were published in [14] in the framework of the 24th European Signal Processing Conference 2016 in Budapest, Hungary.

2.1 Fundamentals of Channel Models

Wireless data transmission between two devices is performed by the emission and reception of electromagnetic waves. The information subject to transmission is imposed on the waves by means of some modulation scheme. While travelling from transmitter to receiver, the electromagnetic waves pass a so-called channel which is determined by the physical environment in which the wireless signals propagate. The achievable performance of such a communication system is fundamentally determined by the underlying propagation channel which renders channel modelling a crucial part of the system design [15, 16]. In the following, we will introduce some basic notions of channel modelling required to understand the work presented in this chapter.

2.1.1 What Are Wireless Channels?

Physical propagation of electromagnetic waves carrying the transmit signals is a very complex process as it is the result of various phenomena such as reflection, refraction, diffraction and scattering [13]. In general, the electromagnetic waves interact with a number of objects, so-called scatterers, in the propagation environment while travelling from transmitter to receiver. From a physical point of view, scatterers represent objects, such as trees, buildings, walls or people, which cause the above mentioned distortions to the propagating signal. Due to the interaction with the scatterers, multiple distorted copies of the original signal are detected at the receiver. This principle is illustrated in Fig. 2.1. It is clear from the figure, that each detected copy travelled along its individual path from transmitter to receiver. Thus, we will hereafter refer to one such copy as *Multi Path Component (MPC)*. It is evident that the number of received copies and their distortions strongly depend on the respective propagation environment (i.e. the channel), which renders uni-
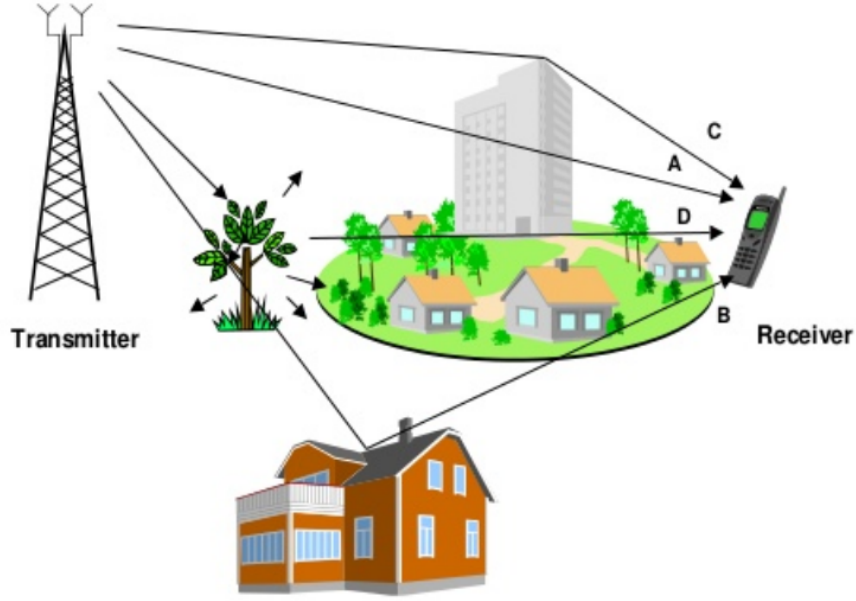
Figure 2.1: Schematic illustration of physical phenomena of electromagnetic wave propagation.
Figure adopted from [17].

versal and accurate modelling of electromagnetic wave propagation in practical environments a challenging task.

From a signal processing point of view, the wireless channel is modelled as a linear filter [13]. The signals transmitted at the receiver are distorted by the channel before they arrive at the receiver unit. Typically, such distortions manifest in delays, amplitude changes, and frequency offsets of the received signals [13]. In this thesis, we will only consider frequency-flat channels in which the fading process is constant over the entire bandwidth of the channel. We remark, that frequency-flat fading is a strong assumption, especially when large bandwidths are used for data transmission. However, a frequency-selective wide band channel can be divided into multiple frequency-flat narrow band channels by means of Orthogonal Frequency-Divison Multiplexing (OFDM). Consequently, our restriction to frequency-flat channels does not constitute a limitation of practical relevance of our presented work. Moreover, we remark that our assumption is in alignment with the majority of the references consulted in the remainder of this thesis.

Let us now consider the data transmission in the downlink of the communication system, i.e., when data is transmitted from the BS equipped with M antennas to the K User Equipments (UEs). To this end, we formally describe the relationship between transmitted and received signal as

$$\boldsymbol{y} = \sqrt{\gamma}\boldsymbol{H}\boldsymbol{x} + \boldsymbol{n}, \tag{2.1}$$

where $\boldsymbol{y}, \boldsymbol{n} \in \mathbb{C}^{K \times 1}$ is the signal received at the K UEs and the additive white Gaussian noise with unit variance, i.e., $\boldsymbol{n} \sim \mathcal{CN}(\boldsymbol{0}, \boldsymbol{I}_K)$, respectively. Moreover, the transmit signal $\boldsymbol{x} \in \mathbb{C}^{M \times 1}$ is assumed to have unity transmit power, i.e. $\mathbb{E}(\boldsymbol{x}^H \boldsymbol{x}) = 1$, $\boldsymbol{H} \in \mathbb{C}^{K \times M}$ denotes the channel matrix and $\gamma \in \mathbb{R}$ is a scalar scaling the transmit power at the BS. Here, $\boldsymbol{H}$ contains the channel coefficients between the K UEs and the M antennas at the BS and models the above mentioned physical effects experienced by the signal $\boldsymbol{x}$ when travelling from transmitter to receiver. Consequently, as a result of the channel modelling procedure, we aim to obtain a policy to artificially generate the entries of $\boldsymbol{H}$ such that the distortions of the transmit signal occurring in realistic environments are reflected

by the multiplication of $\boldsymbol{x}$ with $\boldsymbol{H}$. We note that the transmission model in (2.1) describes the data transmission from a system-level perspective and does not cover all physical aspects of wireless signal propagation. This, however, is not a restriction since our studies focus on algorithmic aspects of massive MIMO communication systems for which (2.1) contains the relevant information (cf. with the modelling assumptions made in references cited in this thesis).

A key property of $\boldsymbol{H}$ when evaluating communication systems described in Eq. (2.1) is the channel capacity, which measures the maximum information which can be inferred from an observation vector $\boldsymbol{y}$ (received signal) about the unknown variables in $\boldsymbol{x}$ (transmitted signal). The capacity of $\boldsymbol{H}$ is formally defined as [8]

$$C = I(\boldsymbol{y}, \boldsymbol{x}) = \log_2 \det\left(\boldsymbol{I}_K + \gamma \boldsymbol{H}\boldsymbol{H}^H\right), \tag{2.2}$$

where $I(\boldsymbol{y}, \boldsymbol{x})$ denotes the mutual information operator.[1] The channel capacity is a fundamental metric determining the performance of the wireless communication systems and it is a property of the underlying propagation environment. We remark that the channel capacity is determined by the singular values of $\boldsymbol{H}$. To see this, we write the singular value decomposition of $\boldsymbol{H}$ as

$$\boldsymbol{H} = \boldsymbol{U}\boldsymbol{\Sigma}\boldsymbol{V}^H, \tag{2.3}$$

where $\boldsymbol{U} \in \mathbb{C}^{K \times K}, \boldsymbol{V} \in \mathbb{C}^{M \times M}$ are unitary matrices and $\boldsymbol{\Sigma} \in \mathbb{C}^{K \times M}$ is a matrix with the singular values $\sigma_1, \geq \ldots, \sigma_K \geq 0$ of $\boldsymbol{H}$ on its diagonal. Plugging (2.3) into (2.2) gives

$$\begin{aligned} C &= \log_2 \det\left(\boldsymbol{I}_K + \gamma \boldsymbol{U}\boldsymbol{\Sigma}\boldsymbol{\Sigma}^H\boldsymbol{U}^H\right) \\ &= \log_2 \det\left[\boldsymbol{U}\left(\boldsymbol{I}_K + \gamma \boldsymbol{\Sigma}\boldsymbol{\Sigma}^H\right)\boldsymbol{U}^H\right]. \end{aligned}$$

Since $\det(\boldsymbol{A}\boldsymbol{B}) = \det(\boldsymbol{A})\det(\boldsymbol{B})$ and the determinant of a unitary matrix is one, we can rewrite the capacity as

$$\begin{aligned} C &= \log_2 \det\left(\boldsymbol{I}_K + \gamma \boldsymbol{\Sigma}\boldsymbol{\Sigma}^H\right) \\ &= \sum_{k=1}^{K} \log_2\left(1 + \gamma \sigma_k^2\right). \end{aligned} \tag{2.4}$$

While channel models are required to investigate the performance of wireless communication systems, they also constitute an important tool for system design, such as the development of precoding and detection algorithms, as well as testing and standardization of wireless communication technologies [18]. Consequently, depending on the purpose of the model, certain features of physical propagation channels are more important than others. This led to the development of different approaches to wireless channel modelling which are outlined next.

2.1.2 Types of Channel Models

Two fundamentally different types of channel models are found in literature, namely analytical and physical models [19]. While analytical models describe the radio channel mathematically in an abstract manner, physical channel models aim to reconstruct the actual propagation characteristics of electromagnetic waves. We will briefly describe the main principle of both modelling approaches

---

[1]Note that the given definition of the capacity assumes that no power allocation is adopted at the BS.

in the sequel.

Analytic Models

Analytic channel models describe the propagation environment by means of closed-form expressions which generate the coefficients of $\boldsymbol{H}$. In literature, there exist two categories of such models, namely propagation-based and correlation-based models [19]. While the former ones make use of actual physical propagation parameters, such as directions and delays of signals, the latter ones generate the channel coefficients based on statistical distributions only. Examples for propagation-based models are Clarke's Model and the virtual channel representation, whereas the Kronecker and Weichselberger models are typical representatives of correlation-based models [19].

Analytical channel models are widely adopted for the purpose of theoretical evaluation of wireless communication systems [20]. This can be explained by the fact that such models are mathematically tractable and an entire communication system can be easily simulated numerically due to the low model complexity. However, analytical models do not accurately reflect physical properties of wireless signal propagation. In particular, the models usually require that the plane wave front assumption holds true. While this is the case in conventional MIMO systems where the antenna arrays have small physical dimensions, this assumption can not be used in massive MIMO systems [11, 21]. To understand this, we remark that the plane wave front assumption can only be adopted if the UEs and the scatterers are located outside the Rayleigh distance (i.e. in the far-field) of the antenna array [13]. The Rayleigh distance of the antenna array is dependent on the physical dimensions according to

$$d_{\text{Rayleigh}} = \frac{2D_{\text{B}}^2}{\lambda},$$

(2.5)

where D_{B} is the largest physical dimension of the antenna array and λ denotes the wave length of the carrier frequency [13]. To give an example, we assume a carrier frequency of 2.1 GHz which corresponds to a wave length of $\lambda = 0.15$ meters and a linear antenna array with $M = 64$ antennas spaced $\lambda/2$ apart, which results in $D_{\text{B}} = 9.45$ meters. Consequently, $d_{\text{Rayleigh}} \approx 596$ meters. Hence, we can not assume that all UEs and scatterers are located outside the Rayleigh distance of the BS array which renders the plane wave front assumption invalid in such systems. Careful studies are thus required to assess the applicability and validity of traditional channel models in systems with physical large antenna arrays.

Physical Models

In order to overcome the restrictions of analytic channel models, more advanced concepts have been developed to characterize practical propagation environments more accurately. To generate the channel coefficients of $\boldsymbol{H}$, physical modelling approaches make use of basic physical principles of electromagnetic wave propagation in real environments. Generally, physical models are distinguished into three categories, namely deterministic, geometry-based stochastic, and non-geometrical stochastic models [19]. Deterministic channel models are obtained from practical experiments in one particular environment. Despite being extremely accurate, such models are impractical due to the complicated procedure involved when obtaining the model parameters, the high computational complexity, and the validity for only one specific location [19]. In contrast to this, geometry-based stochastic models artificially generate a virtual propagation environment such that relevant properties of the generated channels match those of real propagation environ-

ments from a statistical perspective. More specifically, the simulation environment is filled with a number of scatterers, a BS and UEs at certain locations and the channels coefficients are then obtained by superposition of the contributions of all scatterers.

Physical channel models generally exhibit a more complex nature than analytical models and are usually not mathematically tractable [20]. However, owing to the more accurate description of actual propagation effects of electromagnetic waves, these models facilitate a more precise representation of practical propagation environments which is particularly helpful for the modelling of massive MIMO systems. Consequently, such models are widely used to evaluate the performance of a given system design under more practical conditions in order to obtain realistic performance estimates [20].

2.2 Channel Models for Massive MIMO

After our brief categorization of channel models available in literature, we now describe some selected representatives which are typical used for analysis and simulation of massive MIMO systems. We first present three analytic channel models widely applied in theoretical massive MIMO studies. Then, we introduce the COST 2100 model, a physical channel model considered as a suitable approach for practical massive MIMO channel modelling.

2.2.1 I.I.D. Rayleigh Model

The most simple analytical channel model often adapted in massive MIMO related literature (see e.g. [8–10, 22–24]) is the so-called *independent identical distributed (i.i.d.) Rayleigh fading model.* This model falls into the category of correlation-based analytic channel models [25]. The entries of $\boldsymbol{H}$ are generated by identical, independent Gaussian distributions, and each channel between a UE and the BS is multiplied by a scalar to model the large-scale fading. Mathematically, we express the i.i.d. Rayleigh channel as

$$\boldsymbol{H} = \boldsymbol{D}^{1/2}\boldsymbol{W}, \tag{2.6}$$

where $\boldsymbol{W} \in \mathbb{C}^{K \times M}$ reflects the small-scale fading with $\boldsymbol{W} \sim \mathcal{CN}(\boldsymbol{0}, \boldsymbol{I}_M)$ and $\boldsymbol{D} \in \mathbb{R}^{K \times K}$ is a diagonal matrix containing the large-scale fading coefficients.

The i.i.d. Rayleigh model does not introduce any coupling or correlation between the channel coefficients. Therefore, it provides the highest capacity from an information theoretic point of view. To illustrate this, we remark that the capacity defined in (2.2) depends on the channel covariance matrix $\boldsymbol{H}\boldsymbol{H}^H$. Using the tools from random matrix theory, one can show that for very large array sizes, i.e., when $M \to \infty$ and $M/K = $ const. with $M > K$, the channel covariance matrix approaches almost surely a diagonal matrix [8], that is,

$$\frac{1}{M}\boldsymbol{H}\boldsymbol{H}^H \stackrel{M \to \infty}{=} \boldsymbol{D}. \tag{2.7}$$

This effect is known as *favourable propagation conditions*, since all K channels are orthogonal [8, 9, 20]. In this case, $\boldsymbol{H}$ can be considered as a system providing K parallel channels, each channel supporting its own individual data stream. Therefore, the i.i.d. Rayleigh channel provides ideal propagation conditions and constitutes an upper bound for the capacity of a MIMO system [8].

The i.i.d. Rayleigh model is very suitable for mathematical system analysis due to its simple analytic closed-form expression and the well explored properties of i.i.d. Gaussian random variables.

However, physical properties of electromagnetic wave propagation are not accurately covered by this model. Moreover, the model often overestimates the capacity of realistic transmission channels, especially in massive MIMO systems [11–13, 21, 26]. We will consider this phenomenon in more depth later in Chapter 2.3.

In our thesis, we will not take large-scale fading into account, i.e., we set $D = I_K$. This decision is based on the practice of the measurement campaigns which we will consult for performance comparisons of simulated and real-world massive MIMO systems later in our work. From a physical point of view, large-scale fading models the power imbalances between the channels of different UEs, i.e., to which extent the signals are attenuated on the way between transmitter and receiver. Mathematically, large-scale fading can be considered as an individual scalar for each user scaling the length of the corresponding channel vector. Thus, the direction of the vectors and consequently the degree of orthogonality of the channels, a key property of massive MIMO systems, is not directly affected by large-scale fading effects. This fact and the initial nature of our studies justify this fundamental decision.

Kronecker Model

As a second representative of correlation-based analytic channel models, we introduce the correlated Rayleigh model, also known as *Kronecker model*. In contrast to the i.i.d. Rayleigh model, the Kronecker model introduces spatial correlation between the entries of H. Mathematically, the Kronecker channel is defined as [15]

$$H = R_{\text{UE}}^{1/2} W R_{\text{B}}^{1/2},\tag{2.8}$$

where $R_{\text{B}} \in \mathbb{C}^{M \times M}$ and $R_{\text{UE}} \in \mathbb{C}^{K \times K}$ is the spatial correlation matrix at the BS antennas and the UEs, respectively.[2] Moreover, W has i.i.d. entries distributed according to $\mathcal{CN}(0, I_M)$.

It is easy to see from Eq. (2.8) that the correlation coefficients at the BS and at the UEs are assumed to be uncoupled in this model. This assumption is justified when the UEs are located far away from the BS antenna array and a sufficient amount of random scattering takes place between both locations [15]. We note that the Kronecker model has been criticized owing to its inability to generate a realistic transmission channel [27] and the model tends to underestimate the performance of real propagation channels. However, as our studies presented later in Chapter 2.3.4 will show, the Kronecker model is indeed capable of modelling realistic massive MIMO channels from a system-level point of view.

We remark, that the i.i.d Rayleigh model is a special case of the Kronecker model obtained by setting $R_{\text{B}} = I_M, R_{\text{UE}} = I_K$ in (2.8).

2.2.2 Clarke's Model

Originally introduced in [28], we briefly present Clarke's channel model as a typical example for propagation-based analytical models. The fundamental idea of this model is that the received signal is always a combination of multiple independent plane waves with random angles of arrival and phase shifts as a result of scattering effects in the propagation environment. For the sake of model tractability, the author in [28] fixed the number of scatterers and assumed that each scatterer

---

[2]As already mentioned, we assume that all large-scale coefficients are equal to one and we thus drop the large-scale fading matrix completely.

contributes one plane wave to the received signal. Then, the channel between a UE and the BS can be described as

$$\boldsymbol{h}_k = \frac{1}{\sqrt{N_s}} \sum_{s=1}^{N_s} \boldsymbol{a}(\alpha_{ks}) \exp(\jmath(2\pi f_d \cos \alpha_{ks} + \phi_{ks})), \tag{2.9}$$

where N_S is the number of scatterers, $\jmath$ is the imaginary unit, f_d is the maximum Doppler shift, and α_{ks} and ϕ_{ks} are the angles of arrival and initial phases, respectively, of the wave from the s-th scatterer which are independent of the UE and scatter indices. Both α_{ks} and ϕ_{ks} are i.i.d. random variables uniformly distributed in the interval $[-\pi, \pi)$ and $f_d = v/cf_c$, where v is the speed of the UE, c is the speed of light and f_c is the carrier frequency [29]. Moreover, $\boldsymbol{a}(\alpha_{ks}) \in \mathbb{C}^{M \times 1}$ denotes the steering vector of the antenna array at the BS. For a linear array with $\lambda/2$ antenna spacing, the steering vector is given as [30]

$$\boldsymbol{a}(\alpha_{ks}) = \begin{pmatrix} 1 \\ \exp(-\jmath\pi \cos(\alpha_{ks})) \\ \vdots \\ \exp(-\jmath\pi(M-1)\cos(\alpha_{ks})) \end{pmatrix}. \tag{2.10}$$

It is worth noting that Clarke's channel model is identical to the i.i.d. Rayleigh model when N_S grows large as result of the central limit theorem [31].

2.2.3 COST 2100 Channel Model

Much effort has been made to develop sophisticated geometry-based stochastic channel models in order to overcome the limitations of analytic modelling approaches. In contemporary fourth generation (4G) wireless systems, WINNER II [32] and COST 273 [33] are often used for practical system evaluation. Currently, researches work on extensions of these concepts to model and incorporate new technologies and features of future wireless communication systems [11, 34]. In our thesis, we consider the COST 2100 model as one representative of geometry-based stochastic channel models since it has been identified as a potential candidate accurately modelling practical massive MIMO systems [11, 13, 35].

In COST 2100, each wave is assumed to travel via a multitude of scatterers from transmitter to receiver [36]. As an effect of reflection, diffraction and refraction, each scatterer will attenuate or amplify the signal amplitude, and impacts propagation direction and phase offset of the impinging wave. The received signal is then obtained by superposition of all waves originating from all scatterers. COST 2100 is a scatter-level modelling approach [36], since the entries of $\boldsymbol{H}$ are determined by the properties of the scatterers. To generate the entries of $\boldsymbol{H}$, an artificial propagation environment with randomly located scatterers is created and the channel coefficients are computed depending on the location of BS and UE. The basic steps of the COST 2100 modelling procedure are outlined next.

1. Definition of simulation scenario:

   - specify propagation scenario, e.g., indoor, urban or rural outdoor environment, Line-of-Sight (LOS) or Non-Line-of-Sight (NLOS) conditions
   - define fundamental system parameters, e.g. center frequency, number of cells

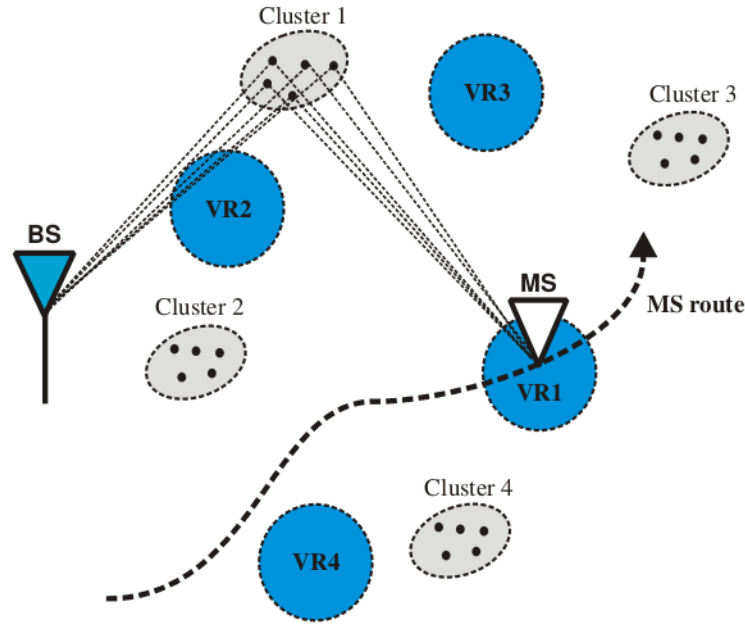2. Generation of simulation environment

Figure 2.2: Four clusters with their respective visibility regions (denoted as VR). Only cluster one is active in this scenario. Figure adopted from [19].

- determine number and location of scatterers and their properties such as signal attenuation, phase shift, visibility regions
- locate BS and UEs and assign velocity and moving direction to UEs

3. Compute channel coefficients between each UE and the antennas at the BS array as a superposition of the contributions of all scatterers visible at the UE's location

The key idea of COST 2100 is that each scatterer is assigned a number of so-called visibility regions [36]. A scatterer only contributes to the propagation of a UE (i.e. the channel coefficients of the UE's channel) if the UE is located within the visibility region of the respective scatterer (as illustrated in Fig. 2.2). This approach inherently enables the simulation of practical multi-user systems since co-located UEs will see the same scatterers and consequently have similar channels. In contrast to this, in the WINNER II model, the channel coefficients are generated for each UE individually, which might lead to inconsistent modelling of closely located UEs [34]. The spatial consistency renders COST 2100 particularly suitable for massive MIMO, since the high spatial model resolution enables a more thorough evaluation of the enhanced beamforming capabilities of large antenna arrays.

In the following, we elaborate the fundamental idea behind the scatterers in more detail. The concept originates from observations made in practical measurement campaigns which showed that MPCs usually arrive in packets. More specifically, multiple signals with very similar angles of arrival and path delays were usually detected at the receiver as a result of the interaction of the propagating signal with the surface of typical scatterers [36]. As an example of a typical scatterer, let us consider a building which causes multiple reflections due to different surface materials (e.g. glass and stone) and shapes of the facade (e.g. balconies and windows). Here the individual angles of arrival of the MPCs might fluctuate. However, they will be strongly related to the angle between the antenna array at the BS and the building (i.e. the scatterer) where the MPCs originate from [36]. Thus, COST 2100 models the contributions of one scatterer as a packet of MPCs, where the MPCs' characteristics are described statistically. The concept facilitates an accurate represen-

tation of realistic environments due to its close relation to physical properties of electromagnetic wave propagation. Moreover, the approach helps to decrease the model complexity in terms of required model parameters. This is because it is sufficient to characterize a scatterer by an average number of emitted MPCs, and the mean values and variances of attenuation and angular properties of the MPCs. This renders the individual parameterization of each MPC unnecessary. COST 2100 distinguishes two types of scatterers, namely local and far scatterers. Each UE is surrounded by its own local scatterers and these scatterers always contribute to the signal propagation of the UE, regardless of its location. In contrast to this, far scatterers are specific to the simulation environment and they are randomly located at a fixed position. Each far scatterer is assigned a number of visibility regions, which describe circular areas in the azimuth plane of the environment. The MPC components of a far scatterer only contribute to a UE's channel if the UE is located within the visibility region of that scatterer (cf. Fig. 2.2).

As already mentioned, the channel coefficients between a UE and the BS antennas are eventually obtained by the superposition of all contributions of the scatterers visible at the UE's location. Mathematically, the channel between a single-antenna UE and the BS drawn from the COST 2100 is obtained as [36]

$$\boldsymbol{h}_k = \rho_k \sum_{s \in \mathcal{S}_k} \varrho_s \sum_{n=1}^{N_s} w_{sn} \boldsymbol{a}(\alpha_{sn}, \theta_{sn}), \tag{2.11}$$

where ρ_k is the overall path-loss between the UE and the BS and $\mathcal{S}_k$ denotes the set of scatterers visible at the location of UE k. Furthermore, ϱ_s denotes the scatterer specific attenuation and w_{sn} describes the complex Gaussian fading of the n-th MPC of the s-th scatterer (where scatterer s has N_s MPCs). To obtain the contributions of each MPC to the M element channel vector, w_{sn} is multiplied by the steering vector of the antenna array, denoted as $\boldsymbol{a}(\alpha_{sn}, \theta_{sn})$, where α_{sn} and θ_{sn} is the azimuth and elevation angle-of-arrival, respectively, of the plain wave originating from the n-th MPC of the s-th scatterer.

The COST 2100 model facilitates an accurate characterization of a wireless propagation environment in space, time and frequency [13]. This, however, comes along with considerable computational model complexity and the loss of analytic tractability. We therefore investigate methods to approximate the outcomes of COST 2100 by means of a simple analytic channel model. We note that [11] suggest extension to the original COST 2100 model in order to further increase the modelling accuracy for massive MIMO systems. However, at the time of writing, the modified COST 2100 model had not been published yet which is why we adopt the original COST 2100 model in our studies.

2.3 Evaluation of Models in Massive MIMO Systems

In the remainder of this chapter, we compare the previously presented channel models from a system-level point of view by evaluating the properties of the channel coefficients in terms of separability and capacity. First, we introduce the metrics used for our model comparisons. Subsequently, we compare the channels generated by the presented models with data obtained from real-world massive MIMO measurement campaigns. Based on these comparisons, we determine the suitability of the models to simulate the performance of massive MIMO systems in realistic environments.

2.3.1 Metrics for Model Evaluation

With our studies presented in the following, we aim to investigate how "favourable" the channels drawn from the models presented above are compared to real-world massive MIMO channels. In alignment with the measurement campaign [37], we focus on the orthogonality of the channels of different UEs. Thus, we eliminate power imbalances between the UEs by normalizing the power of each individual channel to one. More specifically, we normalize each channel vector (i.e. each column of $\boldsymbol{H}$) as

$$\boldsymbol{h}_{k,\text{norm}} = \frac{\boldsymbol{h}_k}{\|\boldsymbol{h}_k\|}. \tag{2.12}$$

The normalized channel matrix is then obtained as $\boldsymbol{H}_{\text{norm}} = [\boldsymbol{h}_{1,\text{norm}}, \ldots, \boldsymbol{h}_{K,\text{norm}}]$. For the ease of notation, we will drop the "norm" subscript in all equations for the rest of this chapter.

Channel Correlation

As a first comparison metric, we introduce the *average normalized spatial correlation* defined as [12]

$$\xi = \frac{2}{K^2 - K} \sum_{k=1}^{K} \sum_{j>k}^{K} \frac{\left|\boldsymbol{h}_k^H \boldsymbol{h}_j\right|}{\|\boldsymbol{h}_k\| \|\boldsymbol{h}_j\|}, \tag{2.13}$$

where $\boldsymbol{h}_k$ denotes the channel between UE k and the BS, i.e., the k-th row of the channel matrix $\boldsymbol{H}$. The measure $\xi \in [0, 1]$ provides insights into the (average) similarity of the channels of two UEs. If ξ is close to zero, the channels are pairwise uncorrelated on average, while values of ξ close to one imply that the channels are strongly correlated. In the ideal case, i.e., under favourable propagation conditions, all channels are mutually uncorrelated which means that $\xi = 0$. We remark, that for the i.i.d. Rayleigh model favourable propagation conditions hold almost surely if $M \to \infty$ [12].

Pairwise correlation reveals information about channel similarity, which is particularly helpful when studying the properties of closely spaced UEs and their channels. However, this metric does not provide sufficient information to draw conclusions about the channel capacity. Thus, we introduce a more sophisticated metric measuring joint spatial correlation in the following.

Singular Value Spread of Channel Matrix

Joint spatial correlation is related to the singular values of $\boldsymbol{H}$ and reveals information about the capacity of the simulated propagation channel. We measure *joint spatial correlation*, subsequently denoted by κ, by means of the Singular Value Spread (SVS) of the channel matrix $\boldsymbol{H}$. We recall, that as a result of the singular value decomposition described in Eq. (2.3), we obtain K singular values $\sigma_1, \geq \ldots, \sigma_K \geq 0$. The SVS of $\boldsymbol{H}$ is then defined as the ratio between the largest and smallest singular value, that is,

$$\kappa = \frac{\sigma_1}{\sigma_K}. \tag{2.14}$$

It is evident that $\kappa \in [1, \infty)$. Note that the SVS is sometimes referred to as *condition number* of the matrix $\boldsymbol{H}$ [11].

The SVS indicates how favourable the propagation conditions are for a given channel matrix $\boldsymbol{H}$. If $\kappa = 1$, the channels of the UEs (i.e. the columns in $\boldsymbol{H}$) are orthogonal, and simultaneously transmitted data streams are perfectly separable at the receiver. On the other hand, if κ is large, there exists a strong linear dependency between the channels of at least two UEs. Therefore, values of κ close to one are desirable since they imply that $\boldsymbol{H}$ provides favourable propagation conditions.

Sum Rate Performance

In general, the channel capacity as defined in Eq. (2.2) is obtained when non-linear precoding or detection techniques are employed. Unfortunately, such techniques are usually too complex to be applied in practical systems [8]. In order to shed light on the achievable performance in realistic massive MIMO systems, we therefore introduce the downlink capacity when a more practical precoding scheme is applied at the BS. For our comparisons, we assume that the BS performs Zero-Forcing Beamforming (ZFBF) to precode the signals of the K UEs in the downlink. The ZFBF precoding matrix is obtained as the Pseudo-inverse of the channel matrix, and consequently, the transmission model described in (2.1) can be rewritten as

$$\boldsymbol{y} = \boldsymbol{H}\boldsymbol{x} + \boldsymbol{n} = \gamma \boldsymbol{H}\boldsymbol{H}^H \left(\boldsymbol{H}\boldsymbol{H}^H\right)^{-1} \boldsymbol{s} + \boldsymbol{n} = \gamma \boldsymbol{s} + \boldsymbol{n}, \tag{2.15}$$

where $\boldsymbol{s} \in \mathbb{C}^{K \times 1}$ denotes the K data symbols transmitted to the UEs[3], $\gamma = \sqrt{P_{\mathrm{BS}} / \operatorname{tr}\left[\left(\boldsymbol{H}\boldsymbol{H}^H\right)^{-1}\right]}$ is a measure of the signal-to-noise ratio (SNR) and P_{BS} denotes the transmit power at the BS. By plugging (2.15) into (2.2), we determine the capacity of the ZFBF downlink channel as

$$C = K \log_2 \left(1 + \gamma^2\right). \tag{2.16}$$

We note from (2.16) that the gain provided by a large antenna array can be used in two different ways. On the one hand, one can increase the SNR by increasing M, while the transmit power at the BS remains fixed. On the other hand, we can keep the SNR constant and scale down the transmit power at the BS with increasing M. In our simulations, we keep the SNR constant and scale down the transmit power linearly with M due to the normalization performed in Eq. (2.12).

2.3.2 Characteristics of Practical Massive MIMO Channels

Before we investigate how well the presented models reflect the properties of real-world massive MIMO propagation channels, we characterize realistic propagation environments by means of our proposed evaluation criteria. Since practical experiments are out of the scope of this thesis, we make use of practical measurement results available in literature. A fair number of massive MIMO measurement campaigns with different focuses has been carried out lately. While the experiments presented in [35, 38] study physical aspects such as power variations and angular distributions of the received signals over the antenna array, the vast majority of measurement campaigns tackles practical investigations from a system-level point of view by studying metrics like capacity and SVS of the measured channels, see e.g. [11–13, 15, 21, 37, 39–42]. Furthermore, we note that a first attempt to standardize channel modelling for future communication systems based on real-world measurements was made in the realm of the METIS project (see [34] for more detail).

In our thesis, we will mainly refer to [12, 40] to study pairwise channel correlation in practical massive MIMO systems. Moreover, we consult the extensive measurement campaign [11, 37, 39] for the evaluation of joint channel correlation of real-world propagation channels in terms of SVS. We will compare the practical results with the characteristics of an i.i.d. Rayleigh channel to assess the validity of the favourable propagation assumption for real-world massive MIMO systems. Based on the practical observations, we will then derive a suitable parameterization of the Kronecker model as a first attempt to cover typical characteristics of practical massive MIMO channels with

---

[3]We assume data symbols with unit variance, i.e., $\mathbb{E}(\boldsymbol{s}^H \boldsymbol{s}) = \boldsymbol{I}_K$.
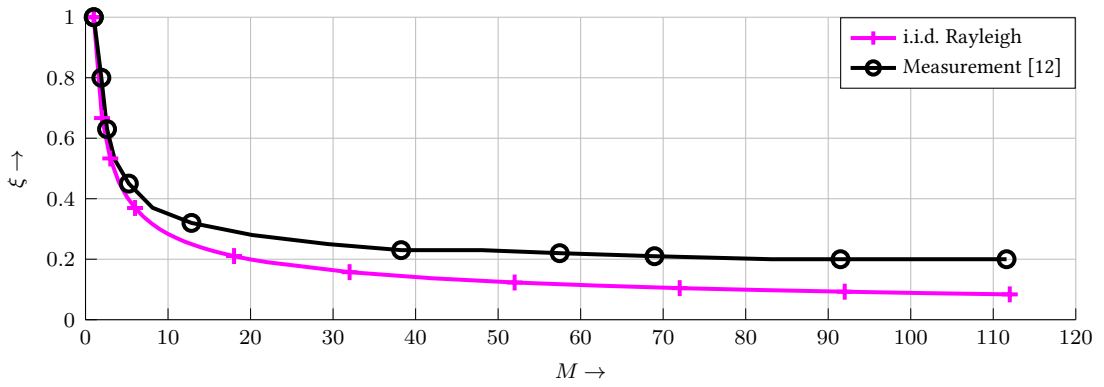
Figure 2.3: Average pairwise channel correlation for $K = 30$ well separated UEs (5 meters or more apart from each other).

a simple analytic model.

In general, physical propagation environments are distinguished into three different categories, namely indoor, outdoor and indoor-outdoor scenarios [34]. These categories can be further split into several sub scenarios based on user mobility, building and user density and many more. Despite the availability of indoor measurement results, see e.g. [11, 41, 42], we restrict ourselves to well-documented measurement campaigns conducted in semi-urban outdoor environments. We made this decision based on observations made in indoor and outdoor experiments documented in [11], which revealed that indoor scenarios provide more favourable propagation conditions in general. It is important to note that physical propagation environments are further distinguished in NLOS and LOS scenarios, respectively. It has been observed in practical experiments, that massive MIMO systems perform better under NLOS conditions as a result of increased propagation path diversity [37]. Under strong LOS conditions, however, spatial separation of UEs becomes particularly difficult due to the dominating contribution of the LOS component. This effect is even more pronounced when the UEs are closely located [37]. Consequently, co-located UEs under strong LOS conditions are very challenging scenarios for massive MIMO systems. Therefore, in our thesis we will focus on scenarios with LOS and mixed LOS/ NLOS conditions to evaluate the performance of massive MIMO systems in particularly difficult but realistic propagation environments.

Properties of Practical Channels of Well Separated UEs

In theoretical works, it is often assumed that the channels of sufficiently spaced UEs are uncorrelated when M grows large, see e.g. [9, 43–45]. This assumption is based on the properties of the i.i.d. Rayleigh model in which the channels are indeed rendered uncorrelated with growing M. In the following, we will investigate whether this assumption is satisfied in practical environments.

We first present real-world data measuring pairwise channel correlation of spatially separated UEs. Practical measurements with UEs located several meters apart from each other were presented in [12, 40]. While [40] considered only medium-sized arrays with up to 32 antennas and two active UEs, [12] presented the results of experiments with up to 112 antennas and 30 users. A similar behaviour of the pairwise channel correlation was observed in both experiments, therefore, we only present the results for ξ from [12] in Fig. 2.3. In addition, we also plot the trajectory of ξ versus M for channels generated by the i.i.d. Rayleigh model for comparison purposes. It is easy to see that an increasing number of BS antennas indeed helps to decrease the correlation between the channels in practical scenarios. However, the trajectories in Fig. 2.3 clearly demonstrate that
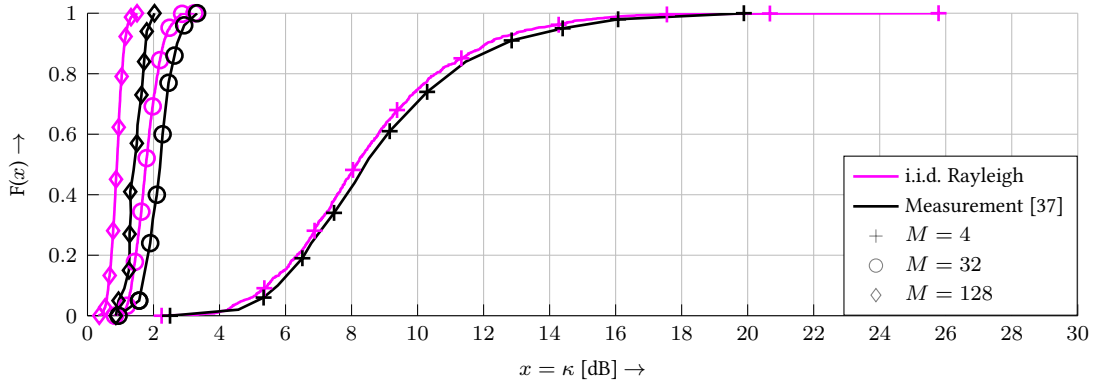
Figure 2.4: SVS for $K = 4$ well separated UEs.

the i.i.d. Rayleigh model does not accurately model the decorrelation effect observed in practical scenarios for $M > 10$, which can be explained as follows. Even though the UEs are separated by several meters, their signals might propagate via the same scatterers in the environment, which in turn can lead to similar channel coefficients [40]. While increasing M from one to ten facilitates the resolution of more scatterers and thus greatly helps to decorrelated the channels, the beneficial effects of further increasing M vanish due to the limited number of scatterers existent in the propagation environment [40].

To further investigate the assumption of uncorrelated channels and its validity in practical systems, we now evaluate joint correlation by means of SVS. The measurement campaigns [21, 37] provide results for the SVS of realistic massive MIMO channels for up to 128 antennas at the BS. We show the SVS for several antenna settings and $K = 4$ spatially separated UEs extracted from the measurement campaign [37] in Fig. 2.4. First, we observe that the *channel hardening effect* observed in i.i.d. Rayleigh channels is also a characteristic of realistic channels which means that the channel statistics become stable over different channel realizations due to the increased number of BS antennas. For $M = 4$, i.e., in a conventional MIMO setup, the slope of the Cumulative Distribution Function (CDF) of κ is quite flat, that is, the SVS fluctuates considerably over different channel realizations. In contrast to this, for $M = 32, 128$, i.e., in a massive MIMO setup, the slope is very steep which means that the SVS barley fluctuates over the channel realizations. This indicates that the performance of a massive MIMO system becomes insensitive to the instantaneous small-scale channel coefficients and thus more predictable. Second, we observe that the SVS of the measured channels is close to that of i.i.d. Rayleigh channels. However, the figure indicates that the mean values of κ deviate in measured and i.i.d. Rayleigh channels when M is large, which is again a result of the limited number of scatterers (and consequently propagation paths) provided by the propagation environment. This aligns with the saturation effect for large M observed in Fig. 2.3.

We conclude that practical massive MIMO channels with UEs located far apart exhibit similar properties as those of i.i.d. Rayleigh channels. A large antenna array indeed helps decorrelate the channels of the UEs as the i.i.d. Rayleigh model suggests. However, a saturation effect can be observed in practical systems for large M, which is not accurately covered by the analytical model. Thus, an arbitrary increase of M is not expected to render the channels of spatially separated UEs completely uncorrelated in practical systems.
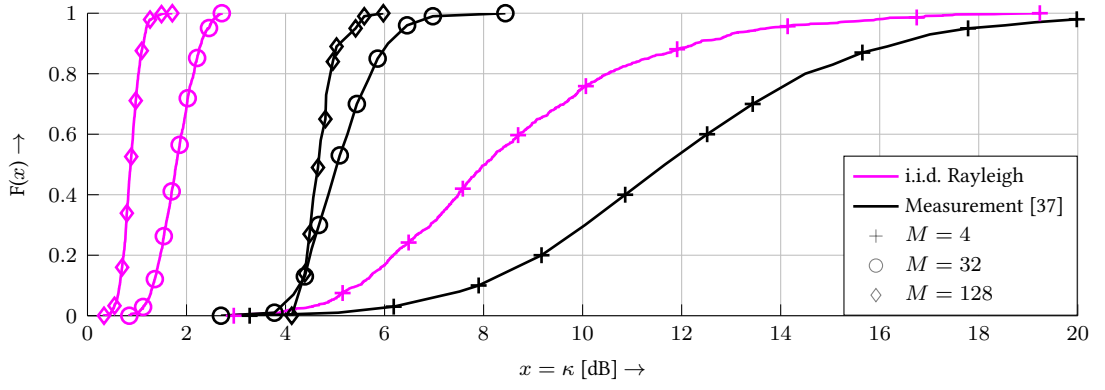
Figure 2.5: SVS for $K = 4$ closely spaced UEs (1.5 to 2 meters apart from each other).
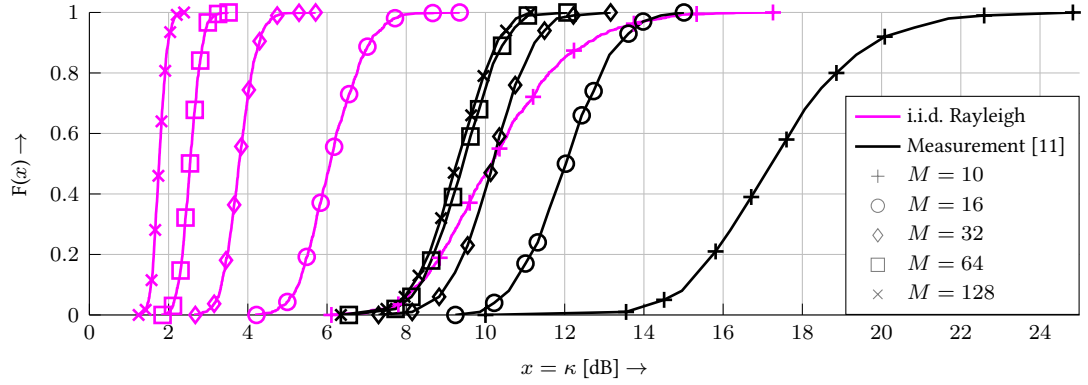

Figure 2.6: SVS for $K = 9$ closely spaced UEs (all UEs within a 5 meter-diameter circle).

Properties of Practical Channels of Closely Located UEs

After considering a desirable scenario in which the UEs are spatially separated, we now investigate a more difficult situation where the UEs are closely located. The joint correlation[4] observed in a practical LOS scenario with four UEs spaced 1.5 to 2 meters apart from each other and up to 128 BS antennas is presented in [37]. Moreover, a mixed LOS/ NLOS scenario with 9 users located within a five-meter diameter circle and 128 BS antennas is studied in [11]. The results of the experiments documented in [11] and [37] are depicted in Fig. 2.5 and Fig. 2.6, respectively.

We observe from the figures that the channel hardening effect can also be observed in practical scenarios with closely located UEs and the slopes of the CDFs of κ observed in measured channels are similar to those of the equivalent i.i.d. Rayleigh model. Furthermore, the CDFs move to the left when increasing M which indicates that large antenna arrays help to decorrelate the channels even in difficult scenarios considered here. However, there is a significant deviation of the mean values of κ for the measured and the i.i.d. Rayleigh channels, and the analytical model considerably overestimates the ability of a large antenna array to separate co-located UEs. Moreover, by comparing Fig. 2.4 and Fig. 2.5 we conclude that the joint channel correlation (i.e. the mean value of κ) is significantly increased when the UEs are located close to each other. While the signals of well separated UEs propagate via different sets of scatterers, closely spaced UEs usually see the same scatterers. As already mentioned, the MPCs of one scatterer have similar properties, which leads to the increased channel correlation [11]. Nevertheless, we conclude from Fig. 2.5 and Fig. 2.6 that even closely spaced UEs can be separated at the BS. This is because even though the UEs see

---

[4]We consider only joint correlation in such scenarios since no practical measurements studying pairwise correlation of closely spaced UEs were available at the time of writing.

the same scatterers, the set of MPCs contributing to the signal propagation is different from UE to UE [13].

In conclusion, we state that increasing M is also beneficial in case of closely located UEs and helps decorrelate the channels. However, measurements indicate that non-negligible UE correlation exists among co-located UEs which renders the i.i.d. Rayleigh model inappropriate for such scenarios. To avoid an overestimation of the performance of massive MIMO systems, user correlation should thus be taken into account when modelling co-located users.

2.3.3 Parameterization of Kronecker Model Based on Measurement Data

Based on the results of the experimental massive MIMO studies described above, we now suggest a simple analytical model which covers typical characteristics of real-world propagation environments from a system-level point of view. In our work, we adopt the Kronecker model to generate the artificial massive MIMO channels. It is not our goal to model physical properties of realistic channels, but we only focus on the modelling of stochastic parameters of the channel coefficients, such as channel correlation and eigenvalues, since these measures directly determine the channel capacity in Eq. (2.4). We adopt the Kronecker model since it allows us to express correlation at the BS and the UE side independent of each other. We will parameterize the Kronecker model such that pairwise channel correlation and joint spatial correlation of the resulting channels approximate that of the measured channels well. As a basic goal, we aim to provide an easy closed-form expression for the correlation matrices in (2.8), independent of physical parameters such as distances between the UEs. Such an approach reduces the required model parameters to an absolute minimum and renders the generation of an artificial simulation environment unnecessary. Thus the model is particularly suitable for theoretical analysis of realistic massive MIMO systems due to the resulting low computational complexity and the small number of parameters.

In the following, we present the expressions for the correlation matrices $\boldsymbol{R}_\mathrm{B}$ and $\boldsymbol{R}_\mathrm{UE}$. We follow the basic approaches used in [46–48] and model the correlation matrices by means of a simple exponential model. Although the entries of $\boldsymbol{R}_\mathrm{B}$ and $\boldsymbol{R}_\mathrm{UE}$ can be complex in general, we restrict ourselves to real entries only. This restriction is justified by the observations made in [46] which show that real exponential correlation matrices can indeed model realistic channels well in terms of the resulting channel capacity. Mathematically, the entry in row i and column j of the correlation matrices suggested in [46] is given by $R[i, j] = a^{|i-j|^2}$ with $a \in [0, 1]$. Consequently, the structure of the corresponding N by N matrix is given as

$$\boldsymbol{R} = \begin{pmatrix} 1 & a^{1^2} & a^{2^2} & \dots & a^{(N-1)^2} \\ a^{1^2} & 1 & a^{1^2} & \ddots & \vdots \\ a^{2^2} & a^{1^2} & 1 & \ddots & a^{2^2} \\ \vdots & \ddots & \ddots & \ddots & a^{1^2} \\ a^{(N-1)^2} & \dots & a^{2^2} & a^{1^2} & 1 \end{pmatrix}. \tag{2.17}$$

We remark that $\boldsymbol{R}$ has a Toeplitz structure, when the exponential correlation model is adopted.

Let us first focus on the case where the UEs are located far apart from each other. Following the observations described in Chapter 2.3.2, we assume the UEs to be uncorrelated in this case, i.e., we set $\boldsymbol{R}_\mathrm{UE} = \boldsymbol{I}_K$ in Eq. (2.8). We recall that the channels of well separated UEs can not be decorrelated completely by increasing M at the BS (cf. Chapter 2.3.2). In fact, a saturation
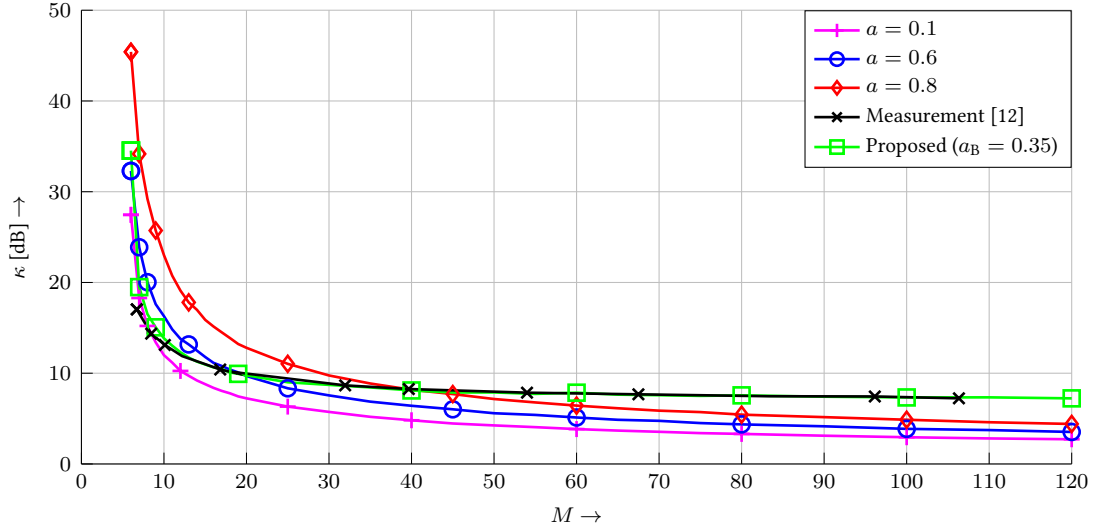
Figure 2.7: Average SVS (in dB) versus M for $K = 6$ UEs spaced far apart from each other (5 meters of more).

effect was observed in practical systems occurring for moderate and large M, which manifests in an unchanged value of average pairwise and joint channel correlation when M is increased. This phenomenon has to be taken into account when modelling the correlation at the BS in a massive MIMO systems. Unfortunately, this saturation effect can not be accurately covered by the exponential structure described in (2.17). To demonstrate this, we plot the average SVS resulting from the Kronecker model with $\boldsymbol{R}_{\mathrm{UE}} = \boldsymbol{I}_K$ and $\boldsymbol{R}_{\mathrm{B}} = \boldsymbol{R}$ (with different values for a) versus M for $K = 6$ well separated UEs in Fig. 2.7. For comparison purposes, we also plot the average SVS extracted from the measurement campaign [12] for $K = 6$ well separated UEs. It is easy to see from the figure, that the saturating decorrelation effect observed in practical systems is not covered well by the structure shown in (2.17). Thus, we propose the introduction of a penalty on the correlation coefficients which grows with M. More specifically, we suggest to generate the entries of $\boldsymbol{R}$ according to $R[i, j] = a^{|i-j|^{2/M}}$. Then, the correlation matrix at the massive MIMO BS has the following structure:

$$\boldsymbol{R}_{\mathrm{B}} = \begin{pmatrix} 1 & a_{\mathrm{B}}^{1^{2/M}} & a_{\mathrm{B}}^{2^{2/M}} & \ldots & a_{\mathrm{B}}^{(N-1)^{2/M}} \\ a_{\mathrm{B}}^{1^{2/M}} & 1 & a_{\mathrm{B}}^{1^{2/M}} & \ddots & \vdots \\ a_{\mathrm{B}}^{2^{2/M}} & a_{\mathrm{B}}^{1^{2/M}} & 1 & \ddots & a_{\mathrm{B}}^{2^{2/M}} \\ \vdots & \ddots & \ddots & \ddots & a_{\mathrm{B}}^{1^{2/M}} \\ a_{\mathrm{B}}^{(N-1)^{2/M}} & \ldots & a_{\mathrm{B}}^{2^{2/M}} & a_{\mathrm{B}}^{1^{2/M}} & 1 \end{pmatrix}, \tag{2.18}$$

where $a_{\mathrm{B}} \in [0, 1]$, and the value of a_{B} is chosen such that the SVS extracted from a given measurement campaign is approximated well. To illustrate the penalty effect introduced by the modified correlation matrix, we plot the average SVS resulting from the Kronecker model with $\boldsymbol{R}_{\mathrm{UE}} = \boldsymbol{I}_K$ and $\boldsymbol{R}_{\mathrm{B}}$ as in (2.18) with $a_{\mathrm{B}} = 0.35$ for $K = 6$ and varying M in Fig. 2.7. The plot demonstrates that the trajectory of the SVS versus M observed in a real-world massive MIMO system can be approximated well with the proposed correlation matrix and the saturation effect with increasing M is accurately covered. Although this approach models realistic channels consistently over a wide range of M from a system-level point of view, it is important to note that this model does not necessarily reflect the true correlation coefficients of real physical channels.

Let us now consider the scenario, when the K UEs are closely located. In this case, the saturation effect with increasing M is still existent. Additionally, a significant increase in joint spatial correlation was observed which indicates that co-located UEs have similar channels (cf. Chapter 2.3.2). Therefore, we propose the introduction of correlation between co-located UEs. Specifically, we model the correlation matrix as $\boldsymbol{R}_{\text{UE}} = \boldsymbol{R}$, where $\boldsymbol{R}$ is obtained from (2.17) with $N = K$ and $a = a_{\text{UE}}$. Here, the model parameter a_{UE} is chosen such that the SVS extracted from a given measurement campaign is approximated well.[5]

Due to the proposed construction of the correlation matrices, the channel model is completely characterized by only two real parameters. The specific values of the parameters a_{B} and a_{UE} can be found by comparing the average SVS resulting from the Kronecker model with that resulting from corresponding measured channels. In the following section, we will demonstrate the suitability of our proposed Kronecker model to simulate realistic massive MIMO channel from a system-level point of view.

2.3.4 Model Comparison

In the remainder of this chapter, we will compare the presented channel models under massive MIMO configurations. The properties of the generated channel coefficients are evaluated by means of pairwise and joint channel correlation as well as channel capacity. Additionally, we will show these measures for the corresponding real-world channels in order to see to which extent the properties of practical channels are reflected by the artificially generated channels. In our simulation setup, we consider a single-cell system with one massive MIMO BS and a variable number of antennas and UEs. We average the results over 1000 independent channel realizations for each model. Moreover, we compute the average downlink sum rate, by numerically simulating the ZFBF data transmission for each channel realization.

In our experiments, we configure the COST 2100 channel according to the parameterization given in [11, Table 7.1] which was mostly derived from massive MIMO measurements. Moreover, similar to the COST 2100 configuration, we set the number of scatterers to $N_S = 15$ in Clarke's model. For the Kronecker model, we choose the correlation matrices as described in Chapter 2.3.3, where the parameters a_{B} and a_{UE} are chosen individually for the different experimental setups.

2.3.5 Pair-Wise Channel Correlation

We first compare the pairwise spatial correlation between the channels of the UEs drawn from different channel models. For this experiment, we reconstruct the real-world scenario considered in [12] and assume $K = 30$ UEs which are spatially separated by five meters or more. In our proposed Kronecker model, we therefore set $a_{\text{UE}} = 0$ (i.e., the UEs are uncorrelated) and we choose $a_{\text{B}} = 0.3$ such that ξ observed from the Kronecker channels approximates that of the measured channels well. For the COST 2100 model, we set the parameters according to the LOS case in [11, Table 7.1] and we place the 30 UEs as in the original experimental setup, that is, the UEs are located on two lines, where the distance between the UEs on a line is 5 meters and the distance between the lines is 50 meters.

Fig. 2.8 illustrates the average value of ξ versus M for the different channel models. It is evident, that increasing the number of BS antennas helps decorrelate the channels under all the models. For $M = 1, \ldots, 10$ the beneficial effect of increasing M observed in realistic environments is

---

[5]Note that a_{UE} depends on the number of closely spaced UEs to be modelled.
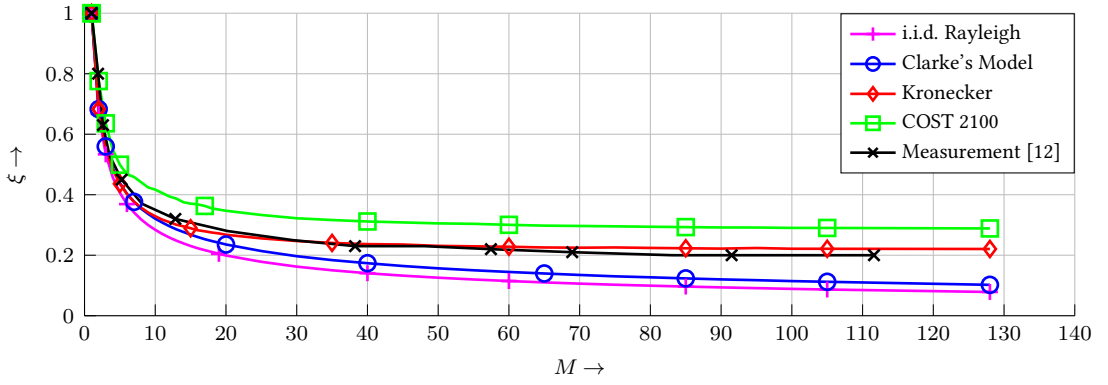
Figure 2.8: Average pairwise channel correlation for $K = 30$ well separated UEs.

approximated rather well by all the models. However, the channels drawn from the i.i.d. Rayleigh and Clarke's model provide a lower correlation than real-world channels when M grows large since both models assume completely uncorrelated fading over the antenna array. In contrast to this, we observe that the COST 2100 model and our proposed Kronecker model indeed exhibit a saturation effect with increasing M. It is worth noting that the Kronecker model approximates the realistic channels very well in terms of ξ over the whole range of M, however, the value of ξ obtained from COST 2100 saturates at a slightly higher level than observed in the measurements. These deviations are a result of the performed model parameterization procedure. While we tuned the parameter of the Kronecker model according to the measurement data, we adopted the parameter set given in [11] for COST 2100 since no parameterization of COST 2100 was provided in [12]. Although this comparison might thus appear somewhat unfair, we stress that the Kronecker model requires the tuning of a_B only, while an entire set of parameters needs to be identified for COST 2100, which, however, can hardly be inferred from the data provided in [12].

From the above observations, we conclude that COST 2100 and our proposed Kronecker model reflect the saturation effect in terms of ξ for growing M observed in realistic systems. This is in contrast to the i.i.d. Rayleigh model and Clarke's model which tend to overestimate the beneficial effects of an increasing number of BS antennas. In summary, the Kronecker model and COST 2100 are suitable to model realistic massive MIMO channels in terms of pairwise spatial correlation. Moreover, the Kronecker model is more easily matched to the real-world data than the COST 2100 model as a result of the considerable differences in terms of the number of required model parameters.

2.3.6 Singular Value Spread

Let us now investigate how well the presented channel models approximate real-world channels in terms of joint spatial correlation. To this end, we compare the CDFs of κ obtained from the channel models with those observed in the practical experiments [37] and [11]. For the Kronecker model, we set the correlation coefficient at the BS to $a_\mathrm{B} = 0.18$ and $a_\mathrm{B} = 0.3$ when reconstructing experiment [37] and [11], respectively. Moreover, we set the correlation at the UEs to $a_\mathrm{UE} = 0.5$ and $a_\mathrm{UE} = 0.6$ for [37] and [11], respectively. We chose the parameters of the Kronecker model, such that the CDFs of the SVS of the generated channels matches those measured in the references. To parameterize the COST 2100 channel model, we make use of the LOS configuration given in [11, Table 7.1] for both scenarios and we locate the UEs on a circle of five-meter diameter, where the distance between the BS and the centre of the circle is 50 meters. This approximates the physical

setup of the practical experiments.

Fig. 2.9a and Fig. 2.10 show the trajectories of the CFDs of κ for the two experimental setups. It is evident from the graphs that the slopes of the measured CFDs are well approximated by all the channel models. The increased steepness of the CDFs means that κ becomes more stable over different channel realizations when M grows. Thus, we conclude that the channel hardening effect observed in i.i.d. Rayleigh models is also a typical characteristic of realistic propagation environments.

After evaluating the slopes of the CDfs, we now focus on the relative locations of the CDFs. First, we compare the average values of κ of the channels drawn from the i.i.d. Rayleigh model and Clarke's model to that of the measured channels. Fig. 2.9a and Fig. 2.10 clearly show, that both models result in an average value for κ, which is significantly smaller than the values measured in the practical experiments for all antenna settings. We remark that the deviations become even more pronounced when M grows large and reach up to 7 dB. This observation aligns with the results presented in Fig. 2.8 which demonstrates that both models overestimate the beneficial effects of large M in a massive MIMO system. In contrast to this, the mean values of κ resulting from COST 2100 and the Kronecker model are much closer to the measured values and deviate by at most 4 dB. We also conclude from the figures that both models show the saturating behaviour of κ when M grows large. However, the COST 2100 model tends to underestimate the joint spatial correlation of real systems with closely located UEs when M is very large, while our proposed Kronecker model approximates the mean values of κ particularly well under massive MIMO settings. Thus, we conclude that the Kronecker model provides the best accuracy in terms of SVS when modelling massive MIMO systems with closely spaced UEs.

Another interesting question is how the channel models behave under different spatial user distributions and whether changes in terms of SVS observed in practical systems are covered by the models. Therefore, we compare the CDFs of κ when the BS serves four UEs which are either closely located or well separated in Fig. 2.9. As we demonstrated earlier in Chapter 2.3.2, increasing the spatial separation of the UEs helps to reduce joint spatial correlation in practical systems. This phenomenon, however, is not covered by the i.i.d. Rayleigh and Clarke's model since they do not support different spatial user distributions. On the contrary, the effects of increased user density are covered by the Kronecker model and COST 2100 as the plots in Fig. 2.9a and Fig. 2.9b reveal. We recall that the Kronecker model simulates co-located UEs by means of the correlation matrix $\boldsymbol{R}_{\mathrm{UE}}$ (2.8), whereas COST 2100 actually places the UEs in the simulation environment according to the experimental setup. Nevertheless, we observe a better match between κ obtained from simulations and the measurements when the Kronecker model is used. The mismatch of the COST 2100 model can be partly explained by the model parameterization used in our simulations. While we tuned the two parameters of the Kronecker model such that a good match between the CDFs of κ from simulations and measurements is achieved, such a tuning of COST 2100 is prohibitive owing to the large number of model parameters.

Before moving on to the comparison of the sum rates achievable under the different models, we evaluate the behaviour of the SVS versus M. To this end, we again consult the measurement campaign [12] and aim to reconstruct the experiment where the BS serves $K = 6$ UEs which are well separated by five meters. The trajectories of the SVSs for values of M varying between 6 and 120 is depicted in Fig. 2.11. The figure is another indicator that the i.i.d. Rayleigh and Clarke's model consistently underestimate the joint spatial correlation when M is large, even for well separated UEs. An interesting and somewhat surprising conclusion drawn from Fig. 2.11 is that COST 2100
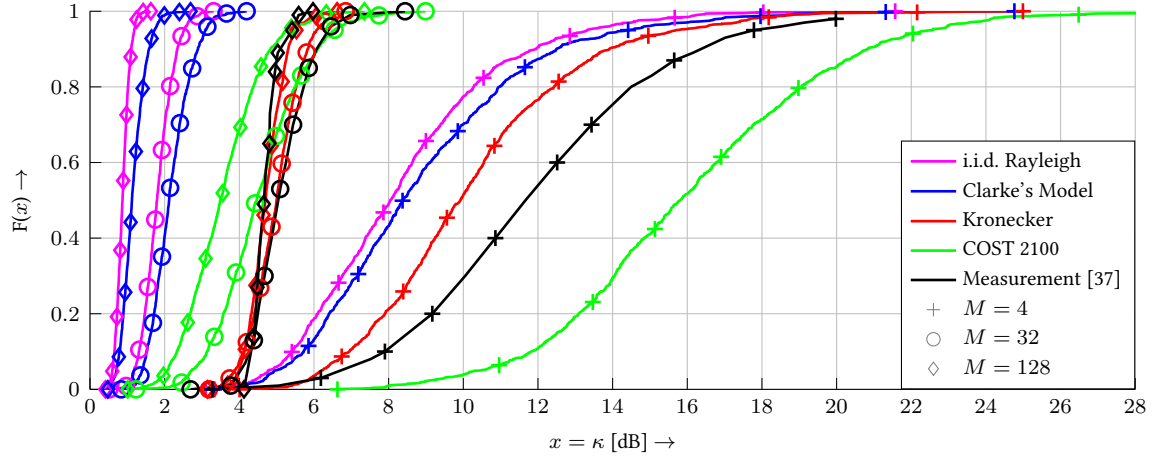
(a) UEs are closely located. For Kronecker model we used $a_{\mathrm{B}} = 0.18$, $a_{\mathrm{UE}} = 0.5$.
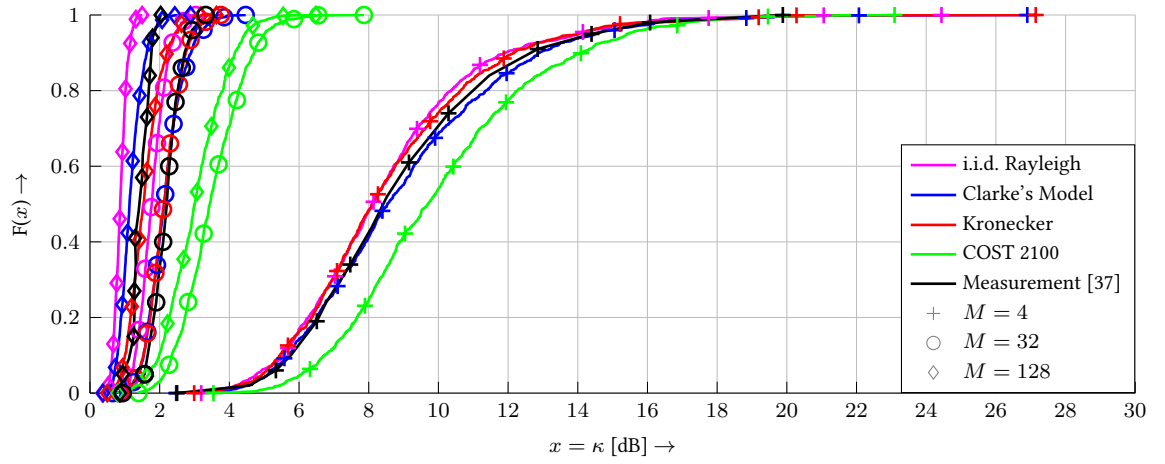
(b) UEs are separated. For the Kronecker model we used $a_{\mathrm{B}} = 0.18$, $a_{\mathrm{UE}} = 0$.
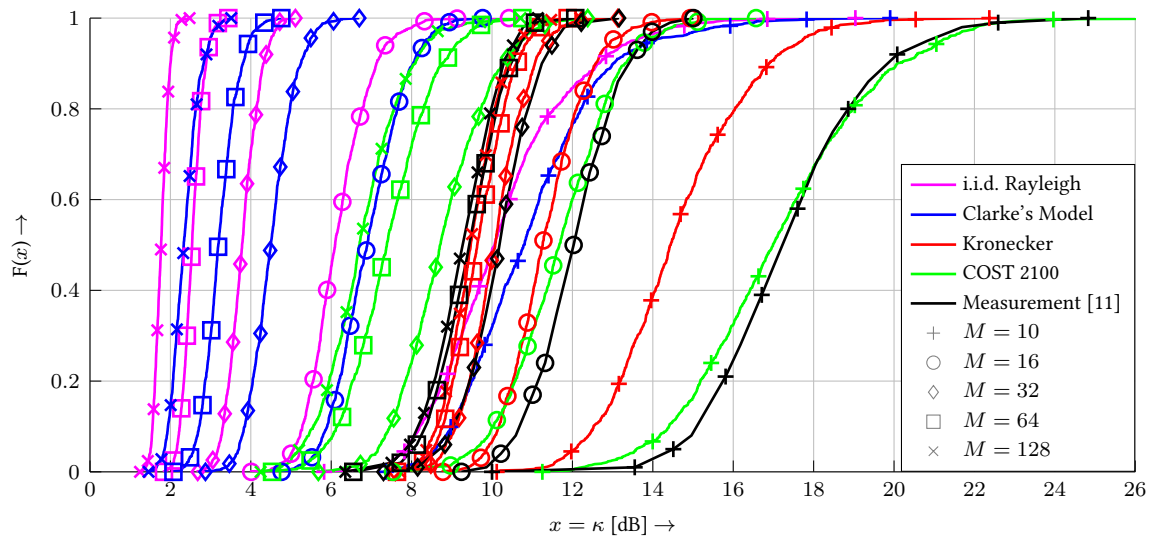
Figure 2.9: SVS for $K = 4$ UEs.

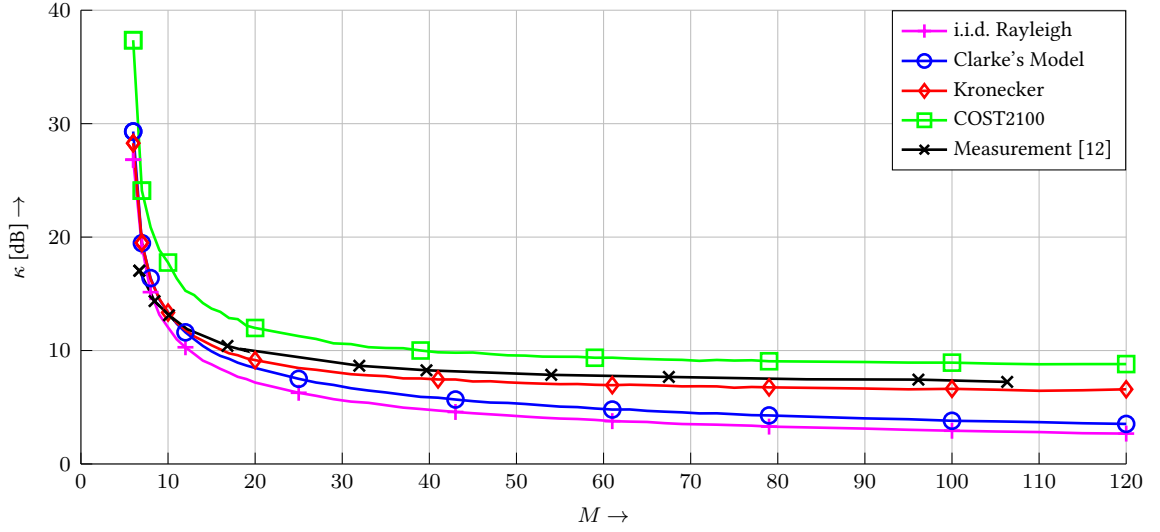Figure 2.10: SVS for $K = 9$ closely located UEs. For the Kronecker model we used $a_{\mathrm{B}} = 0.3$, $a_{\mathrm{UE}} = 0.6$.

Figure 2.11: SVS versus M for $K = 6$ well separated UEs. For the Kronecker model we used $a_{\mathrm{B}} = 0.3$, $a_{\mathrm{UE}} = 0$.

consistently overestimates κ in the given experiment. This observation demonstrates the modelling inconsistency of COST 2100, which was already discovered in the preceding experiments. Our proposed Kronecker model, however, approximates the measured channels very well in terms of the SVS over the entire range of M.

2.3.7 Sum Rate Performance

To complete our studies, we now focus on the sum rate performance of the ZFBF precoder under the different channel models. We first compare the performance of a massive MIMO system serving $K = 4$ UEs simultaneously in the downlink. We plot the downlink sum rate obtain according to Eq. (2.16) versus M for a fixed transmission power of $P_{\mathrm{BS}} = 10$ dB for the different channel models in Fig. 2.12 and compare it with the experimental results documented in [13]. It is evident that the i.i.d. Rayleigh model and Clarke's channel model consistently overestimate the performance of practical massive MIMO systems, which is in strong agreement with the conclusions drawn from the comparisons of joint orthogonality in the last section. Since both models significantly underestimate the channel correlation occurring in realistic systems with closely located UEs, they provide very optimistic predictions for the achievable capacity in massive MIMO systems which are unlikely to be met in realistic system setups. Fig. 2.12 further reveals an inconsistent modelling of the ZFBF performance by COST 2100. While for small M, the model tends to underestimate the achievable rates; it gives too optimistic values for large M. This behaviour goes hand in hand with the values of the SVS of the channels drawn from COST 2100, which were identified to be too large for small M and too small for large M earlier in Fig. 2.9a. In contrast to this, our proposed Kronecker model results in a very accurate modelling of the sum rate performance of practical systems over the entire range of M.

A similar conclusion can be drawn when studying the ZFBF performance versus Signal-to-Noise Ratio (SNR) for the different channel models. In Fig. 2.13 we depict the ZFBF downlink sum rate versus SNR for $M = 128$ antennas and $K = 9$ closely located UEs. First, we remark that for sufficiently large values of SNR, the sum rate scales linearly with increasing SNR in both the simulated and practical environments. However, the absolute value of the achievable sum rate obtained from
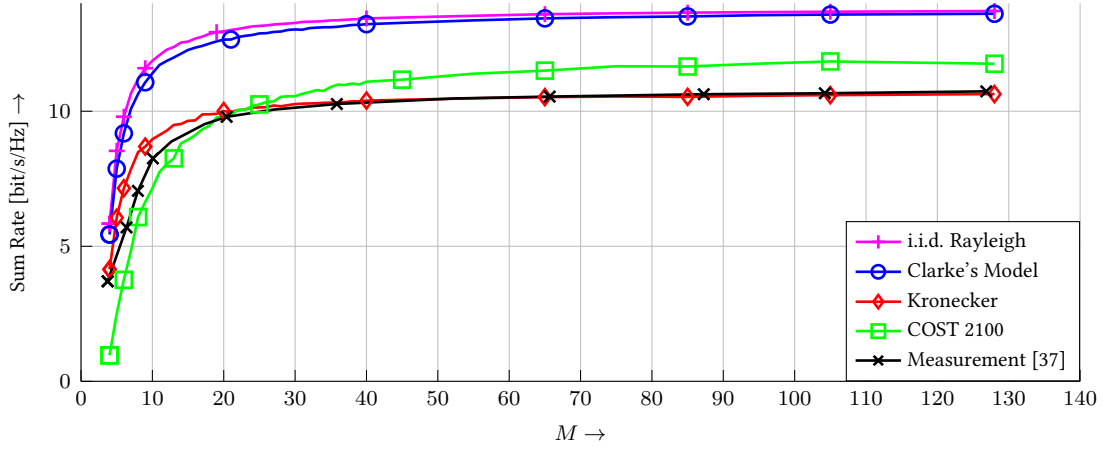
Figure 2.12: Sum Rate versus M for $K = 4$ closely located UEs. For the Kronecker model we used $a_{\mathrm{B}} = 0.18$, $a_{\mathrm{UE}} = 0.5$.
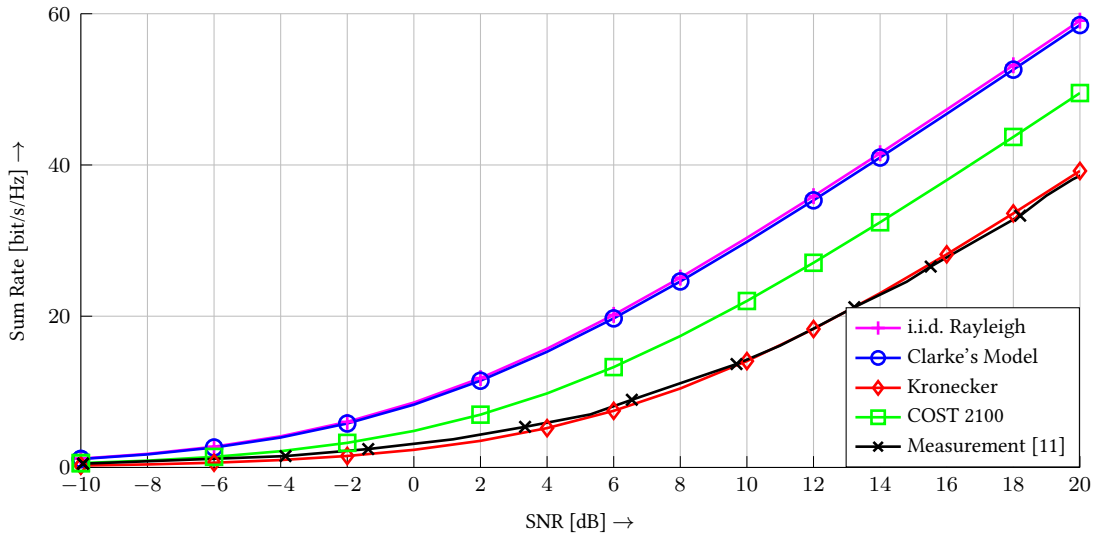
Figure 2.13: Sum Rate for $M = 128$ and $K = 9$ closely located UEs. For the Kronecker model we used $a_{\mathrm{B}} = 0.3$, $a_{\mathrm{UE}} = 0.6$.

the i.i.d. Rayleigh model and Clarke's model do not reflect the rates achievable in the real-world environment very well. This is again a result of the previously described underestimation of the channel correlation in i.i.d. Rayleigh and Clarke's model. Furthermore, we notice that the COST 2100 does also lead to an overestimation of the sum rate performance in the considered scenario. To understand this, we compare the SVS obtained from the COST 2100 model with that of the measured channels for $M = 128$ in Fig. 2.10. It is easy to see, that the SVS of the COST 2100 channels is significantly smaller than in the practical experiment which in turn explains the larger sum rate observed in Fig. 2.13. In contrast to this, it is evident from Fig. 2.13 that our proposed Kronecker model reflects realistic massive MIMO systems very well in terms of achievable sum rate over the entire SNR range considered here.

Overall, our simulations demonstrated that the i.i.d. Rayleigh model and Clarke's channel model consistently overestimate the performance of realistic massive MIMO systems since they do not take any correlation between the channel coefficients into account. In contrast to this, COST 2100 and our proposed Kronecker model provide more realistic estimates. While the Kronecker model is capable of modelling joint spatial correlation and sum rate performance of measured channels

very accurately, COST 2100 exhibits a modelling inconsistency which often leads to a mismatch between the simulated and measured channels. Thus, we conclude that the Kronecker model with the correlation matrices proposed in this thesis constitutes a very suitable approach to model practical massive MIMO systems from a system-level point of view.

2.4 Conclusions

Accurate channel models reflecting the properties of real-world propagation environments play a vital role when estimating the achievable performance of massive MIMO systems. In this chapter, four different models commonly used in the massive MIMO literature were examined in terms of their ability to reflect typical characteristics of practical channels.

The widely used i.i.d. Rayleigh channel model and the closely related Clarke model were shown to consistently overestimate the achievable performance of realistic systems due to absence of correlation between the channel coefficients in these models. As a result, both models provide very optimistic predictions for pairwise and joint spatial correlation as well as achievable sum rates in such systems. In particular, the gap between the predictions provided by both models and the measured results increases when the number of BS antennas grows very large, that is, the beneficial effects when switching from conventional MIMO systems to massive MIMO systems seen under the i.i.d. Rayleigh and Clarke's model can not be observed in practical systems.

In contrast to this, it was observed that the COST 2100 and the correlated Rayleigh models, incorporating spatial correlation parameters serve as a better approximation for massive MIMO channels. However, the COST 2100 model leads to somewhat inconsistent modelling results for varying M. Moreover, it has been identified to be inconvenient for theoretical system analysis owing to its high model complexity and the large number of parameters whose values are difficult to obtain from practical measurement data.

To overcome the inconsistencies of the existing models, a novel strategy to model massive MIMO channels was proposed. The suggested approach is based on the well-known Kronecker model, and a characterization of the correlation matrices by only two real parameters was derived. It was demonstrated that the Kronecker model with the proposed modified exponential correlation matrices is able to accurately predict pairwise and joint spatial correlation as well as achievable sum rates observed in real-world channels. Thus, the model presented in this thesis constitutes an approach to the channel modelling problem for massive MIMO systems, which provides more accurate and consistent predictions than existing models while being very easy to parameterize based on practical channel measurements.

3 Channel Estimation

Large antenna arrays at the BS of a wireless communication system offer many advantages such as improved signal detection in the uplink and very precise beamforming in the downlink. To leverage from the benefits offered by such massive antenna arrays, the BS needs access to the instantaneous channel coefficients, which in turn requires effective channel estimation techniques. Though various such channel estimation algorithms have been proposed in the massive MIMO literature, their performance evaluation has been limited to the case of standard channel models and determining their suitability for practical scenarios remains an important problem to be addressed. In this chapter, the evaluation of available estimation techniques is approached from a new perspective aiming to identify impacts of the underlying channel model on different estimators.

Similar to the preceding chapter, the work presented in the following was partly published in [14] in the framework of the 24th European Signal Processing Conference 2016 in Budapest, Hungary.

3.1 Preliminaries

In contrast to the last chapter, we now concentrate on the uplink of a massive MIMO system in a multi-cell setup. First, we introduce the system and transmission model assumed in this Chapter. Subsequently, we will explain the pilot contamination problem occurring in such multi-cell networks.

3.1.1 Multi-Cell Network Model

In this chapter, we consider the uplink of a fully synchronized multi-cell wireless communication system with B cells. In each cell, there is one massive MIMO BS equipped with M antennas serving K single-antenna UEs.[1] We define the uplink channel between UE k in cell j and the M antennas at the BS in cell b as $\boldsymbol{h}_{bj_k} \in \mathbb{C}^{M \times 1}$. Moreover, we collect all channels between the UEs in cell j and the BS located in cell b in the matrix $\boldsymbol{H}_{bj} = [\boldsymbol{h}_{bj_1}, \boldsymbol{h}_{bj_2}, \ldots, \boldsymbol{h}_{bj_K}] \in \mathbb{C}^{M \times K}$.[2] This multi-cell setup is illustrated in Fig. 3.1.

We learned from the last chapter, that the channel coefficients, i.e., the entries in $\boldsymbol{H}_{bj}$, are determined by the underlying propagation environment and the location of the UEs. Consequently, if either the UEs or objects in the environment move, the channel coefficients will change. In our thesis, we adopt the common assumption of a time block fading model, i.e., the channel coefficients remain constant during a transmission block of C data symbols and change from coherence interval to coherence interval [43–45, 49, 50]. We call one such block in which the channel remains constant *coherence interval* in the sequel. Moreover, we assume the channel statistics to be constant over time, which is justified by the fact that the large-scale coefficients were observed to change by one or two orders of magnitude slower than the instantaneous channel coefficients [51]. We thus

---

[1]For the ease of notation, but without loss of generality, we assume that M and K is the same in all cells.

[2]We remark that the definition of the channel adopted in this chapter is slightly different from the other parts in our thesis in which we consider the downlink transmission and thus defined the channel of one UE as a row vector.
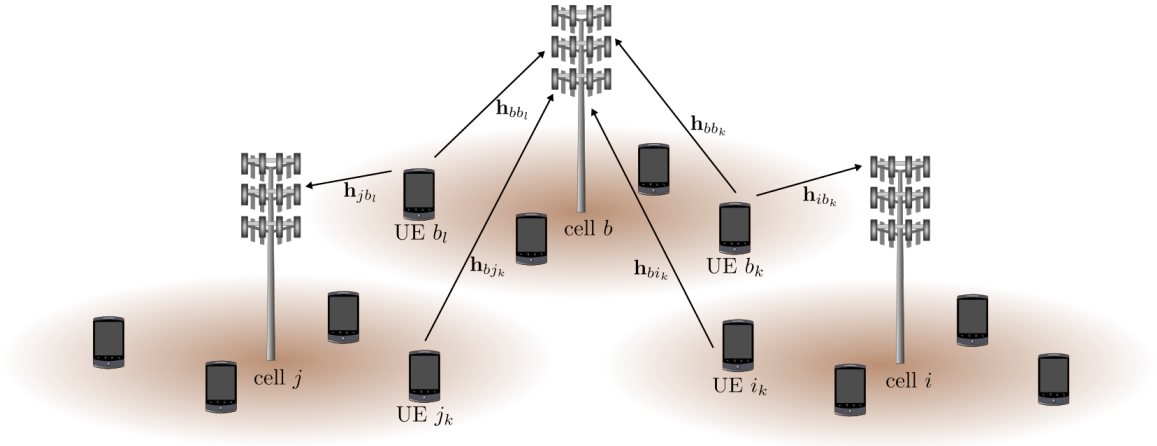
Figure 3.1: Multi-cell system with $B = 3$, $M = 24$, $K = 4$.
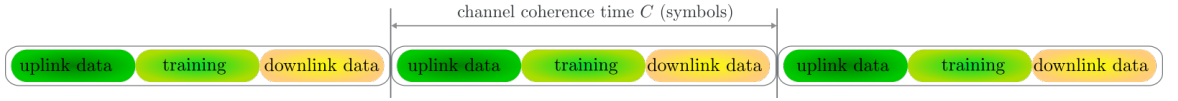
Figure 3.2: Partition of one channel coherence interval C in the three phases.

model the covariance matrix of the channels time-invariant and denote the covariance matrix of the channels between the UEs in cell j cell and the BS in cell b as

$$\boldsymbol{R}_{bj} = \mathbb{E}\left(\bar{\boldsymbol{h}}_{bj}\bar{\boldsymbol{h}}_{bj}^{H}\right), \tag{3.1}$$

where $\boldsymbol{R}_{bj} \in \mathbb{C}^{MK \times MK}$ and $\bar{\boldsymbol{h}}_{bj}$ denotes the vectorized form of $\boldsymbol{H}_{bj}$ obtained by stacking the columns of $\boldsymbol{H}_{bj}$ on top of each other.

3.1.2 Data and Pilot Transmission Model

Channel estimation becomes a challenging task under massive MIMO systems since M coefficients per UE need to be estimated. Therefore, many theoretical works assume a Time-Division Duplex (TDD) operation of massive MIMO systems which reduces the required overhead for channel estimation tremendously [8, 43, 50, 51]. In a TDD system, the coherence interval is split into three phases: the training, uplink data and downlink data phase, respectively (cf. Fig. 3.2). During the training phase, the UEs transmit so-called pilot symbols to the BS. The transmitted pilot symbols are a priori known on both ends of the communication link which facilitates channel estimation at the BS. The BS makes use of the obtained channel estimate to detect the uplink data symbols and precode the downlink data symbols intended for the UEs. It is evident that all three transmission phases have to be carried out within one coherence interval in order to avoid performance degradation due to outdated channel estimates.

During the uplink data phase, the BS in cell b receives the superposition of all data transmitted in all cells:

$$\boldsymbol{Z}_{b} = \sqrt{\gamma}\sum_{j=1}^{B}\boldsymbol{H}_{bj}\boldsymbol{X}_{j} + \boldsymbol{N}_{b}, \tag{3.2}$$

where $\boldsymbol{X}_{j} \in \mathbb{C}^{K \times D}$ contains the D uplink data symbols transmitted by the UEs in cell j on its rows, where we assume that each entry of $\boldsymbol{X}_{j}$ has unit variance, $\boldsymbol{N}_{b} \in \mathbb{C}^{M \times D}$ is the additive complex white Gaussian noise with zero mean and unit variance, and γ is a measure of the SNR.

Moreover, during the pilot transmission phase, the BS in cell b receives a superposition of the training data of all UEs in all cells:

$$\boldsymbol{Y}_b = \sqrt{\gamma} \sum_{j=1}^{B} \boldsymbol{H}_{bj} \boldsymbol{P}_j + \boldsymbol{N}_b, \tag{3.3}$$

where $\boldsymbol{P}_j \in \mathbb{C}^{K \times T}$ contains the T pilot symbols transmitted by the UEs in cell j on its rows and $\boldsymbol{N}_b \in \mathbb{C}^{M \times T}$ denotes the noise as in (3.2).

The pilot sequences of different UEs are required to be orthogonal such that the BS is able to separate the signals of the K UEs in the cell and estimate their channels. In order to achieve orthogonality between the pilot sequences transmitted during the training phase in (3.3), the length of each individual sequences needs to be at least KB, i.e., $T \geq KB$. We recall that pilot transmission needs to be performed in each coherence interval, thus only $C - BK$ symbols are available for uplink and downlink data transmission. Consequently, under massive MIMO systems where the number of supported UEs is large, the training phase would occupy a considerable part of the coherence interval which in turn deteriorates the system performance [8]. Moreover, guaranteeing orthogonality of the training sequences used in different cells requires coordination between the BSs, which might not be possible in any case. Thus, it is usually assumed that the same set of orthogonal pilot sequences is reused in all cells, i.e., $\boldsymbol{P}_j = \boldsymbol{P} \, \forall \, j \in \{1, \dots, B\}$, see e.g. [8, 43, 45, 51, 52]. In this case, it is sufficient to use pilot sequences of length $T \geq K$ to guarantee orthogonality across the UEs within a cell, i.e., $\boldsymbol{P}$ is chosen such that $\boldsymbol{P}\boldsymbol{P}^H = T\boldsymbol{I}_K$. This in turn helps to reduce the training overhead, and coordination among the BSs for pilot assignment is not required anymore. However, this practice fundamentally limits the achievable performance of a massive MIMO system as we will demonstrate next.

3.1.3 Pilot Contamination in Massive MIMO systems

It is well known that large antenna arrays at the BS can help to improve signal detection in the uplink and enable precise beamforming of the downlink signals [8, 10, 22]. If the channels satisfy the favourable propagation conditions described in Eq. (2.7) and the BS has perfect knowledge of the instantaneous channel coefficients, the achievable sum rate performance grows linearly with the number of BS antennas, even when linear detection and precoding algorithms are applied. In particular, the deteriorating effects of additive receiver noise can be mitigated by solely adding more antennas without increasing the transmission power [8, 10, 22]. In a practical multi-cell system, however, this advantageous effect of large antenna arrays is limited due to *pilot contamination* [8–10, 53, 54].

In the sequel, we will illustrate how the performance of a simple linear detection algorithm will suffer from pilot contamination when detecting the uplink data symbols. Although the pilot contamination effect has been explained in several works, see e.g. [8, 9, 55], we will repeat these explanations for the sake of completeness in this thesis. As already mentioned earlier, the same set of pilot sequences is usually reused in all cells of the communication system. Consequently, the BS in cell b will receive the following signal during the training phase

$$\boldsymbol{Y}_b = \sqrt{\gamma} \sum_{j=1}^{B} \boldsymbol{H}_{bj} \boldsymbol{P} + \boldsymbol{N}_b. \tag{3.4}$$

In order to estimate the channel, the BS can apply the traditional matched filtering approach which results in the following estimate of $\boldsymbol{H}_{bb}$

$$\hat{\boldsymbol{H}}_{bb} = \boldsymbol{Y}_b \frac{1}{\sqrt{\gamma T}} \boldsymbol{P}^H = \boldsymbol{H}_{bb} + \sum_{j \neq b} \boldsymbol{H}_{bj} + \boldsymbol{N}_b \frac{1}{\sqrt{\gamma T}} \boldsymbol{P}^H. \tag{3.5}$$

It is easy to see that the channel estimate is contaminated by the interfering channels between the BS in cell b and the users in the neighbouring cells $j \neq b$ as a result of the non-orthogonal sequences used in the different cells. To detect the symbols $\boldsymbol{X}_b$ transmitted during the uplink data phase in Eq. (3.2), the BS can apply the principle of matched filtering again. Without loss of generality, let us consider the estimation of one uplink symbol in the following. To this end, we set $\boldsymbol{X}_j = \boldsymbol{x}_j = (x_{j_1}, \ldots, x_{j_K})^T$, where x_{j_k} denotes the symbol transmitted by user k in cell j with $\mathbb{E}(|x_{j_k}|^2) = 1$. Then, the estimates of the signals of interest are given as

$$\hat{x}_{b_k} = \hat{\boldsymbol{h}}_{bb_k}^H \boldsymbol{Z}_b = \left(\sum_{j=1}^B \boldsymbol{h}_{bj_k} + \bar{\boldsymbol{n}}_{b_k} \right)^H \left(\sum_{j=1}^B \boldsymbol{H}_{bj} \boldsymbol{x}_j + \boldsymbol{n}_b \right), \tag{3.6}$$

where $\hat{\boldsymbol{h}}_{bb_k}$ denotes the k-th column of $\hat{\boldsymbol{H}}_{bb}$, $\bar{\boldsymbol{n}}_{b_k}$ is the k-th column of $\boldsymbol{N}_b \frac{1}{\sqrt{\gamma T}} \boldsymbol{P}^H$ and $\boldsymbol{n}_b$ corresponds to the additive white Gaussian noise with zero mean and unit variance. Let us assume favourable propagation similar to Eq. (2.7) for all the channels, i.e., the interesting and interfering channels. Thus, if M grows to infinity, we have

$$\frac{1}{M} \boldsymbol{H}_{bj}^H \boldsymbol{H}_{bj} \overset{M \to \infty}{=} \boldsymbol{D}_{bj} \ \forall b, j = 1, \ldots, B, \tag{3.7}$$

where $\boldsymbol{D}_{bj} = \mathrm{diag}(d_{bj_1}, \ldots, d_{bj_K})$ and d_{bj_k} denotes the power of the channel between UE k in cell j and the BS in cell b. Then, if $M \to \infty$, the Signal-to-Interference-Plus-Noise Ratio (SINR) of user k in cell b is given as [9]

$$\mathrm{SINR}_{b_k} = \frac{d_{bb_k}^2}{\sum_{j \neq b} d_{bj_k}^2}. \tag{3.8}$$

It is evident from the last expression that the SINR of user k can not be increased by a larger number of antennas at the BS, but it is determined by the power of the interfering channels of those UEs in the adjacent cells which use the same pilot sequence as UE k in cell b. Similar conclusions can be drawn when other linear estimation techniques are used [9].

3.2 Channel Estimation Techniques

In this section, we will now introduce some selected channel estimation techniques. We present a mix between traditional approaches which were extended to massive MIMO systems, and two novel methods which take the problem of pilot contamination into account.

3.2.1 Least Square Estimation

First, we present the Least Squares (LS) estimator as the simplest method estimating the coefficients of $\boldsymbol{H}_{bb}$ from the training signal $\boldsymbol{Y}_b$. The LS estimate of the channels between the BS in cell b and its UEs is obtained by multiplying the received training signal with the conjugate transpose of the

pilot matrix, i.e.,

$$\hat{\boldsymbol{H}}_{bb}^{\text{LS}} = \boldsymbol{Y}_b \frac{1}{\sqrt{\gamma T}} \boldsymbol{P}^H = \boldsymbol{H}_{bb} + \sum_{j \neq b} \boldsymbol{H}_{bj} + \boldsymbol{N} \frac{1}{\sqrt{\gamma T}} \boldsymbol{P}^H. \tag{3.9}$$

It is evident from (3.9) that the LS estimate is contaminated by the channels from the interfering cells due to the sum term in (3.9) as already demonstrated earlier in Chapter 3.1.3. Nevertheless, the estimator does not require any further information but the pilot sequences and is therefore extremely easy to implement. Moreover, the LS estimator does not rely on any asymptotic properties of massive MIMO channels.

3.2.2 Amplitude-Based Blind Pilot Decontamination

To leverage from the benefits provided by a large number of BS antennas, an improved channel estimation technique specifically designed for massive MIMO systems which are subject to pilot contamination was presented in [43]. The basic principle of the so-called *blind channel estimation technique* is as follows. In order to estimate the channels between the BS in cell b and its UEs, the signal received during the training phase is projected onto the subspace spanned by the channels in $\boldsymbol{H}_{bb}$ which eliminates some parts of the additive receiver noise and the contamination caused by the interfering cells. Then, the channels are estimated by applying conventional estimation methods to the projected (decontaminated) training signal.

Let us consider this strategy in more detail. At the beginning, the BS in cell b performs an eigen decomposition of the signals received during the uplink data phase as

$$\boldsymbol{Y}_b \boldsymbol{Y}_b^H = \boldsymbol{U}_b \boldsymbol{\Lambda}_b \boldsymbol{U}_b^H, \tag{3.10}$$

where $\boldsymbol{U}_b \in \mathbb{C}^{M \times M}$ is a unitary matrix and $\boldsymbol{\Lambda}_b$ is a diagonal matrix whose entries are the eigenvalues of $\boldsymbol{Y}_b \boldsymbol{Y}_b^H$ sorted in non-increasing order. From this eigen decomposition, we now aim to find a basis of the subspace spanned by the channels in $\boldsymbol{H}_{bb}$. It was shown in [43] that in the large system limit, i.e., $M \to \infty$, $M \gg K$ and under favourable propagation conditions, the BK largest eigenvalues in $\boldsymbol{\Lambda}_b$ are identical to the Euclidean norms of the BK channel vectors contributing to the signals in $\boldsymbol{Y}_b$. From a physical point of view, it is justified to assume that the norms of the channels in $\boldsymbol{H}_{bb}$ (i.e. the channels of interest) are larger than that of the channels in $\boldsymbol{H}_{bj} \forall j \neq b$ (i.e. the interfering channels) as a result of perfect power control and power-controlled handoff strategies [43]. Consequently, the first K eigenvectors in $\boldsymbol{\Lambda}_b$ correspond to the norms of the channels to be estimated. Hence, the corresponding eigenvectors, i.e., the first K columns of $\boldsymbol{U}_b$, subsequently combined in the matrix $\boldsymbol{E}_b = (\boldsymbol{u}_{b_1}, \boldsymbol{u}_{b_2}, \dots, \boldsymbol{u}_{b_K}) \in \mathbb{C}^{M \times K}$, constitute an orthogonal basis of the estimated channel subspace $\boldsymbol{H}_{bb}$. In order to estimate the actual channel coefficients, the detected training signal $\boldsymbol{Y}_b$ is then projected onto the subspace spanned by $\boldsymbol{E}_b$. This projection eliminates the interfering signals caused by the pilot transmission in adjacent cells and thus mitigates the effect of pilot contamination. Additionally, significant contributions of the additive receiver noise are cancelled out due to the reduction of the signal dimensions [43]. The estimate of $\boldsymbol{H}_{bb}$ is then obtained by means of conventional LS estimation applied to the decontaminated training signal, i.e.,

$$\hat{\boldsymbol{H}}_{bb}^{\text{AM}} = \frac{1}{\sqrt{\gamma T}} \boldsymbol{E}_b \boldsymbol{E}_b^H \boldsymbol{Y}_b \boldsymbol{P}^H. \tag{3.11}$$

The above scheme technically combats pilot contamination on the basis of power differences

among the channels of interest and the interfering channels. Hence, the effectiveness of the method decreases if the signals of UEs using the same pilot sequence have similar received powers at the BS, a case which might occur if both UEs are closely located at the cell edges. Nevertheless, the blind subspace estimation is a formidable example demonstrating how to leverage from the advantages of large antenna arrays under favourable propagation environments.

3.2.3 DFT-Based Blind Pilot Decontamination

To further improve the performance of the blind channel estimation technique described in the last section, [45] presented an extension which aims to separate the interesting and interfering signals by exploiting angular properties of the channels. It was suggested to increase the accuracy of the estimate of $\boldsymbol{H}_{bb}$ by filtering the amplitude-based estimate $\hat{\boldsymbol{H}}_{bb}^{\mathrm{AM}}$ from (3.11) in the frequency domain. This suggestion is based on the observation that the power of a channel with limited angular support is concentrated in a confined frequency range. Moreover, the frequency ranges of channels with disjoint angular support were observed to be non-overlapping which enables the cancellation of undesired signals [45].

We explain the technical implementation of this strategy in the following. To begin with, we write down the conventional Discrete Fourier Transform (DFT) matrix whose modified version is used for the filtering procedure later:

$$\boldsymbol{F} = (\boldsymbol{f}_0, \boldsymbol{f}_1, \ldots, \boldsymbol{f}_{M-1}) = \begin{pmatrix} 1 & 1 & 1 & \ldots & 1 \\ 1 & \omega & \omega^2 & \ldots & \omega^{M-1} \\ 1 & \omega^2 & \omega^4 & \ldots & \omega^{2(M-1)} \\ \vdots & \vdots & \vdots & \ddots & \vdots \\ 1 & \omega^{M-1} & \omega^{2(M-1)} & \ldots & \omega^{(M-1)(M-1)} \end{pmatrix}, \qquad (3.12)$$

where we denote the columns of $\boldsymbol{F}$ as $\boldsymbol{f}_m = (\omega^0, \omega^{1 \cdot m}, \omega^{2 \cdot m}, \ldots, \omega^{(M-1) \cdot m})^T$ and $\omega = \exp\left(\frac{-j 2\pi}{M}\right)$. Our goal is to design a filter matrix which cancels out all contributions originating from the undesired channels in $\boldsymbol{H}_{bj} \forall j \neq b$. Since we do not know a priori which frequency ranges the powers of the channels in $\boldsymbol{H}_{bb}$ are concentrated in, we need to consult a coarse estimate of $\boldsymbol{H}_{bb}$. For instance, such a "pre-estimate" can be obtained from (3.11) for the current and preceding channel realizations. Assuming that N such estimates are available, we now design a filter matrix $\boldsymbol{F}_{\mathcal{F}_{b_k}}$ for each user k which retains only the contributions of the corresponding channel $\boldsymbol{h}_{bb_k}$. To this end, we project the N coarse channel estimates, subsequently denoted as $\tilde{\boldsymbol{h}}_{bb_k}(n)$, onto the basis vectors of the DFT matrix and keep only these columns $\boldsymbol{f}_m$ of $\boldsymbol{F}$, for which the empirical mean power of the projected channel estimate is larger than a certain fraction $\mu \in [0, 1]$ of the mean power of the original version $\tilde{\boldsymbol{h}}_{bb_k}(n)$. More specifically, for user k we obtain the filter matrix $\boldsymbol{F}_{\mathcal{F}_{b_k}}$ from $\boldsymbol{F}$ by keeping only those columns of $\boldsymbol{F}$ whose indices are contained in the set

$$\mathcal{F}_{b_k} = \left\{ m : \sum_{n=1}^{N} \left| \boldsymbol{f}_m^H \tilde{\boldsymbol{h}}_{bb_k}(n) \right|^2 > \mu \sum_{n=1}^{N} \left| \tilde{\boldsymbol{h}}_{bb_k}(n) \right|^2, 0 \leq m \leq M - 1 \right\}. \qquad (3.13)$$

Then, the projection matrix of user k is given as

$$\boldsymbol{\Pi}_{b_k} = \boldsymbol{F}_{\mathcal{F}_{b_k}} \boldsymbol{F}_{\mathcal{F}_{b_k}}^H \qquad (3.14)$$

and we collect the projection matrix of the UEs in cell b in the block diagonal matrix

$$\tilde{\boldsymbol{F}}_b = \text{diag}(\boldsymbol{\Pi}_{b_1}, \boldsymbol{\Pi}_{b_2}, \ldots, \boldsymbol{\Pi}_{b_K}). \tag{3.15}$$

Eventually, the improved estimate of $\boldsymbol{H}_{bb}$ is computed as

$$\hat{\boldsymbol{h}}_{bb}^{\text{AD}} = \tilde{\boldsymbol{F}}_b \hat{\boldsymbol{h}}_{bb}^{\text{AM}}, \tag{3.16}$$

where $\hat{\boldsymbol{h}}_{bb}^{\text{AM}} = \text{vec}\left(\hat{\boldsymbol{H}}_{bb}^{\text{AM}}\right)$ is the vectorized channel estimate from (3.11).

The method described above aims to further improve the blind estimate from Eq. (3.11) by exploiting the knowledge about the channel realizations in previous coherence intervals. Even though this information is readily obtainable at the BS, no improvements can be expected when the power spectra of the channels fluctuate considerably. Moreover, the performance of this method heavily depends on the underlying channel model since it requires the power spectra of the interesting and interfering channels to be clustered in non-overlapping frequency intervals. This issue is elaborated later in Chapter 3.3.3.

3.2.4 MMSE Estimation with Polynomial Expansion

The last channel estimation technique investigated in this thesis is the traditional Minimum Mean Square Error (MMSE) estimator and two modified versions.

The MMSE estimator in its traditional form is given as [51]

$$\hat{\boldsymbol{h}}_{bb}^{\text{MMSE}} = \boldsymbol{R}_{bb} \overline{\boldsymbol{P}}^H \left(\overline{\boldsymbol{P}} \boldsymbol{R}_{bb} \overline{\boldsymbol{P}}^H + \boldsymbol{S}_b \right)^{-1} \boldsymbol{y}_b, \tag{3.17}$$

where $\boldsymbol{y}_b = \text{vec}(\boldsymbol{Y}_b)$ is the vectorized form of the received training signal, $\overline{\boldsymbol{P}} = \frac{1}{\sqrt{\gamma T}} \boldsymbol{P}^T \otimes \boldsymbol{I}_M$, $\boldsymbol{R}_{bj}$ is the covariance matrix defined in (3.1) and the covariance matrix of the contaminating signal is given as

$$\boldsymbol{S}_b = \sum_{j=1, j \neq b}^{B} \overline{\boldsymbol{P}} \boldsymbol{R}_{bj} \overline{\boldsymbol{P}}^H + \boldsymbol{I}_{MT}. \tag{3.18}$$

We conclude from (3.18), that the MMSE estimator in (3.17) exploits the knowledge of the SNR and the channel statistics of the interesting and interfering channels. Since these quantities change only slowly over time, we assume that $\boldsymbol{R}_{bb}$ and $\boldsymbol{S}_b$ are perfectly known at the BS [51].

In order to reduce the complexity of the MMSE receiver, which is mainly determined by the computation of the matrix inverse in (3.17), we present two approaches originally proposed in [51] in the following. It is well known that the inverse of a diagonal matrix is simply obtained by inverting each element on the diagonal. Thus, a straightforward method to decrease the complexity of the MMSE estimator is to diagonalize the covariance matrices, i.e., to set all off-diagonal elements of $\boldsymbol{R}_{bb}$ and $\boldsymbol{S}_b$ to zero. Consequently, the diagonalized MMSE estimator is given as

$$\hat{\boldsymbol{h}}_{bb}^{\text{diag}} = \boldsymbol{R}_{bb}^{\text{diag}} \overline{\boldsymbol{P}}^H \left(\overline{\boldsymbol{P}} \boldsymbol{R}_{bb}^{\text{diag}} \overline{\boldsymbol{P}}^H + \boldsymbol{S}_b^{\text{diag}} \right)^{-1} \boldsymbol{y}_b, \tag{3.19}$$

where $\boldsymbol{R}_{bb}^{\text{diag}}$ and $\boldsymbol{S}_b^{\text{diag}}$ are obtained by setting all off-diagonal elements of $\boldsymbol{R}_{bb}$ and $\boldsymbol{S}_b$ to zero. We remark that the diagonailzation of the covariance matrices is accompanied by a loss of information, which in turn results in considerable performance degradation of the estimator in (3.19) compared to the original version (3.17) if the off-diagonal entries of the original matrices $\boldsymbol{R}_{bb}$ and

S_b significantly deviate from zero.

The authors in [51] thus proposed to compute the matrix inverse in (3.17) by means of a L-degree polynomial approximation which helps reduce the computational complexity of the estimator while the information contained in the off-diagonal elements of R_{bb} and S_b can still be exploited. This approach leads to the so-called Polynomial Expansion Channel Estimator (PEACH):

$$\hat{h}_{bb}^{\text{PEACH}} = R_{bb}\overline{P}^H \sum_{l=0}^{L} \alpha \left(I_{MT} - \alpha \left(\overline{P}R_{bb}\overline{P}^H + S_b \right) \right)^l y_b,$$

(3.20)

where the constant α is given by

$$\alpha = \frac{2}{\text{tr}\left(\overline{P}R_{bb}\overline{P}^H + S_b \right)}.$$

(3.21)

It can be seen from (3.20), that the PEACH estimator does not involve the computational intensive matrix inversion anymore. We remark that the PEACH estimator approaches the original MMSE estimator in (3.17) for $L \to \infty$, thus L can be chosen such that a desired trade-off between complexity reduction and channel estimation accuracy is achieved [51].

3.3 Simulation Results

In the remainder of this chapter, we evaluate the presented estimation techniques by means of numerical simulations. The focus of our studies in not on the comparison of channel estimation techniques among each other, in fact, we aim to identify the impacts of different channel models on the individual estimators.

3.3.1 Preliminaries

As an indicator of the performance measure of the estimation techniques, we use the Normalized Mean Squared Error (NMSE), defined as

$$\text{NMSE} = 10 \log_{10} \left(\frac{1}{K} \sum_{k=1}^{K} \frac{\|\hat{h}_{bb_k} - h_{bb_k}\|^2}{\|h_{bb_k}\|^2} \right),$$

(3.22)

where h_{bb_k} is the actual channel between UE k in cell b and the BS in cell b and $\hat{h}_{bb_k}$ is its estimate. We note that smaller values for NMSE correspond to a better performance of the investigated estimators.

In the remainder of this chapter, we will refer to the individual estimation techniques described earlier by the abbreviations given in Tab. 3.1. The table also provides the parameters of the estimators used throughout our experiments.

3.3.2 Simulation Setup

In our simulations, we consider a multi-cell system with $B = 7$ cells. The massive MIMO BS is equipped with $M = 64$ antennas and we assume a user population of $K = 9$ UEs in all the cells. During the training phase described in Eq. (3.3), a scaled identity matrix is adopted as a basic pilot matrix in all B cells, i.e., $P_j = KI_K \,\forall j = 1, \ldots, B$. Moreover, the channel realizations are drawn from the four models described in Chapter 2.2.

Table 3.1: Simulated channel estimation techniques.

Estimator	Abbreviation	Simulation Parameters
LS Estimator Eq. (3.9)	LS	not available
Power-Based Blind Estimation Eq. (3.11)	AM	$D = 200$ (# data symbols)
DFT-Based Blind Estimation Eq. (3.16)	AD	$\mu = 10^{-2}/M$, $N = 10$
MMSE Estimator Eq. (3.17)	MMSE	not available
Diagonalized MMSE Estimator Eq. (3.19)	DIAG	not available
PEACH Estimator Eq. (3.20)	PEACH	$L = 15$

For Clarke's model, the number of scatterers is set to $N_S = 15$ as in the preceding chapter. When using the Kronecker model, the correlation matrices in (2.8) are computed according to our parameterization suggested in Chapter 2.3.3. In particular, the channels between the UEs in cell b and their BS (i.e. the elements of $\boldsymbol{H}_{bb}$) are generated using $a_{\mathrm{B}} = 0.3$ and $a_{\mathrm{UE}} = 0.6$, while $a_{\mathrm{B}} = 0.3$ and $a_{\mathrm{UE}} = 0$ is used to generate the interfering channels (i.e. the entries of $\boldsymbol{H}_{bj} \, \forall \, j \neq b$). This setup corresponds to a scenario where the UEs within cell b are co-located and thus have correlated channels, while the interfering UEs are far away, i.e., there is no correlation between the interesting and interfering channels. For the COST 2100 model, the parameter set from [11, Table 7.1] is adopted. To obtain comparable conditions for the Kronecker and COST 2100 model, the UEs of cell b are placed on a circle with five-meter diameter and the distance between BS and the centre of the circle is 50 meters, similar to the simulations in Chapter 2.3.4. Additionally, the interfering UEs are located on a bigger circle with the same centre and a diameter of 200 meters.

We continue to use channel normalization (2.12) which allows us to concentrate on the influence of the different correlation conditions under the models which we discussed earlier in Chapter 2. In addition to the normalization which is performed on all channels, we follow the strategy in [51] and scale the interfering channels, i.e., all matrices $\boldsymbol{H}_{bj} \, \forall \, j \neq b$ by $1/\sqrt{B-1}$. The scaling facilitates the adjustment of the signal-to-interference ratio. In particular, the choice $1/\sqrt{B-1}$ corresponds to the case where the contaminating signal has the same power as the training signals of the interesting UEs, i.e., the signal-to-interference ratio is 0 dB.

3.3.3 Comparison of Estimation Techniques

We now present the performance of the estimation techniques described in Chapter 3.2. We first compare the performance of the estimators among each other. Subsequently, we evaluate the impact of the channel models on the individual techniques.

Performance Differences Due to Estimation Technique

The performance of the estimators listed in Tab. 3.1 is depicted in Fig. 3.3 for the four different channel models. It is evident that the estimation error of all the techniques reduces with increasing SNR. For small SNR values, increasing the power devoted to the training signals helps to reduce the estimation error which is mostly determined by the additive noise in this regime. However, with increasing SNR, the interference due to pilot contamination from the adjacent cells outweighs the effects of the noise. Consequently, the estimation error saturates and can not be further decreased by boosting the power of the training signals. For comparison purposes, we plot the trajectory of the NMSE for a single-cell system (i.e. $B = 1$) under i.i.d. Rayleigh channel conditions in Fig. 3.4. It is evident from the figure, that the saturation effect vanishes if the training signals are

(a) i.i.d. Rayleigh model

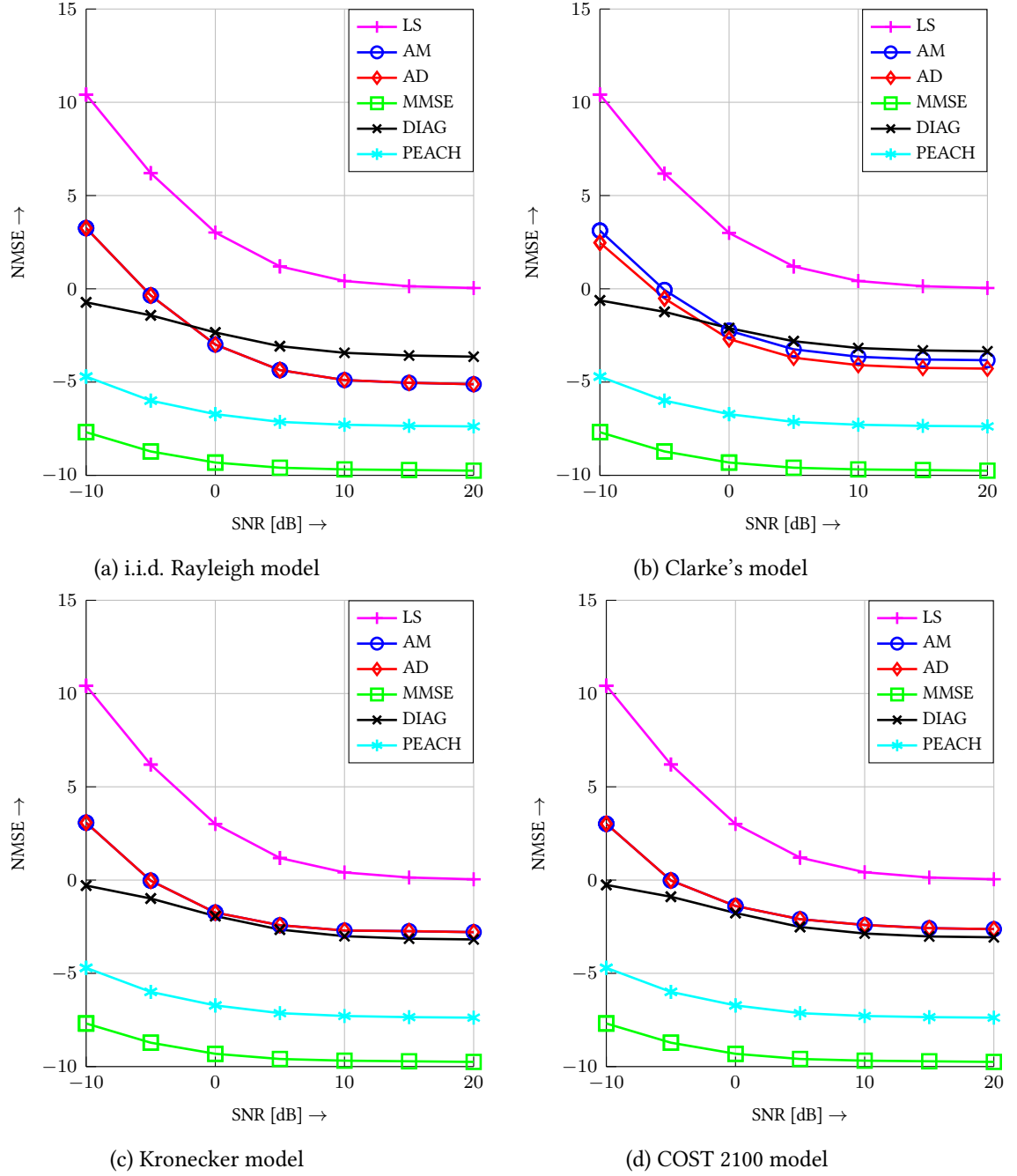(b) Clarke's model

(c) Kronecker model

(d) COST 2100 model

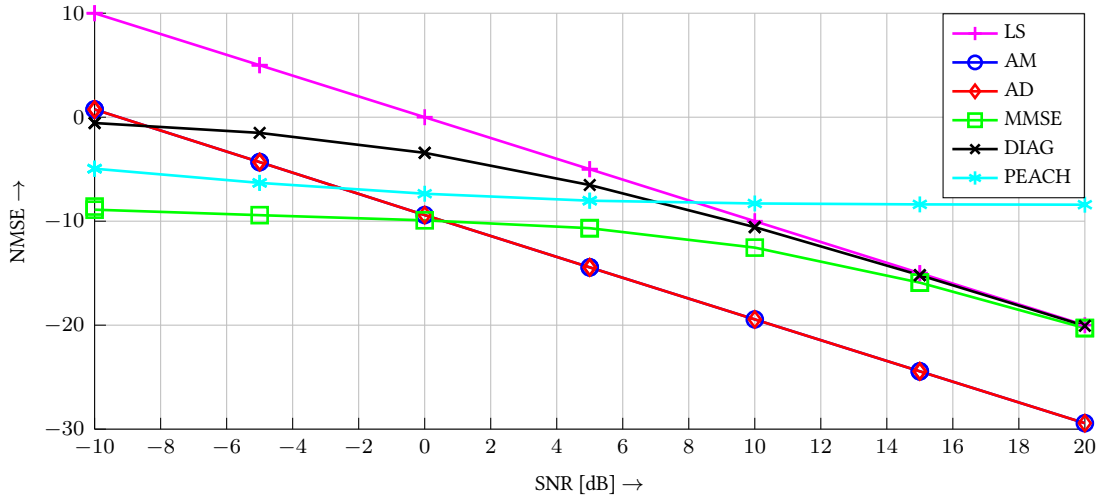Figure 3.3: Performance of channel estimators for $M = 64, K = 9, B = 7$ and different channel models.

Figure 3.4: Performance of channel estimators for i.i.d. Rayleigh model for $M = 64, K = 9, B = 1$ (no pilot contamination).

uncontaminated for all the estimators except the PEACH technique. The saturating estimation performance of PEACH is caused by the error introduced due to the polynomial approximation of the matrix inverse in Eq. (3.20). To overcome this problem, the degree L of the polynomial needs to be increased. The performance gap between the blind techniques and the remaining estimators in the large SNR regime results from the projection of the received training signal onto the subspace spanned by the channels of interest which eliminates large quantities of the additive noise.

When comparing the performances of the different estimation techniques at the same SNR values, we notice differences in terms of estimation error between 10 and 17.5 dB, where LS generally leads to the worst performance and MMSE gives the best results. The considerable performance gap is explained by the fact that LS does not use any information about the wireless channel, while MMSE exploits the channel statistics which were assumed to be perfectly known at the BS. Although the perfect knowledge of the channel statistics is challenging in realistic systems, one can generally assume that at least a very good estimate is available since the statistics vary only slowly over time and can therefore be tracked by the BS [51].

We further conclude from the graphs in Fig. 3.3 that the blind methods AM and AD significantly improve the estimation error over LS by 2.6 to 6.9 dB. This is because the projection of the training signal onto the subspace spanned by the channels of interest, eliminates a considerable contribution of the additive noise and the contaminating signals, which in turn improves the estimation accuracy.

The MMSE and the PEACH estimators provide the best performance under all the channel models. This is intuitively clear, since these estimators are the only ones exploiting the full knowledge about the covariance matrices of the channel of interest and the interfering channels. However, PEACH performs 1.8 to 3.9 dB worse than MMSE which is due to the errors introduced by the polynomial approximation of the matrix inverse in (3.20). The gap between PEACH and MMSE can be reduced by increasing the number of terms, L, used for the polynomial approximation [51]. It is evident that DIAG provides the worst channel estimate among the MMSE-based approaches since it does not make use of the information contained in the off-diagonal elements of the covariance matrices.
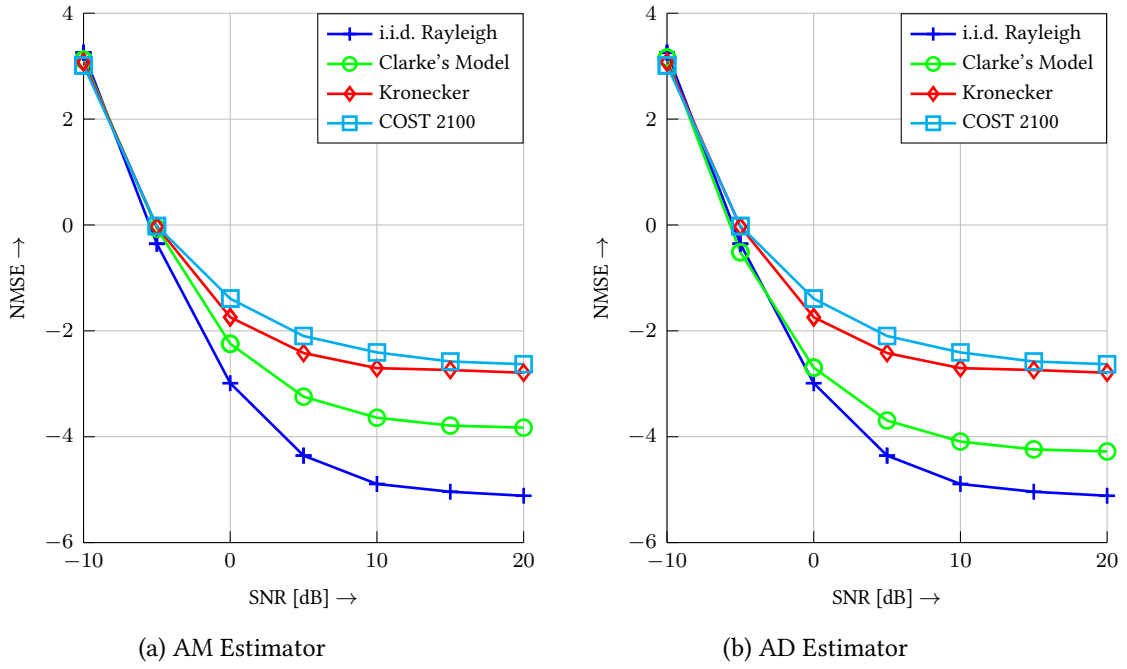
(a) AM Estimator

(b) AD Estimator

Figure 3.5: Performance of selected channel estimators under different channel models.

Performance Differences Due to Channel Model

After the comparison of the different estimation techniques, we now focus on the performance of the estimators under different channel models. To this end, we compare the individual trajectories in Fig. 3.3 across the subplots (i.e. the channel models). First, we observe that the relative performance between the estimators is independent of the channel models for all estimators except the blind approaches AM and AD. While the blind techniques outperform DIAG in the high SNR regime under the i.i.d. Rayleigh and Clarke's model, they deliver worse estimates than DIAG under the more realistic channel models.

To further elaborate this issue, we illustrate the performance of AM and AD under the different channel models in Fig. 3.5a and Fig. 3.5b, respectively. We notice that both strategies perform up to 2.4 dB better under the idealistic i.i.d. Rayleigh and Clarke channel than under the realistic channels. In particular, for SNR > 0 dB, the techniques are degraded by about 1.3 dB to 2.3 dB for the correlated Rayleigh model and by about 1.6 dB to 2.5 dB for COST 2100 model, when compared to the i.i.d. Rayleigh model. The similar amount of degradation between the correlated Rayleigh and COST 2100 models is because the SVS of COST 2100 and Kronecker are much closer to each other than to that of the i.i.d. model (cf. Fig. 2.10 in the last Chapter). This clearly demonstrates the sensitivity of the AM and AD techniques to the underlying modelling approach. The reason for this behaviour is rooted in the original derivations of the estimators, which were based on the i.i.d. Rayleigh model and exploited the favourable propagation conditions offered when M grows large (cf. [43, 45]). However, as we have learned in Chapter 2 (and as can be seen in Fig. 2.10 for this particular case), favourable propagation conditions similar to the i.i.d. Rayleigh model are only observed under Clarke's channel model and the more realistic Kronecker and COST 2100 model exhibit correlation among the channels. Thus, the blind estimation of the subspace involved in AM and AD is subject to performance degradation under more realistic channels.

Another interesting observation from the graphs in Fig. 3.3 is that the AD technique shows only minimal performance improvement over AM when Clarke's model is adopted and no improvement

at all under the remaining models. To explain this issue, we investigate the power spectra of the UE channels in more detail. To this end, we plot in Fig. 3.6 the normalized[3] channel power spectrum of the channels of three randomly selected UEs for one exemplary channel realization drawn from the different channel models. Let us first consider the channels drawn from Clarke's model in which case AD does outperform AM. It can be inferred from the power spectrum in Fig. 3.6b, that the UEs can be separated by their channel powers in the frequency domain. In fact, the power of the individual UE channels is concentrated in different frequency ranges, thereby enabling improved cancellation of signals of the UEs by the filter matrix described in Eq. (3.15). We recall, that the authors in [45] originally assumed channels with limited, non-overlapping angular support, i.e., the dominant signal parts of a UE impinge with very similar angles at the BS array, whereas the signals of the individual UEs arrive with different angles. Under such circumstances, the channel powers of the UEs are concentrated in non-overlapping frequency ranges which facilitates the cancellation of interfering signals in the frequency domain. Even though Clarke's model does not generate channels with limited, non-overlapping angular support, each channel has a "discrete" angular support. This can be concluded from Eq. (2.9) in Chapter 2.2.2 which shows that each channel coefficient is obtained by the summation of N_S waves with randomly chosen angle of arrival. Clearly, with growing N_S, it will become increasingly difficult to separate the UEs by the AD technique, even under Clarke's model. Since Clarke's model converges to the i.i.d. Rayleigh model for $N_S \to \infty$, we immediately conclude that AD will not outperform AM under i.i.d. Rayleigh channels. Unfortunately, even the very realistic COST 2100 model does not result in channels with discrete or limited angular support since the MPCs contained in each channel usually originate from more than one scatterer as explained earlier in Chapter 2.2.3.

To conclude our studies, we turn our focus to the performance of DIAG under the different models. Fig. 3.3 reveals that DIAG experiences a slight performance degradation of about 0.4 dB over the entire SNR range when operating under Kronecker and COST 2100 channel conditions compared to i.i.d. Rayleigh and Clarke channels. This observation is intuitive since the covariance matrices $\boldsymbol{R}_{bb}$ and $\boldsymbol{S}_b$ are closer to diagonal matrices in the case of i.i.d. Rayleigh and Clarke rather than under Kronecker and COST 2100 channels, as a result of the different underlying assumptions on the correlation between the channel coefficients. Hence, the error introduced due to the use of $\boldsymbol{R}_{bb}^{\mathrm{diag}} \, \boldsymbol{S}_b^{\mathrm{diag}}$ in Eq. (3.19) is larger under the two latter models.

In summary, our simulations demonstrate that the performance of traditional estimation techniques such as LS and MMSE are not affected by the underlying channel model. However, the blind estimation techniques specifically derived for massive MIMO systems indeed exhibit a non-negligible sensitivity to the properties of the propagation channels. Moreover, the DIAG approach is sensitive to the channel correlation in the system by construction.

3.4 Conclusion

In this chapter, we examined the effect of the channel models presented in Chapter 2 on the performance of massive MIMO channel estimation techniques. We numerically evaluated the performance of selected channel estimation techniques under different channel models. We discovered that the blind channel estimation techniques and the diagonalized MMSE estimator are sensitive to the underlying channel model. The three techniques show a noticeable degradation in performance

---

[3]We obtained the normalized power spectrum of the channel $\boldsymbol{h}_{bb_k}$ by computing the Fourier transform of $\boldsymbol{h}_{bb_k}$ and dividing it by $|\boldsymbol{h}_{bb_k}|^2$.

(a) i.i.d. Rayleigh model

(b) Clarke's model

(c) Kronecker model
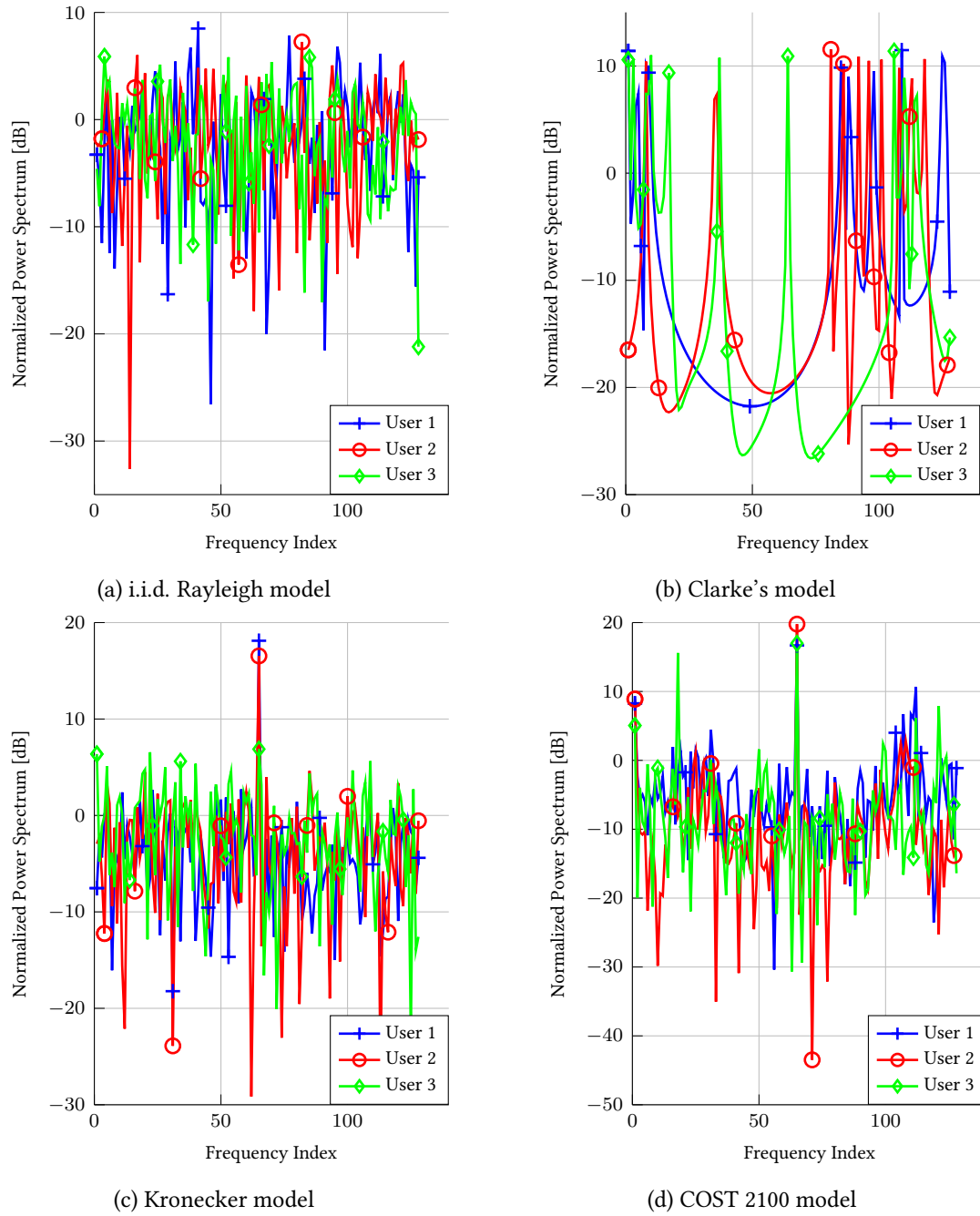
(d) COST 2100 model

Figure 3.6: Normalized power spectrum of three randomly selected UEs.

for realistic channel models with spatial correlation compared to the traditional i.i.d. Rayleigh and Clarke model. Furthermore, we demonstrated that the traditional LS and MMSE estimator and its PEACH approximation perform almost equally well under all the models.

4 DL Scheduling for IoT scenarios

The IoT is envisioned to connect a plethora of devices to the global communication network and its support is an integral part in the development of new 5G cellular networks. Massive MIMO transmission is considered as a potential enabler for cellular IoT as it allows spatial multiplexing of a large number of devices. The following chapter of this thesis focuses on the problem of user selection and fair scheduling for massive MIMO systems to support IoT application scenarios. Specifically, a method serving the IoT users consecutively in groups is proposed, where the group sizes are derived from the optimal number of active users in the zero-forcing downlink channel. The group members are selected by a modified version of the popular Semi-Orthogonal User Selection (SUS) algorithm. To illustrate the origin and need of the introduced modifications, the shortcomings of the original SUS algorithm when operating in a massive MIMO system are identified and elucidated. The new method is evaluated by means of numerical simulations which indicate the suitability of the proposed joint grouping and scheduling algorithm for massive MIMO IoT systems.

Selected parts of this chapter have been submitted for publication in the IEEE Wireless Communication Letters journal. The manuscript was under revision at the time of writing.

4.1 System Model for Downlink IoT Scenarios

In this chapter, we focus on the downlink data transmission in a single-cell wireless communication system. As in the preceding chapters, the massive MIMO BS is equipped with M antennas while the UEs have only one antenna. We assume the BS and all the UEs to be fully synchronized. Our studies focus on highly populated systems where the user population in the cell is larger than M, i.e., $M > K_{\text{cell}}$, where K_{cell} denotes the number of UEs located in the cell. In the following, we will denote the set of all UEs in the cell as

$$\mathcal{K}_{\text{cell}} = \{1, 2, \ldots, K_{\text{cell}}\}. \tag{4.1}$$

The downlink channels between the BS and users are described by the channel matrix $\boldsymbol{H}_{\text{cell}} = \left(\boldsymbol{h}_1^T, \boldsymbol{h}_2^T, \ldots, \boldsymbol{h}_{K_{\text{cell}}}^T\right)^T \in \mathbb{C}^{K_{\text{cell}} \times M}$, where $\boldsymbol{h}_k \in \mathbb{C}^{1 \times M}$ denotes the channel between the k-th user and the BS. As a channel model, we adopt the Kronecker model similar to Eq. (2.8) in Chapter 2.2.1, that is

$$\boldsymbol{H}_{\text{cell}} = \boldsymbol{R}_{\text{U, cell}}^{1/2} \boldsymbol{W} \boldsymbol{R}_{\text{B}}^{1/2}, \tag{4.2}$$

where $\boldsymbol{R}_{\text{B}} \in \mathbb{C}^{M \times M}$ and $\boldsymbol{R}_{\text{U, cell}} \in \mathbb{C}^{K_{\text{cell}} \times K_{\text{cell}}}$ are the correlation matrices at the BS and the users, respectively, and the entries of $\boldsymbol{W} \in \mathbb{C}^{K_{\text{cell}} \times M}$ are independently circularly-symmetric complex Gaussian distributed random variables with zero mean and unit variance. The choice for the channel model is justified by our investigations conducted in Chapter 2, which revealed that the Kronecker model is able to accurately reflect correlation properties and sum rate performance of realistic massive MIMO propagation environments. Throughout this chapter, full knowledge of the

instantaneous channel coefficients and the channel statistics at the BS is assumed, that is, $\boldsymbol{H}_\text{cell}$, $\boldsymbol{R}_\text{B}$ and $\boldsymbol{R}_\text{U, cell}$ are available at the BS.

It is well known, that the precoder leading to the highest sum rate is the so-called dirty paper precoder (DPC) [56]. However, due to the high computational complexity, this non-linear precoding technique can hardly be implemented in practical systems [57]. Therefore, we assume that the BS employs the computational, less expensive ZFBF technique to precode the downlink data signals. Although ZFBF is a sub-optimal precoding technique in general, it can reach near-optimal performance under certain system scenarios [8, 56, 58, 59]. In particular, when $K_\text{cell} \to \infty$, ZFBF with SUS has been shown to reach the same sum rate performance as DPC as an effect of multi-user diversity [56, 58]. Moreover, if $M \to \infty$ and M is much larger than K_cell, serving all the UEs with ZFBF results in optimal sum rate performance due to the spatial diversity provided by the large antenna array [8, 59]. Since ZFBF cancels the interference between the users completely [60], very simple detection algorithms can be employed at the UE side, which in turn facilitates an easier integration of wide-range wireless communication interfaces in typical low-complexity IoT devices [3, 4].

The ZFBF precoding matrix is obtained by the computation of the Moore-Penrose pseudo-inverse of the channel matrix. Therefore, the BS can transmit at most $K \leq M$ independent data streams at a time, where K denotes the number of active UEs. Denoting $\boldsymbol{H} \in \mathbb{C}^{K \times M}$ as the channel matrix of the K active UEs, we express the precoded signals emitted by the BS as

$$\boldsymbol{x} = \gamma \boldsymbol{H}^\dagger \boldsymbol{s} = \boldsymbol{H}^H (\boldsymbol{H} \boldsymbol{H}^H)^{-1} \boldsymbol{s}, \tag{4.3}$$

where $\boldsymbol{s} = (s_1, \ldots, s_K)^T \in \mathbb{C}^{K \times 1}$ contains the K data symbols with unit variance, i.e., $\mathbb{E}\left(|s_k|^2\right) = 1$ and $\boldsymbol{H}^\dagger$ denotes the pseudo-inverse of $\boldsymbol{H}$. The normalization factor γ is chosen such that the transmit power at the BS is fixed to P_BS, that is

$$P_\text{BS} = \text{tr}\left[\mathbb{E}\left(\gamma^2 \boldsymbol{x} \boldsymbol{x}^H\right)\right] = \gamma^2 \, \text{tr}\left[\mathbb{E}\left(\boldsymbol{H}^\dagger \boldsymbol{s} \boldsymbol{s}^H \left(\boldsymbol{H}^\dagger\right)^H\right)\right] = \gamma^2 \, \text{tr}\left[\boldsymbol{H}^\dagger \left(\boldsymbol{H}^\dagger\right)^H\right]. \tag{4.4}$$

Consequently, γ is given by

$$\begin{aligned}
\gamma &= \sqrt{\frac{P_\text{BS}}{\text{tr}\left[\boldsymbol{H}^\dagger \left(\boldsymbol{H}^\dagger\right)^H\right]}} \\
&= \sqrt{\frac{P_\text{BS}}{\text{tr}\left[\boldsymbol{H}^H \left(\boldsymbol{H} \boldsymbol{H}^H\right)^{-1} \left(\boldsymbol{H}^H \left(\boldsymbol{H} \boldsymbol{H}^H\right)^{-1}\right)^H\right]}} \\
&= \sqrt{\frac{P_\text{BS}}{\text{tr}\left[\left(\boldsymbol{H} \boldsymbol{H}^H\right)^{-1}\right]}}.
\end{aligned} \tag{4.5}$$

The signals received at the K active UEs are described as

$$\boldsymbol{y} = \boldsymbol{H} \boldsymbol{x} + \boldsymbol{n} = \gamma \boldsymbol{H} \boldsymbol{H}^\dagger \boldsymbol{s} + \boldsymbol{n} = \gamma \boldsymbol{s} + \boldsymbol{n}, \tag{4.6}$$

where $\boldsymbol{n} \in \mathbb{C}^{K \times 1}$ is the additive white Gaussian noise with zero mean and variance one. Hence, the inter-user interference is cancelled completely and the K active UEs experience the same SNR given by γ.

4.2 Introduction to the User Scheduling Problem and Existing Solutions

The application of user selection strategies in a massive MIMO ZFBF system can provide gains if the excess of BS antennas is small, i.e., $K_{\text{cell}} \approx M$ [59], or the channels of the UEs exhibit correlation among each other [9]. In the IoT scenarios considered in this chapter, user selection is rendered inevitable, since only $K \leq M$ out of the K_{cell} UEs can be served simultaneously by the BS. Therefore, we introduce the user selection problem and review some selected solutions available in literature in the following.

4.2.1 The User Scheduling Problem

User selection strategies are often designed such that the optimal set of users which maximizes the sum rate is found, see e.g. [56, 59, 61–65]. Mathematically, the problem can be formulated as

$$\mathcal{K}_{\text{opt}} = \underset{\mathcal{K} \subseteq \mathcal{K}_{\text{u}}}{\operatorname{argmax}} R(\mathcal{K}), \tag{4.7}$$

where $R(\mathcal{K})$ denotes the sum rate when the UEs in the set $\mathcal{K}$ are served and $\mathcal{K}_{\text{u}}$ denotes the set of UEs available for scheduling.[1] In general, the best set $\mathcal{K}_{\text{opt}}$ depends on the precoder design, the channel conditions, and it can only be found by exhaustive search due to the combinatorial nature of the problem [56, 65]. However, exhaustive search has a prohibitive complexity and can therefore not be applied in practice [62]. In massive MIMO systems, the user selection problem becomes particularly complex owing to the large number of served UEs [9]. For instance, finding the best set of UEs when applying ZFBF requires the evaluation of $\sum_{m=1}^{M} \binom{K_{\text{u}}}{m}$ different combinations of UEs, where $K_{\text{u}} = |\mathcal{K}_{\text{u}}|$ denotes the number of UEs available for scheduling. Even in a moderately-sized massive MIMO system, with e.g. $M = 32$ and $K_{\text{u}} = 50$, the sum rates of more than 10^{15} possible UE combinations have to be evaluated at the BS, which is computationally infeasible. This problem becomes even more pronounced under massive MIMO IoT scenarios, where K_{u} is usually notably larger than M [4, 6].

The above problem formulation does not involve any aspects of fair distribution of resources among the UEs. In particular, serving only the UEs in $\mathcal{K}_{\text{opt}}$ results in a large set of unserved UEs. This is a critical observation which is very significant in IoT scenarios for several reasons. Since K_{u} is usually very large in IoT networks [4, 6] and $|\mathcal{K}_{\text{opt}}| \leq M$, the fraction of UEs being served, namely $|\mathcal{K}_{\text{opt}}| / K_{\text{u}}$, is increasingly small with growing K_{u}, because M is typically fixed. Moreover, a large number of possibly resource starving UEs is undesirable in IoT networks, as it might hinder applications which require the frequent transmission of short control messages to the IoT devices, see e.g. [1, 66–68]. In addition to this, many IoT devices have low or limited mobility [4, 6] and devices such as smart meters and many smart city appliances do not move at all [1]. Hence, the channel conditions of these devices are quite static and devices with unfavourable channel conditions might never be scheduled. Therefore, we present a scheduling strategy for IoT scenarios which involves the sum rate maximization and the fairness aspect later in Section 4.3.

---

[1]Note that $\mathcal{K}_{\text{u}} = \mathcal{K}_{\text{cell}}$ if all the UEs in the cell are subject to scheduling and no further restrictions apply.

4.2.2 Review of some selected User Scheduling Strategies

User scheduling strategies have been rarely investigated in massive MIMO-related literature. Typically, the assumption $K_{\mathrm{cell}} \leq M$ is made and user scheduling is not considered, see e.g. [8–10,53, 69–71]. As already mentioned, if $M \gg K_{\mathrm{cell}}$, all UEs can be served simultaneously with optimal sum rate performance which renders user scheduling unnecessary. However, if the users are correlated or the excess of BS antennas is small, i.e., $K_{\mathrm{cell}} \approx M$, user scheduling can offer gains in sum rate performance. Thus, [59,63] investigated scheduling strategies for massive MIMO systems, however, only the case when $K_{\mathrm{cell}} \leq M$ was studied. Recently, [61,72,73] presented user scheduling strategies maximizing the sum rate in massive MIMO systems, but fairness aspects have not been considered in these works.

In the following, we will review three selected scheduling strategies available in literature. Subsequently, we will modify and combine the first two methods and present an improved user selection strategy suitable for massive MIMO systems, which also incorporates the fairness aspect. Moreover, the third strategy presented in our brief literature review will serve as a benchmark approach for performance comparisons.

Improved Random User Scheduling

We first review a low-complexity random user selection strategy for massive MIMO ZFBF systems initially presented in [62]. The strategy aims to improve the sum rate performance by finding the optimal number of simultaneously scheduled UEs, denoted as K^*, for a given ZFBF downlink channel. After the computation of K^*, a set of active UEs, denoted as $\mathcal{K}_{\mathrm{a}}$, is randomly chosen from $\mathcal{K}_{\mathrm{u}}$, such that $K_{\mathrm{a}} = |\mathcal{K}_{\mathrm{a}}| = K^*$. The benefit of this approach is its very low computational complexity which is equal to that of traditional random scheduling as long as the channel statistics remain constant.

The authors in [62] first give an expression for K^* which depends only on the channel statistics. For the derivations, a Kronecker channel model as in (4.2) was adopted, where an arbitrary correlation at the BS and uncorrelated UEs, i.e., $\boldsymbol{R}_{\mathrm{U,\,cell}}$ is a diagonal matrix, were assumed. Then, by using large system analysis, i.e., $M, K \to \infty$, the SNR experienced at the K active UEs can be approximated by [57,60,62]

$$\gamma(K) = \frac{P_{\mathrm{BS}} M \phi}{K}, \tag{4.8}$$

where ϕ is the unique solution of

$$\phi = \frac{1}{M}\,\mathrm{tr}\left(\boldsymbol{R}_{\mathrm{B}}\left(\boldsymbol{I}_M + \frac{K\boldsymbol{R}_{\mathrm{B}}}{M\phi}\right)^{-1}\right). \tag{4.9}$$

The value of ϕ can be determined iteratively, such that $\phi = \lim_{k \to \infty} \phi_k$ with

$$\phi_k = \frac{1}{M}\,\mathrm{tr}\left(\boldsymbol{R}_{\mathrm{B}}\left(\boldsymbol{I}_M + \frac{K\boldsymbol{R}_{\mathrm{B}}}{M\phi_{k-1}}\right)^{-1}\right) \forall k \geq 1 \tag{4.10}$$

and $\phi_0 = 1$. By evaluating (4.8) for $K \in \{1, \ldots, M\}$, the value of K^* is found by a one-dimensional search as

$$K^* = \underset{K \in \{1,\ldots,M\}}{\mathrm{argmax}}\ K \log_2\left(1 + \gamma(K)\right). \tag{4.11}$$

Subsequently, the algorithm randomly selects $\mathcal{K}_\mathrm{a} \subseteq \mathcal{K}_\mathrm{u}$ with $|\mathcal{K}_\mathrm{a}| = K^*$ in each scheduling interval.

Note from Eq. (4.8)-(4.11) that K^* depends only on the channel statics and not the instantaneous channel coefficients, thus the knowledge of $\boldsymbol{H}_\mathrm{cell}$ is not needed to perform the scheduling process. Since the channel statistics vary slowly over time, K^* does not need to be recomputed in every scheduling interval. That is, as long as the channel statistics do not change, the proposed selection method has the same computational complexity as conventional random user selection of $\mathcal{O}(1)$ [62].

Although the improved random user selection seems to be a very simple and straightforward approach, it has been shown in [62] that it can outperform even more sophisticated methods, such as SUS. In order to facilitate a deep understanding of this phenomenon, we will introduce the concept of SUS next.

Semi-Orthogonal User Selection (SUS)

The SUS algorithm originally proposed in [56] greedily chooses the UEs such that the channels of the selected UEs are semi-orthogonal and the effective channel gains are maximized. The algorithm was originally developed for conventional MIMO systems, i.e., $M = 2, 4$, and it has been shown that ZFBF combined with SUS reaches optimal performance in such systems if $K_\mathrm{cell} \to \infty$ [56]. SUS has been widely applied, even in massive MIMO systems, see e.g. [59, 62, 63, 65]. However, to the best of our knowledge, the performance of the original algorithm when applied to massive MIMO systems has not yet been studied in great depth. In order to facilitate a deeper understanding of SUS and its behaviour in systems with large M, we review the basic idea of the algorithm in the following.

As input parameters, SUS requires a set of UEs available for scheduling, denoted as $\mathcal{K}_\mathrm{u}$, the channel vectors $\boldsymbol{h}_k \in \mathbb{C}^{1 \times M} \, \forall \, k \in \mathcal{K}_\mathrm{u}$, and the system parameter α determining the desired degree of orthogonality among the selected UEs. As an output, the algorithm provides a set of selected UEs, denoted as $\mathcal{K}_\mathrm{a}$. The procedure of SUS is formally stated in Algorithm 1. Generally, SUS splits the input set $\mathcal{K}_\mathrm{u}$ into two subsets, namely the set of *selected (active) UEs*, $\mathcal{K}_\mathrm{a}$, and the *set of candidate UEs*, $\mathcal{K}_\mathrm{c}$. At the beginning, SUS chooses the user with the largest channel gain from $\mathcal{K}_\mathrm{u}$ according to Eq. (4.13). Subsequently, in each iteration step i, SUS picks the UE with the largest effective channel gain from the set of candidate UEs. To this end, the effective channel gain, i.e., the component of $\boldsymbol{h}_k$ orthogonal to the subspace spanned by the effective channels of the already selected UEs, denoted as $\{\boldsymbol{g}(1), \ldots, \boldsymbol{g}(i-1)\}$, is computed for each candidate UE $k \in \mathcal{K}_\mathrm{c}$. In step two of the iterative procedure, the UE with the largest effective channel gain is then selected according to Eq. (4.13). As a last step, the set of candidate UEs is updated, such that the degree of orthogonality among the effective channels of the already selected UEs and the channels of the candidate UEs is below the pre-determined threshold α (see Eq. (4.14)). The iterative procedure is repeated until either the maximum number of UEs is scheduled, i.e., $\mathcal{K}_\mathrm{a}(i) = M$, or no more candidate UEs are left, i.e., $\mathcal{K}_\mathrm{c}(i) = \emptyset$.

The key-step of SUS is step three in the iterative procedure. Here, the set of candidate UEs, $\mathcal{K}_\mathrm{c}$, is shrunk in each iteration step i, such that the normalized correlation between the channels of the UEs considered for scheduling in the next iteration step and the effective channels of the already selected UEs is bounded by the parameter α. Technically, a third (internal) subset of UEs is created here, namely the set of rejected UEs, denoted as $\mathcal{K}_\mathrm{r}(i)$. At the beginning, this set will be empty,

---

Algorithm 1 Semi-Orthogonal User Selection (SUS) [56]

Input: $\mathcal{K}_{\mathrm{u}}$, $\boldsymbol{h}_k \, \forall \, k \in \mathcal{K}_{\mathrm{u}}$, α

Set $\mathcal{K}_{\mathrm{a}}(0) = \emptyset$, $\mathcal{K}_{\mathrm{c}}(1) = \mathcal{K}_{\mathrm{u}}$, $i = 1$

while $\mathcal{K}_{\mathrm{a}}(i-1) < M \wedge \mathcal{K}_{\mathrm{c}}(i) \neq \emptyset$ **do**

1. Compute component of $\boldsymbol{h}_k$ orthogonal to the subspace spanned by $\{\boldsymbol{g}(1), \ldots, \boldsymbol{g}(i-1)\}$ for each candidate user $k \in \mathcal{K}_{\mathrm{c}}(i)$

$$\boldsymbol{g}_k = \boldsymbol{h}_k - \sum_{j=1}^{i-1} \frac{\boldsymbol{h}_k \boldsymbol{g}(j)^H}{\|\boldsymbol{g}(j)\|^2} \boldsymbol{g}(j) \tag{4.12}$$

Note: for $i = 1$: $\boldsymbol{g}_k = \boldsymbol{h}_k \, \forall \, k \in \mathcal{K}_{\mathrm{c}}$

2. Select the i-th user such that effective channel gain is maximized, i.e.,

$$s = \underset{k \in \mathcal{K}_{\mathrm{c}}(i)}{\operatorname{argmax}} \|\boldsymbol{g}_k\|$$
$$\boldsymbol{g}(i) = \boldsymbol{g}_s \tag{4.13}$$
$$\mathcal{K}_{\mathrm{a}}(i) = \mathcal{K}_{\mathrm{a}}(i-1) \cup \{s\}$$

3. Update $\mathcal{K}_{\mathrm{c}}(i+1)$, the set of users semi-orthogonal to $\boldsymbol{g}(i)$ as

$$\mathcal{K}_{\mathrm{c}}(i+1) = \left\{ k \in \mathcal{K}_{\mathrm{c}}(i) \wedge k \neq s : \frac{\left|\boldsymbol{h}_k \boldsymbol{g}(i)^H\right|}{\|\boldsymbol{h}_k\| \, \|\boldsymbol{g}(i)\|} < \alpha \right\}, \tag{4.14}$$

where $\alpha \in \mathbb{R}$ is a small positive constant.

Set $i \leftarrow i + 1$

end while
return $\mathcal{K}_{\mathrm{a}}(i)$

---

i.e., $\mathcal{K}_{\mathrm{r}}(0) = \emptyset$. Then, in iteration i, if a UE $k \in \mathcal{K}_{\mathrm{c}}(i)$ does not satisfy the inequality in Eq. (4.14), it will not be considered for scheduling anymore in the preceding iterations. More formally, it will be moved from the set $\mathcal{K}_{\mathrm{c}}$ to $\mathcal{K}_{\mathrm{r}}$. In particular, the set of rejected UEs in iteration step i is formally given as

$$\mathcal{K}_{\mathrm{r}}(i) = \mathcal{K}_{\mathrm{r}}(i-1) \cup \left\{ k \in \mathcal{K}_{\mathrm{c}}(i) : \frac{\left| \boldsymbol{h}_k \boldsymbol{g}(i)^H \right|}{\|\boldsymbol{h}_k\| \, \|\boldsymbol{g}(i)\|} \geq \alpha \right\} \; \forall \, i \geq 1. \tag{4.15}$$

Note that once moved to the set $\mathcal{K}_{\mathrm{r}}$, this UE will not be considered as a possible candidate for scheduling again, which has an important implication described next.

The parameter α overtakes the function of controlling the number of scheduled UEs. When $\alpha = 1$, all unscheduled UEs will be considered for scheduling in each iteration step and M UEs will eventually be scheduled.[2] In contrast to this, when α is close to zero, only a small subset of $\mathcal{K}_{\mathrm{c}}(i)$ will be considered in the next iteration $i+1$ and most of the UEs will be reject and moved to $\mathcal{K}_{\mathrm{r}}(i)$. This makes the algorithm very sensitive to the right choice of α, as experimentally observed in many studies [56, 58, 59, 62, 63]. As our investigations in Chapter 4.4.2 further ahead will reveal, this sensitivity becomes even more pronounced under massive MIMO systems and a wrong choice of α can lead to severe performance degradation. Moreover, it should be noted that the optimal choice of α, i.e., the α resulting in best sum rate performance of SUS combined with ZFBF, can only be determined numerically and depends on many system parameters, such as channel conditions, K_{u}, M and P_{BS} [56].

Before moving on to the next scheduling strategy, we briefly want to evaluate the complexity of SUS in terms of number of required Floating Point Operations (FLOPS), where one FLOP is either one complex addition, subtraction, multiplication, division or a comparison. It is clear, that the complexity of the steps performed within the while loop depend on the iteration index i. In particular, step one requires $|\mathcal{K}_{\mathrm{c}}(i)| \, (3M(i-1) + M)$ FLOPS for the computation of $\boldsymbol{g}_k$ for all candidate UEs. Moreover, step two necessitates the evaluation of $|\mathcal{K}_{\mathrm{c}}(i)|$ norms of a $1 \times M$ vector which is equivalent to $2M \, |\mathcal{K}_{\mathrm{c}}(i)|$ FLOPS. The computation of $\mathcal{K}_{\mathrm{c}}(i+1)$ in step three involves the evaluation of $|\mathcal{K}_{\mathrm{c}}(i)| - 1$ normalized inner vector products, i.e., $6M(|\mathcal{K}_{\mathrm{c}}(i)| - 1)$ FLOPS. Since, the iterative procedure is performed at most M times, the overall number of FLOPS required by SUS can be approximated as

$$\mathrm{FLOPS}_{\mathrm{SUS}} = \sum_{i=1}^{M} \left(|\mathcal{K}_{\mathrm{c}}(i)| \, (3Mi + 6M) - 6M \right) \tag{4.16}$$

Since $\mathcal{K}_{\mathrm{c}}(i)$ depends on α, $|\mathcal{K}_{\mathrm{c}}(i)|$ can not be exactly determined analytically [56]. However, $|\mathcal{K}_{\mathrm{c}}(i)|$ can be upper-bounded by setting $\alpha = 1$ which results in $|\mathcal{K}_{\mathrm{c}}(i)| = K_{\mathrm{u}} - i$. Thus, for $K_{\mathrm{u}} \gg M$ we can bound (4.16) by

$$\mathrm{FLOPS}_{\mathrm{SUS}} \leq 3K_{\mathrm{u}}M \sum_{i=1}^{M} i + 6K_{\mathrm{u}}M^2 - 6M^2 = \frac{3}{2}K_{\mathrm{u}}M^2(M+1) + 6K_{\mathrm{u}}M^2 - 6M^2 \tag{4.17}$$

From the last equation we conclude, that the number of FLOPS required for the SUS implementation given in Algorithm 1 scales with $\mathcal{O}(K_{\mathrm{u}}M^3)$. Note that it is possible to implement SUS such that the number of executed FLOPS scales with $\mathcal{O}(K_{\mathrm{u}}M^2) + \mathcal{O}(M^3)$ [74]. This is an important observation, especially in massive MIMO systems where M is large and makes SUS a very practical scheduling

---

[2]If the input set $\mathcal{K}_{\mathrm{u}}$ has less than $M+1$ members, i.e., $K_{\mathrm{u}} \leq M$, then all K_{u} UEs will be scheduled thereby rendering the execution of SUS unnecessary.

approach.

Zero-Forcing with User Selection (ZFS)

As a last scheduling strategy investigated in our literature review, we outline the principle of Zero-Forcing Beamforming with User Selection (ZFS) originally presented in [64]. In order to find the best set of UEs, ZFS directly evaluates Eq. (4.7) and selects the UEs in a greedy manner until no improvement in sum rate performance can be achieved anymore. More formally, ZFS selects the i-th user such that

$$s_i = \underset{k \in \mathcal{K}_{\mathrm{u}} \setminus \mathcal{K}_{\mathrm{a}}(i-1)}{\operatorname{argmax}} R(\mathcal{K}_{\mathrm{a}}(i-1) \cup \{k\}), \tag{4.18}$$

where $\mathcal{K}_{\mathrm{a}}(i)$ denotes the set of UEs which have been selected after iteration i. The sum rate when serving the set $\mathcal{K}$ is hereby given as

$$R(\mathcal{K}) = |\mathcal{K}| \log(1 + \gamma(\mathcal{K})), \tag{4.19}$$

where $\gamma(\mathcal{K})$ is given according to Eq. (4.5) as

$$\gamma(\mathcal{K}) = \sqrt{\frac{P_{\mathrm{BS}}}{\operatorname{tr}\left[\left(\boldsymbol{H}_{\mathcal{K}}\boldsymbol{H}_{\mathcal{K}}{}^{H}\right)^{-1}\right]}}. \tag{4.20}$$

Here, $\boldsymbol{H}_{\mathcal{K}} \in \mathbb{C}^{|\mathcal{K}| \times M}$ denotes the matrix having the channels of the UEs contained in $\mathcal{K}$ as its rows. The procedure of ZFS is summarized in Algorithm 2.

In contrast to SUS, ZFS does not require an additional parameter and performs the selection process based on the channel coefficients only. Moreover, by construction, it is guaranteed that adding a new user to $\mathcal{K}_{\mathrm{a}}$ will never degrade the sum rate performance of ZFS, which is not true for SUS [65]. However, the computational complexity of ZFS is significantly higher than that of SUS, as a result of the repeated computation of the rate $R(\mathcal{K}_{\mathrm{a}}(i) \cup \{k\})$ in Eq. (4.23). Despite the existence of a low-complexity implementation of ZFS (the so-called eZFS method presented in [65]), ZFS is more complex than SUS since the number of required FLOPS, even for eZFS, scales with $\mathcal{O}(K_{\mathrm{u}}M^3)$. Therefore, we consider ZFS as a computationally expensive benchmark strategy, which is unlikely to be implemented in practical massive MIMO systems with large M.

4.3 Joint Grouping and Scheduling in IoT scenarios

In this section, we derive a scheduling approach specifically designed for massive MIMO IoT scenarios. First, we highlight important properties of typical IoT devices which lead us to the basic approach for a fair scheduling strategy serving all the K_{cell} users in a grouped manner. Then, we explain how to split the set of users into groups and select the group members for efficient data transmission.

4.3.1 Basic Approach

In typical IoT scenarios, the wireless cells are expected to be densely populated with a very large number of low-complexity devices [3, 4, 6]. In particular, [4] assumes that a BS should support up to $480\,000$ devices, hence in practical massive MIMO systems, where M is in the range of several tens or even hundreds [9], K_{cell}, is expected to be notably larger than M. Consequently, sum

---

Algorithm 2 Zero-Forcing with User Selection (ZFS) [64]

Input: $\mathcal{K}_{\mathrm{u}}$, $\boldsymbol{h}_k \,\forall\, k \in \mathcal{K}_{\mathrm{u}}$

Find user with largest channel gain:

$$s = \underset{k\in\mathcal{K}_{\mathrm{u}}}{\operatorname{argmax}} \|\boldsymbol{h}_k\| \tag{4.21}$$

Set

$$\mathcal{K}_{\mathrm{a}}(1) = \{s\}$$
$$i = 1 \tag{4.22}$$

while $\mathcal{K}_{\mathrm{a}}(i) < M \wedge \mathcal{K}_{\mathrm{u}}\backslash\mathcal{K}_{\mathrm{a}}(i) \neq \emptyset$ **do**
    Find user with largest contribution to sum rate

$$s = \underset{k\in\mathcal{K}_{\mathrm{u}}\backslash\mathcal{K}_{\mathrm{a}}(i)}{\operatorname{argmax}} R(\mathcal{K}_{\mathrm{a}}(i) \cup \{k\}), \tag{4.23}$$

    where $R(\mathcal{K}_{\mathrm{a}}(i) \cup \{k\})$ is obtained according to Eq. (4.19)

    if $R(\mathcal{K}_{\mathrm{a}}(i) \cup \{s\}) \geq R(\mathcal{K}_{\mathrm{a}}(i))$ **then**
        Set
$$\mathcal{K}_{\mathrm{a}}(i + 1) = \mathcal{K}_{\mathrm{a}}(i) \cup \{s\}$$
$$i \leftarrow i + 1 \tag{4.24}$$

    else
        break
    end if
end while
return $\mathcal{K}_{\mathrm{a}}(i)$

---

rate maximizing scheduling strategy as described in (4.7) result in a high number of unscheduled devices. Thus, such an approach is not able to efficiently support IoT applications which require a frequent transmission of control signals, such as smart traffic systems [66, 67] and other smart city applications [1], or smart health systems [68]. Moreover, the effect of resource-starving UEs becomes even more pronounced if the UEs have very low-mobility and therefore (quasi) static channel conditions, which is typical in IoT scenarios [4, 6].

The majority of IoT devices can be categorized as low-cost machine-type devices of low complexity [3, 4]. Usually, such devices require the frequent transmission of short downlink messages, such as control signals or status updates, see e.g. [1, 66–68]. Therefore, we propose a simple mechanism to serve all the UEs based on Joint Grouping And Scheduling (JGS). In particular, we suggest to accommodate a larger number of Machine-Type Communication (MTC) devices by splitting the transmission interval into several sub intervals and serving a different group of UEs in each sub interval. While decreasing the data rates of the individual users, this procedure enables us to introduce the fairness aspect and avoid resource-starving UEs completely.

More formally, JGS splits the data transmission interval of length T into G equal parts of length T/G, during which $K = K_{\text{cell}}/G$ UEs are served. We restrict ourselves to parts of equal length since it simplifies a fair distribution of resources among the UEs served in different parts. The extension to variable-length intervals to support user groups with different rate requirements is straightforward. In order to ensure fairness among the UEs, we aim to serve all the K_{cell} UEs within one transmission interval and partition $\mathcal{K}_{\text{cell}}$ into G disjoint groups, $\mathcal{K}_g \subseteq \mathcal{K}_{\text{cell}}$, of size $|\mathcal{K}_g| = K \leq M$, such that $\bigcup_{g=1}^{G} \mathcal{K}_g = \mathcal{K}_{\text{cell}}$. As a second scheduling aspect, we adopt the usual objective of sum rate maximization (see e.g. [56, 59, 73, 75]) and attempt to maximize the minimum group throughput:

$$\max_{\mathcal{K}_1, \ldots, \mathcal{K}_G} \min_{g \in \{1, \ldots, G\}} R(\mathcal{K}_g), \tag{4.25}$$

where $R(\mathcal{K}_g)$ is obtained according to Eq. (4.19). We remark, that (4.25) reduces to the basic scheduling problem described in Eq. (4.7) if no fairness aspect is considered, i.e., by setting $G = 1$.

We know from Section 4.2.1, that for $G = 1$ finding the optimal set of served UEs requires an exhaustive search in general. For arbitrary G, solving (4.25) still requires exhaustive search, since the rates $R(\mathcal{K}_g)$ can only be determined after all group members have been selected [56]. We therefore apply the following two-step approach leading to a sub-optimal solution of (4.25).

1. We fix the group sizes of each group to K^*, where $K^* \in \{1, \ldots, M\}$ denotes the optimal number of simultaneously served UEs leading to the highest sum rate. It is important to note that we need to determine K^* before the actual user selection process is carried out. Thus, K^* needs to be independent of the instantaneous channel realization.

2. For each group $g \in \{1, \ldots, G\}$, we greedily select K^* UEs, such that the sum rate of the UEs in $\mathcal{K}_g$ is maximized.

We remark that step one follows the basic principle of the improved random selection strategy presented in Section 4.2.2 to identify appropriate group sizes. Moreover, to further improve the scheduler performance, we make use of available sum rate maximizing user selection strategies in the second step described above. In the following two subsections, we will describe both steps in more detail.
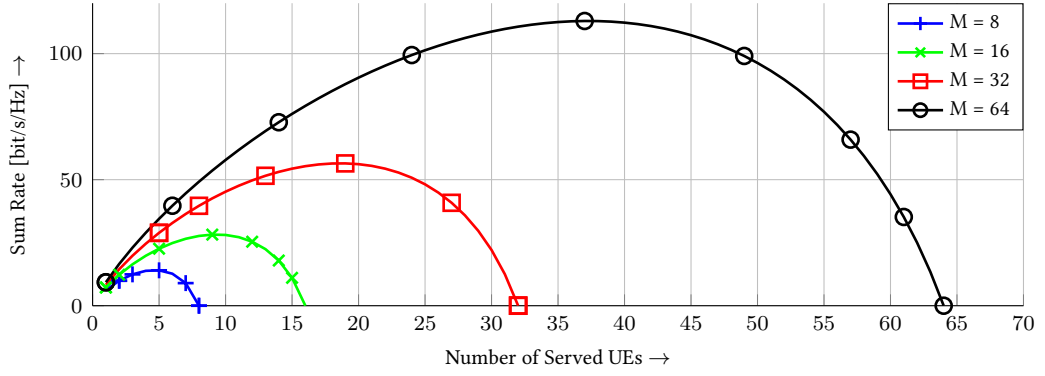
Figure 4.1: Sum rate of ZFBF downlink system versus number of active UEs.

4.3.2 How to Determine Group Sizes

To motivate the introduction of the optimal group sizes K^* in step one of JGS, we consider the ZFBF downlink transmission in a massive MIMO system operating under i.i.d. Rayleigh channel conditions. It has been shown in [8] that in the large system limit, i.e., $M, K \to \infty$ and $M/K =$ const. with $M/K > 1$, the SNR in Eq. (4.5) when serving K UEs simultaneously with equal power allocation can be expressed as $\gamma = P_{\mathrm{BS}} \frac{M-K}{K}$. Hence, the sum rate of the downlink channel is given by

$$
\begin{aligned}
R &= K \log_2 \left(1 + \gamma\right) \\
&= K \log_2 \left(1 + P_{\mathrm{BS}} \frac{M - K}{K}\right).
\end{aligned}
\tag{4.26}
$$

Figure 4.1 illustrates the trajectory of the sum rate in Eq. (4.26) for different numbers of users and antenna settings. The figure demonstrates that the sum rate performance becomes increasingly sensitive to K as the number of BS antennas M grows. Hence, serving an inappropriate number of UEs simultaneously can lead to severe degradation in sum rate performance under massive MIMO systems.

Based on this observation, we therefore suggest to choose the group size in step one of JGS such that the SNR γ of the UEs in $\mathcal{K}_g$ is maximized. To this end, we denote the channels of the K selected UEs as $\boldsymbol{H} \in \mathbb{C}^{K \times M}$ and rewrite the trace-term in Eq. (4.5) as

$$
\mathrm{tr}\left[\left(\boldsymbol{H}\boldsymbol{H}^H\right)^{-1}\right] = \mathrm{tr}\left[\left(\boldsymbol{R}_{\mathrm{U}}^{1/2}\boldsymbol{W}\boldsymbol{R}_{\mathrm{B}}\boldsymbol{W}^H\boldsymbol{R}_{\mathrm{U}}^{1/2^H}\right)^{-1}\right]
\tag{4.27}
$$

$$
= \mathrm{tr}\left[\left(\boldsymbol{D}_{\mathrm{U}}\boldsymbol{U}\boldsymbol{W}\boldsymbol{R}_{\mathrm{B}}\boldsymbol{W}^H\boldsymbol{U}^H\right)^{-1}\right]
\tag{4.28}
$$

$$
= \mathrm{tr}\left[\boldsymbol{D}_{\mathrm{U}}^{-1}\left(\boldsymbol{Q}\boldsymbol{R}_{\mathrm{B}}\boldsymbol{Q}^H\right)^{-1}\right],
\tag{4.29}
$$

where $\boldsymbol{R}_{\mathrm{U}}$ denotes the $K \times K$ correlation matrix of the selected users, $\boldsymbol{R}_{\mathrm{U}} = \boldsymbol{U}\boldsymbol{D}_{\mathrm{U}}\boldsymbol{U}^H$ is its eigenvalue decomposition, and $\boldsymbol{Q} = \boldsymbol{U}\boldsymbol{W}$. We note that $\boldsymbol{Q}$ has the same statistical properties as $\boldsymbol{W}$, since $\boldsymbol{U}$ is a unitary matrix and $\boldsymbol{W}$ is a random matrix with zero mean, unit variance independent Gaussian entries. This enables us to leverage the results from [60, Chapter 14] and express the SNR of the K selected UEs in the large system limit, i.e., for $M, K \to \infty$ and $M/K > 1$ as

$$
\gamma = \frac{P_{\mathrm{BS}} M \phi}{\mathrm{tr}\left(\boldsymbol{D}_{\mathrm{U}}^{-1}\right)}, \quad \phi = \frac{\mathrm{tr}\left[\boldsymbol{R}_{\mathrm{B}}\left(\boldsymbol{I}_M + \frac{K}{M\phi}\boldsymbol{R}_{\mathrm{B}}\right)^{-1}\right]}{M}.
\tag{4.30}
$$

The optimal number of users served is then found by a one dimensional search

$$K^* = \underset{K \in \{1,\dots,M\}}{\operatorname{argmax}} \; K \log_2 (1 + \gamma) \; . \tag{4.31}$$

We observe from (4.30) that γ is indeed independent of the instantaneous channel realizations in the large system limit. However, the SNR in (4.30) depends on the choice of selected users through the eigenvalues $\boldsymbol{D}_{\mathrm{U}}$ of the user correlation matrix. Consequently, in the most general case, it is not possible to determine K^* before the selection process has been carried out and only the expected value $\mathbb{E}\left(\operatorname{tr}\left(\boldsymbol{D}_{\mathrm{U}}^{-1}\right)\right)$ can be consulted. In general, the value of $\mathbb{E}\left(\operatorname{tr}\left(\boldsymbol{D}_{\mathrm{U}}^{-1}\right)\right)$ needs to be computed by numerical evaluation of $\operatorname{tr}\left(\boldsymbol{D}_{\mathrm{U}}^{-1}\right)$ for different sets of users $\mathcal{K} \subset K_{\mathrm{cell}}$ with $|\mathcal{K}| = K$. Fortunately, due to the structure of $\boldsymbol{R}_{\mathrm{U,\,cell}}$ occurring in massive MIMO IoT scenarios, $\boldsymbol{D}_{\mathrm{U}}$ can be assumed to be independent of the actual user selection process in such systems. In particular, as explained earlier in Chapter 2.3.2, the channels of UEs in close proximity exhibit some correlation, while channels of distant UEs are uncorrelated. Moreover, the cells in typical IoT scenarios are expected to be densely populated and the devices can assumed to be geographically clustered. This enables us to arrange $\boldsymbol{R}_{\mathrm{U,cell}}$ as a block-diagonal matrix, where each block describes the user correlation within one cluster of IoT devices, while the correlation between UEs in different clusters is zero. Since step two of JGS is designed such that the UEs resulting in the largest group rate, i.e., the UEs leading to the highest SNR in (4.30), are chosen, the scheduler will choose the least correlated UEs, i.e., UEs from different clusters, for simultaneous data transmission. This in turn renders the resulting submatrix $\boldsymbol{R}_{\mathrm{U}}$ of $\boldsymbol{R}_{\mathrm{U,cell}}$ and hence $\boldsymbol{D}_{\mathrm{U}}$, the SNR (4.30), and thus the optimization (4.31) independent of the specific UE grouping.

4.3.3 How to Find the Group Members

After determining the group sizes based on the channel statistics, we now aim to further improve the sum rate performance by exploiting the knowledge of the instantaneous channel information. The selection of the K^* group members is performed in an iterative manner. In each iteration step, the members of group g are greedily selected from the set $\mathcal{K}_{\mathrm{u}} = \mathcal{K}_{\mathrm{cell}} \backslash \bigcup_{\ell=1}^{g-1} \mathcal{K}_{\ell}$ such that the sum rate of the group is maximized. Note that, if K_{cell} is not a multiple of K^*, the last group G will contain only $\mod\left(K_{\mathrm{cell}}, K^*\right)$ UEs.

To find the group members, we adopt a modified version of the SUS algorithm presented in Chapter 4.2.2. The iterative application of SUS as a strategy serving all the K_{cell} UEs has already been presented in [56]. However, the original SUS algorithm does not allow to determine the number of simultaneously served UEs, and hence G a priori. Moreover, the optimal value of α is used in [56] to guarantee maximum performance. Due to the dependencies of α on K_{u} and the channel conditions, it is however difficult to obtain its optimal value in practical systems. Thus, we suggest a modified version of SUS, called SUS-M in the following, which overcomes the practical limitations of the original algorithm.

As already stated in Chapter 4.2.2, the parameter α overtakes the function of controlling the number of simultaneously served UEs. As the sum rate performance becomes increasingly sensitive to the number of served UEs when M grows (cf. Chapter4.3.2), the impact of α on the performance of SUS increases. However, the optimal number of served UEs becomes more and more predictable when M is large due to the channel hardening effect (cf. Chapter 2.3.2). We exploit this fact to reduce the sensitivity of SUS to α. In particular, we suggest to modify the first termination criteria

of SUS in Algorithm 1 such that at most K^* UEs are served, that is, the condition of the while loop is changed to

$$\mathcal{K}_a(i-1) < K^* \land \mathcal{K}_c(i) \neq \emptyset, \tag{4.32}$$

where K^* is obtained from the large system approximation in Eq. (4.31). Moreover, to completely remove the dependency on α, we set $\alpha = 1$ which means that $\mathcal{K}_c(i) = \mathcal{K}_u \backslash \mathcal{K}_a(i-1)$, i.e. the most orthogonal UEs from the set of all possible UEs are selected. We remark that in the general case, only setting $\alpha = 1$ ensures that all the UEs are served and the group sizes remain fixed to K^*. The procedure of SUS-M is presented in Algorithm 3.

We summarize the procedure of JGS in Algorithm 4. The computational complexity of JGS is mainly determined by the selection process identifying the group members since K^* depends on the channel statistics only and changes slowly over time. In particular, we can state that the complexity of JGS is $G - 1$ times the complexity of the applied user selection algorithm. Hence, the computational cost of JGS as described in Algorithm 4 scales with $(G-1)\,\mathcal{O}(K_{\text{cell}}M^2)$.

It is worth noting that also random selection or ZFS could be used to find the group members in step two of JGS. However, the SUS-based selection provides the best trade-off between computational complexity and scheduler performance.

4.4 Evaluation of Proposed Scheduling Strategy

We now evaluate the performance of JGS via numerical simulations. The experimental setup consists of a single-cell massive MIMO system with $M = 64$ antennas at the BS and a variable number of UEs. We aim to model a challenging, but realistic scenario, in which the IoT devices appear in clusters, i.e., the UEs within a cluster are co-located and there are several such clusters spread out in the cell. In order to model such a scenario realistically, we make use of our results presented earlier and parameterize the Kronecker model in Eq. (4.2) according to the exponential correlation model proposed in Chapter 2.3.3. For the sake of simplicity, we assume the matrices describing the correlation between the UEs within a cluster to be identical across all clusters. For the correlation parameter, we set $a_{\text{UE}} = 0.6$ and the number of UEs in each cluster is assumed to be nine[3]. Consequently, $\boldsymbol{R}_{\text{U, cell}}$ can be written as a block diagonal matrix with the "cluster-correlation" matrices having a structure as in Eq. (2.17) on its diagonal. Furthermore, the exponential correlation model as given in Eq. (2.18) is adopted for $\boldsymbol{R}_{\text{B}}$ in Eq. (4.2), where we set $a_{\text{B}} = 0.3$.[4]

4.4.1 Verification of Large System Approximation of K^*

We first inspect the validity of approximating the optimal number of served UEs by the large system approximation given in Eq. (4.31). To this end, we compare the analytical solution K^* with a numerically determined K_{opt} maximizing the sum rate in the system. We remark that finding the true value of K_{opt} for a given channel realizations requires the enumeration of all possible subsets of $\mathcal{K} \subseteq \mathcal{K}_{\text{cell}}$ with $|\mathcal{K}| \in \{1, \ldots, M\}$ which is not feasible for the given system dimensions. Thus, we determine K_{opt} by random search as follows: for each $K \in \{1, \ldots, M\}$, we select K UEs uniformly at random for N trials and retain the selection with the maximum sum rate. Then, the size of the set corresponding to the largest overall sum rate is chosen as the value for K_{opt}.

---

[3]If K_{cell} is not a multiple of 9, then the last cluster contains only $\text{mod}(K_{\text{cell}}, 9)$ UEs.

[4]The adopted values originate from the experimental setup considered in Chapter 2.3.4, which in turn corresponds to the setup considered in measurement campaign [11].

Algorithm 3 Modified Semi-Orthogonal User Selection (SUS-M)

Input: $\mathcal{K}_{\mathrm{u}}, \boldsymbol{h}_k \, \forall \, k \in \mathcal{K}_{\mathrm{u}}$

Set $\mathcal{K}_{\mathrm{a}}(0) = \emptyset, \mathcal{K}_{\mathrm{c}}(1) = \mathcal{K}_{\mathrm{u}}, i = 1$

while $\mathcal{K}_{\mathrm{a}}(i-1) < K^* \wedge \mathcal{K}_{\mathrm{c}}(i) \neq \emptyset$ **do**

1. Compute component of $\boldsymbol{h}_k$ orthogonal to the subspace spanned by $\{\boldsymbol{g}(1), \ldots, \boldsymbol{g}(i-1)\}$ for each candidate user $k \in \mathcal{K}_{\mathrm{c}}(i)$

$$\boldsymbol{g}_k = \boldsymbol{h}_k - \sum_{j=1}^{i-1} \frac{\boldsymbol{h}_k \boldsymbol{g}(j)^H}{\|\boldsymbol{g}(j)\|^2} \boldsymbol{g}(j) \tag{4.33}$$

   Note: for $i = 1$: $\boldsymbol{g}_k = \boldsymbol{h}_k \, \forall \, k \in \mathcal{K}_{\mathrm{c}}$

2. Select the i-th user such that effective channel gain is maximized, i.e.,

$$s = \underset{k \in \mathcal{K}_{\mathrm{c}}(i)}{\mathrm{argmax}} \|\boldsymbol{g}_k\|$$

$$\boldsymbol{g}(i) = \boldsymbol{g}_s \tag{4.34}$$
$$\mathcal{K}_{\mathrm{a}}(i) = \mathcal{K}_{\mathrm{a}}(i-1) \cup \{s\}$$
$$\mathcal{K}_{\mathrm{c}}(i+1) = \mathcal{K}_{\mathrm{c}}(i) \backslash \{s\}$$

   Set $i \leftarrow i + 1$

end while
return $\mathcal{K}_{\mathrm{a}}(i)$

Algorithm 4 Joint UE Grouping and Scheduling

Input: $\boldsymbol{H}_{\mathrm{cell}}, \boldsymbol{R}_{\mathrm{B}}, \boldsymbol{R}_{\mathrm{U, cell}}$

Set $\mathcal{K}_{\mathrm{u}} = \mathcal{K}_{\mathrm{cell}}, g = 1$
Compute K^* according to (4.31) and set $G = \lceil K_{\mathrm{cell}} / K^* \rceil$
while $g \leq G$ **do**
    if $|\mathcal{K}_{\mathrm{u}}| > K^*$ **then**
        $\mathcal{K}_g = \text{SUS-M}(\mathcal{K}_{\mathrm{u}}, K^*)$
    else
        $\mathcal{K}_g = \mathcal{K}_{\mathrm{u}}$
    end if
    $\mathcal{K}_{\mathrm{u}} \leftarrow \mathcal{K}_{\mathrm{u}} \backslash \bigcup_{\ell=1}^{g} \mathcal{K}_\ell$
    $g \leftarrow g + 1$
end while
return $\mathcal{K}_g \, \forall \, g \in \{1, \ldots, G\}$

Fig. 4.2 shows the empirical distribution of K_{opt} for 10000 channel realizations and $N = 1000$, $M = 64$, $\gamma = 10$ dB and a UE set $\mathcal{K}_{\mathrm{u}}$ of size $K_{\mathrm{u}} = 320$. In addition to the specified correlated channel model, we also show the results of this experiment for an uncorrelated channel model for which $\boldsymbol{R}_{\mathrm{U,cell}} = \boldsymbol{I}_{K_{\mathrm{cell}}}$ and $\boldsymbol{R}_{\mathrm{BS}} = \boldsymbol{I}_M$ in Eq. (4.2). The analytical solution from (4.31) is $K^* = 35$ for the correlated and $K^* = 37$ for the uncorrelated channel model. Hence, we observe that the proposed method, which is derived based on the large system limit, provides a good approximation for the optimal group size also in the case of practical finite-sized systems. Moreover, it is evident that K^* is considerably smaller than M.
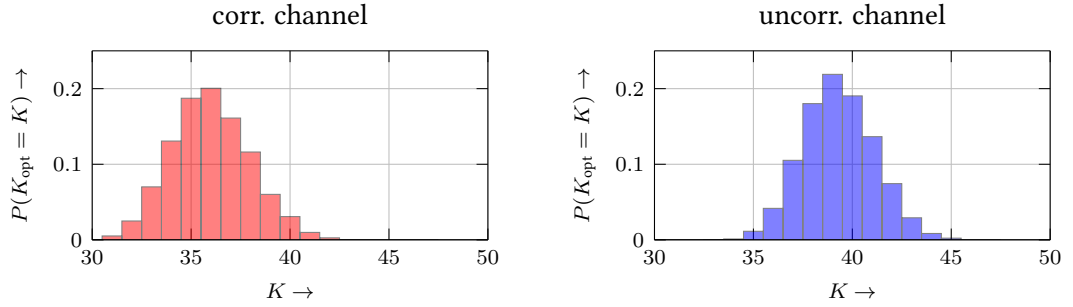
Figure 4.2: Empirical distribution of K_{opt} obtained via numerical simulations for $K_{\mathrm{u}} = 320$ and $M = 64$.

4.4.2 Improvements of SUS-M over SUS

We now illustrate the effects of our proposed modifications to the SUS algorithm. First, we demonstrate the sensitivity of the original SUS algorithm to α under massive MIMO systems. For our simulations, we set $P_{\mathrm{BS}} = 10$ dB. Fig. 4.3a depicts the surface of the sum rate performance of SUS described in Algorithm 1 for $M = 64$ and $K_{\mathrm{u}} \in \{1, \ldots, 320\}$. It is evident from the graph, that the sum rate varies dramatically over α and the optimum value of α changes with K_{u}. This phenomenon can be explained by investigating the number of served UEs, i.e., the value of K_{a} after user selection, which is depicted in Fig. 4.3b. While small values of α restrict the set $\mathcal{K}_{\mathrm{c}}$ too much and only a small number of UEs is served, larger values of α result in $K_{\mathrm{a}} = M$. Consequently, the performance of SUS is highly affected by the choice of α, since the sum rate in a ZFBF system is sensitive to the number of served UEs as demonstrated in Chapter 4.3.2. The trajectory of the sum rate is extremely steep around its maximum value, i.e., at the desired point of operation of SUS. This requires a very accurate choice of α in order to avoid severe performance degradation.

We remark that SUS was originally designed for conventional MIMO systems where M is small, e.g. $M = 2, 4$. In such systems, SUS exhibits good performance over a wide range of α. However, with growing M, the sensitivity of SUS to α increases dramatically. To illustrate this, we plot the sum rate performance versus α for different values of M and $K_{\mathrm{u}} = 4M$ in Fig. 4.4a. Moreover, to illustrate the relative performance loss when α is not chosen properly, we plot the relative sum rate performance, i.e., the sum rate divided by the maximum sum rate achievable for a given M in Fig. 4.4b. It is easy to see from the figures, that for conventional MIMO (i.e. $M = 2, 4$) the relative performance loss due to an improper choice of α is at most 20%. In contrast to this, for a massive MIMO system with $M = 64$, the performance degrades up to 70% for a wrong setting of α. The growing sensitivity is explained by the increased impact of the number of simultaneously served UEs on the sum rate of a ZFBF systems, which was described in Chapter 4.3.2. In particular, SUS serves M UEs when α is sufficiently large, which degrades the sum rate performance in massive
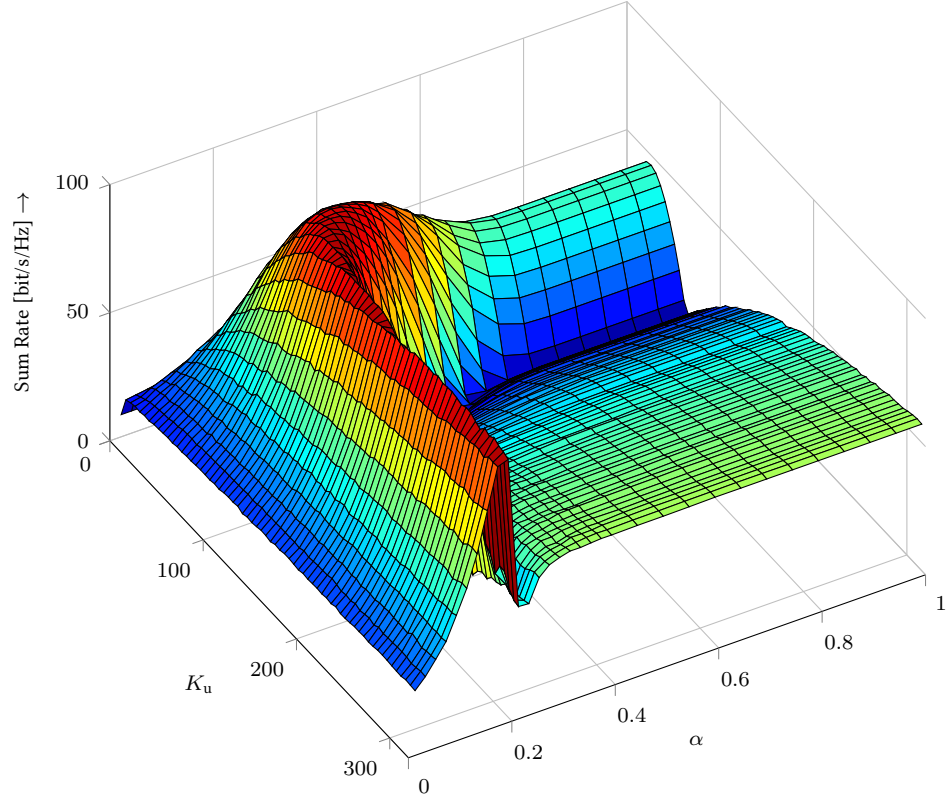
(a) Sum rate performance of SUS (Algorithm 1) for $M = 64$.
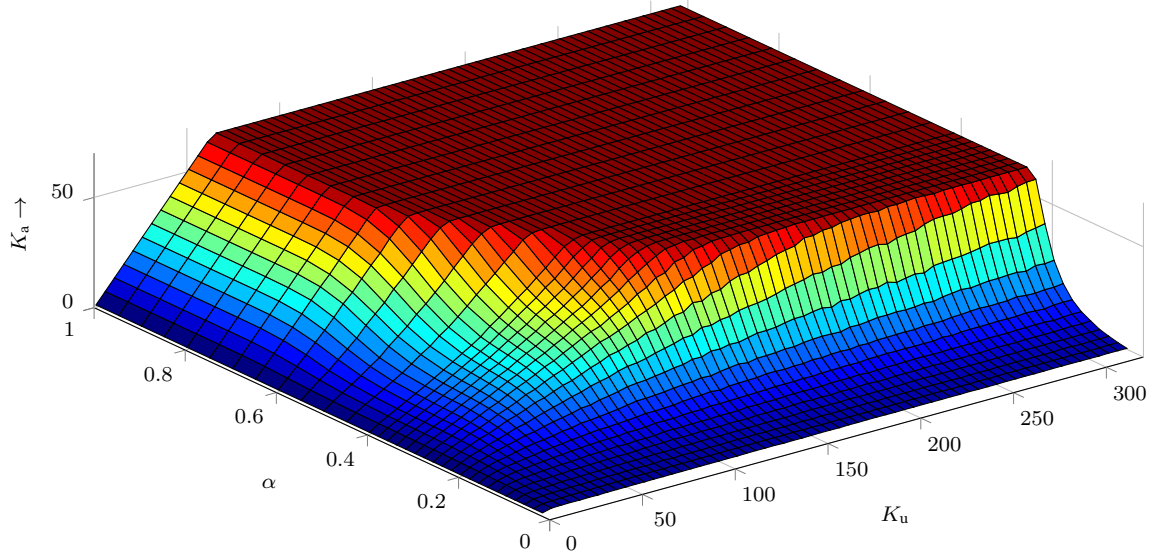
(b) Number of UEs served by SUS in Algorithm 1 for $M = 64$.

Figure 4.3: Performance of SUS averaged over 1000 channel realizations.
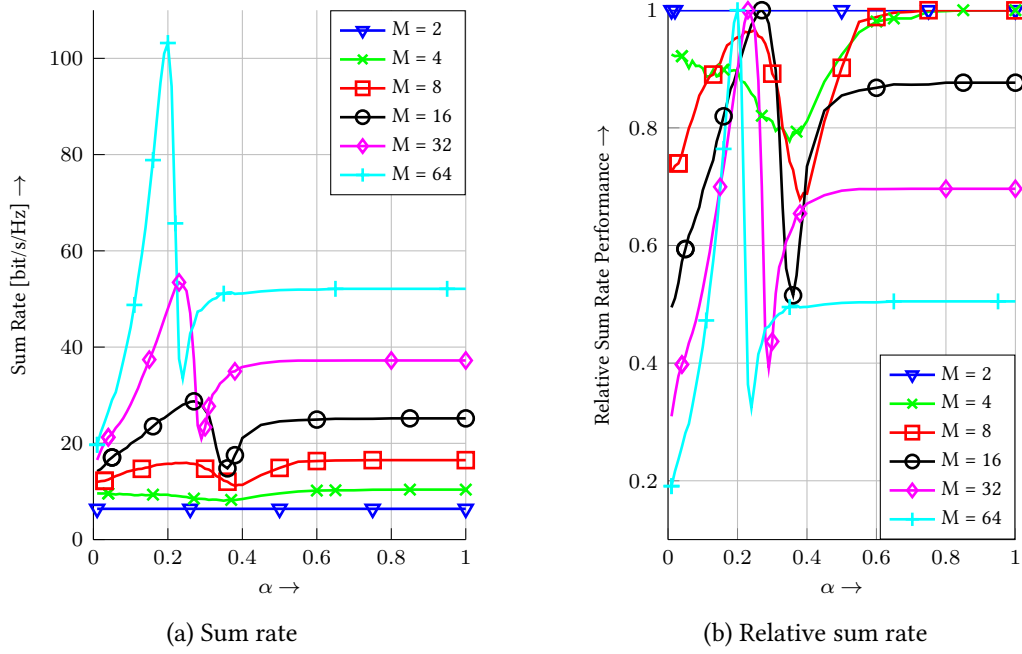
(a) Sum rate

(b) Relative sum rate

Figure 4.4: Sum rate and relative sum rate of SUS for different antenna settings and $K_\mathrm{u} = 4M$.
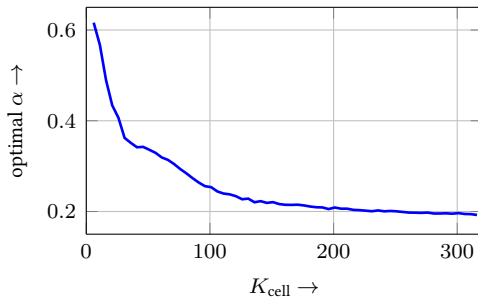
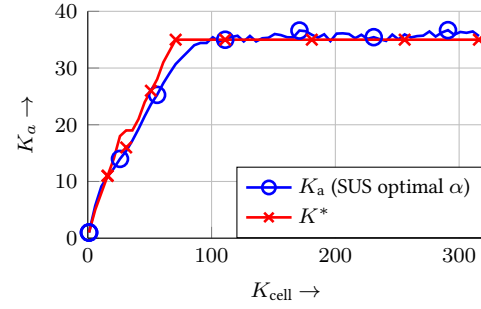Figure 4.5: Optimal value of α versus K_cell with $M = 64$ (extracted from Fig. 4.3a).

Figure 4.6: Number of served UEs when α is optimized (as in Fig. 4.5).

MIMO systems. Thus, a proper choice of α becomes increasingly important when M is large. However, the optimal value of α is difficult to identify in practical systems as the trajectory of the sum rate is very steep (cf. Fig. 4.3a and Fig. 4.4a). Hence, the numerical optimization of α requires very high resolution which increases the computational cost of SUS.

Moreover, we acknowledge from Fig. 4.3a and Fig. 4.5 that the optimal value of α depends on K_u. This renders the application of SUS as a method iteratively selecting the group members in JGS impractical since the optimal α would change for each group index g.

After highlighting the shortcomings of the conventional SUS algorithm occurring in massive MIMO systems, we now demonstrate the beneficial effects of our proposed modifications. To this end, we first assess the validity of the modified termination criteria by investigating the number of UEs served with SUS (i.e. the value of K_a) when α is optimized, i.e., when the largest sum rate is achieved. The values of K_a corresponding to the largest sum rate in Fig. 4.3a versus K_cell are depicted in Fig. 4.6. For comparison purposes, we also plot K^* obtained from Eq. (4.31). It is clear that both trajectories almost coincide. Hence, we conclude that K^* from Eq. (4.31) is a good approximation of the number of UEs naturally served by SUS when α is optimized. This validates the choice of our modified termination criteria in SUS-M.

(a) $M = 32$ (b) $M = 64$
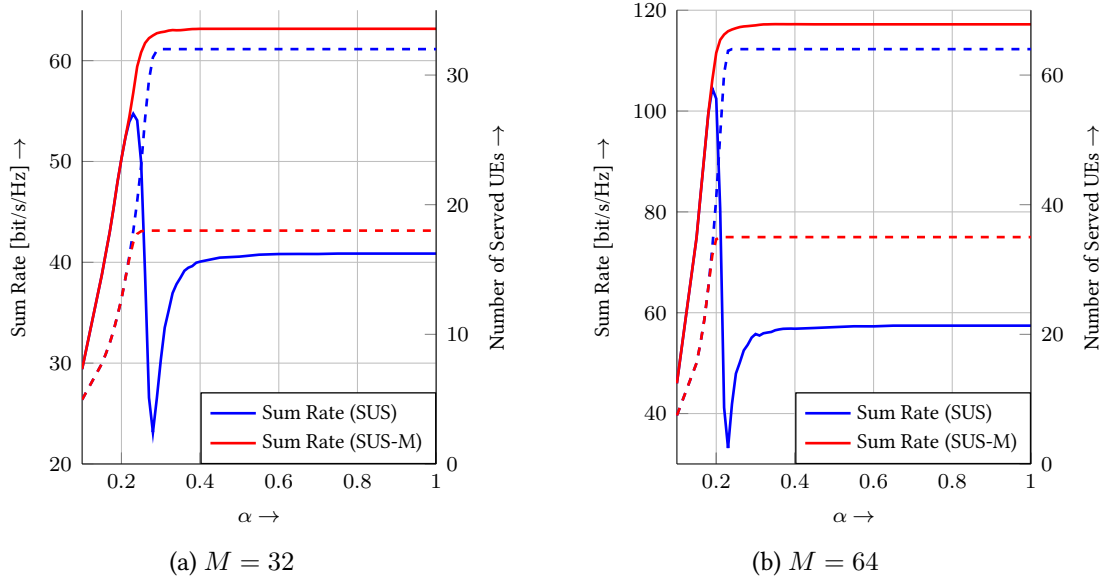
Figure 4.7: Performance of SUS and SUS-M for $K_{\mathrm{u}} = 5M$ averaged over 1000 channel realizations.

Table 4.1: Simulated grouping techniques.

Grouping Technique	Abbreviation	Group Size
Proposed JGS (Algorithm 4)	JGS	K^*
JGS with random group member selection	JGS-RS	K^*
Iterative SUS (Algorithm 1)	G-SUS	variable
Iterative ZFS (Algorithm 2)	G-ZFS	variable

In order to illustrate the validity of our second modification for SUS-M, we plot the performance of the regular SUS algorithm (as shown in Algorithm 1) and that of the SUS algorithm using the modified termination criteria for $\alpha \in [0, 1]$. In particular, we show the sum rate performance and the number of scheduled UEs versus α for both algorithms in Fig. 4.7. We present the results for $M = 32, 64$ and chose the number of available UEs as $K_{\mathrm{u}} = 5M$. While the sum rate of the original SUS algorithm strongly depends on α, the sum rate of SUS-M remains constantly high for increasing α which is a consequence of the improved termination criterion $|\mathcal{K}_{\mathrm{a}}| = K^*$ used in SUS-M. The constantly high sum rate performance of SUS-M justifies our choice of $\alpha = 1$, which allows the algorithm to select the most orthogonal UEs from the unrestricted set $\mathcal{K}_{\mathrm{u}}$.

4.4.3 Performance of JGS

We now turn our focus to the operation of JGS in a massive MIMO IoT system. In our simulations, we consider $M = 64$ and $K_{\mathrm{cell}} \in \{M, \ldots, 500\}$. For comparison purposes, we investigate a different version of JGS, which selects the group members $\mathcal{K}_g$ uniform at random from $\mathcal{K}_{\mathrm{u}}$. Moreover, we study the iterative application of the original SUS Algorithm (with optimal α) and that of the ZFS algorithm. Specifically, we apply SUS and ZFS iteratively to $\mathcal{K}_{\mathrm{u}}$ until all the UEs are scheduled. It is important to note, that these approaches result in groups of variable size and the number of groups is not known a priori. An overview of the simulated grouping algorithms is given in Tab. 4.1.

Fig. 4.8 shows the sum rate performance of grouping strategies listed in Tab. 4.1. First, we observe that JGS-RS is outperformed by all the other scheduling strategy. While JGS-RS exploits the knowledge of the channel statistics only, all other methods evaluate additional information contained in the instantaneous channel coefficients which leads to performance improvements. Second, it is ev-

ident from Fig. 4.8 that our proposed method (JGS) with the modified SUS algorithm outperforms the original SUS method (G-SUS) for most values of K_{cell}. This is due to the different mechanisms that limit the number of simultaneously served UEs in a group. For G-SUS, the candidate set $\mathcal{K}_{\text{c}}$ is restricted using α and the second criterion $\mathcal{K}_{\text{c}} = \emptyset$ always terminates the algorithm for group member selection. As a consequence, α determines the group sizes for G-SUS. By restricting $\mathcal{K}_{\text{c}}$, the algorithm misses out on some potential candidates that could result in a higher group rate. However, our proposed JGS strategy does not have such a restriction since it selects the group members by means of the improved SUS-M algorithm, and thus demonstrates better performance.

We now compare the performance of JGS to our benchmark approach G-ZFS. From Fig. 4.8 we observe, that G-ZFS leads to small performance improvements over JGS for most values of K_{cell}, which however, comes with the cost of a considerably higher computational complexity. The performance gap between JGS and G-ZFS is due to the different natures of the underlying user selection algorithms and the variable group size resulting from the ZFS selection method. We recall that in JGS, the SUS-M algorithm selects the group members based on channel orthogonality, and adding a new member might harm the group rate. In contrast to this, ZFS always selects the user with the largest contribution to the group rate, and by construction of the algorithm, adding a new user will never deteriorate the group rate. We conclude that our proposed JGS strategy provides the best trade-off between scheduler performance and complexity (for the considered strategies) and it is therefore very suitable for practical systems.

A remarkable observation from Fig. 4.8 is that the sum rate performance of JGS does not increase monotonically with increasing K_{cell}. This is due to the fact that the size of the G-th group is varying. In particular, if K_{cell} is not a multiple of K^*, the last group contains less than K^* members. This results in a high rate for the individual UEs in group G, but degrades the overall sum rate performance. To illustrate this issue, we plot the rates of the individual groups obtained from JGS and JGS-RS in Fig. 4.9a and Fig. 4.9b, respectively. We remark that we chose two extreme cases in Fig. 4.9, since for $K_{\text{cell}} = 316$, group G has only one member, where it has K^* members when $K_{\text{cell}} = 350$. In order to further demonstrate the variations of the individual rates for different values of K_{cell}, we plot the average and the range of the individual UE rates for JGS in Fig. 4.8 as a green line and green shaded area, respectively. We observe that regions (K_{cell} values) corresponding to low sum rates exhibit a larger variation for the UE rates since the last group contains only a small number of UEs, which in turn experience high individual data rates. This reasoning aligns with the observations from Fig. 4.9. For large values of K_{cell}, this effect is less pronounced since the number of groups increases, thereby decreasing the influence of the last group on the overall system performance.

As a last aspect of our studies of JGS, we demonstrate how our proposed algorithm helps to improve the fairness among the users. To this end, we plot the empirical CDF of the individual UE rates in Fig. 4.10 for the different grouping strategies. For a fair comparison of the JGS-based strategies with the iterative application of SUS and ZFS, we investigate the two cases where $K_{\text{cell}} = 316$ (i.e. the last group contains only one UE) and $K_{\text{cell}} = 350$ (i.e. when all groups contain K^* UEs) in Fig. 4.10a and Fig. 4.10b, respectively. Both figures indicate that JGS and JGS-RS provide more fairness among the UEs than G-SUS and G-ZFS since the slopes of the CDFs of the two former strategies are significantly steeper. It is clear that all UEs have very similar rates under JGS and JGS-RS if K_{cell} is a multiple of K^*, as indicated by the absence of the tail of the CDFs for JGS and JGS-Rs in Fig. 4.10b.
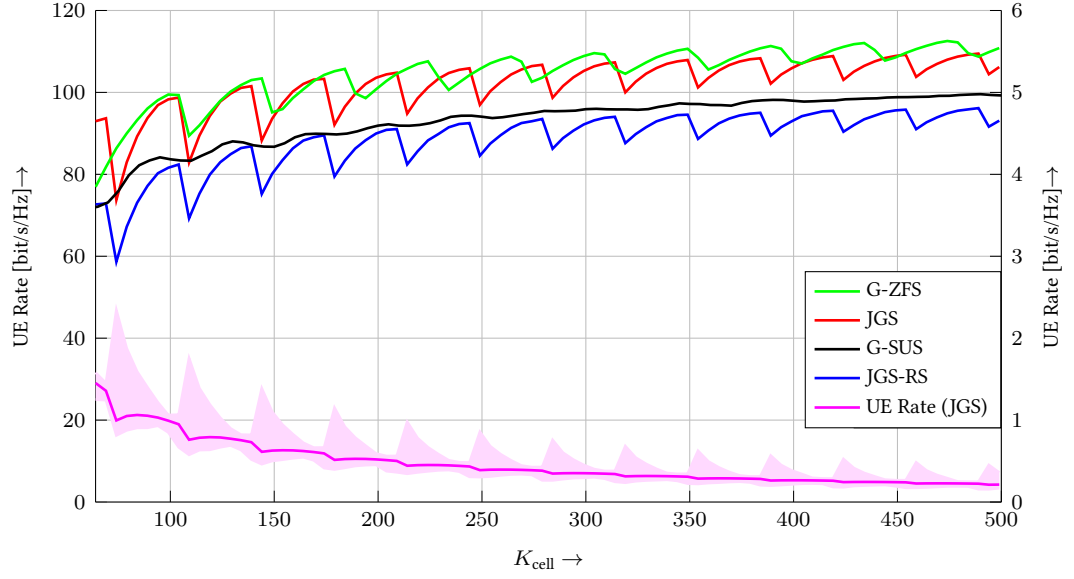
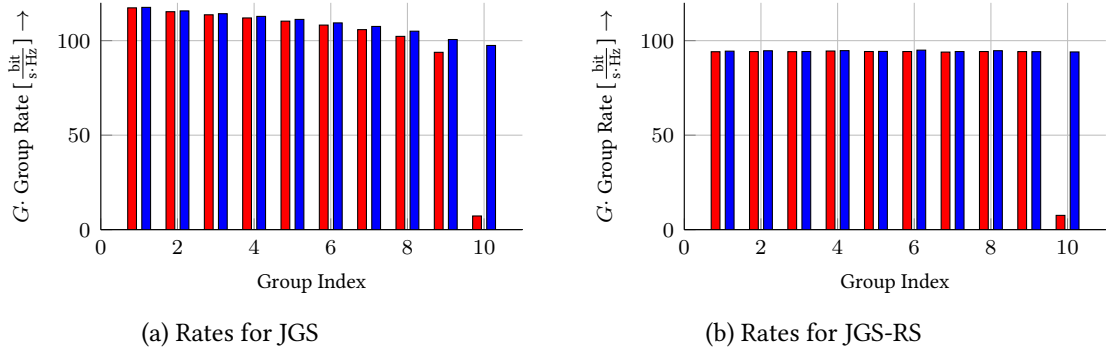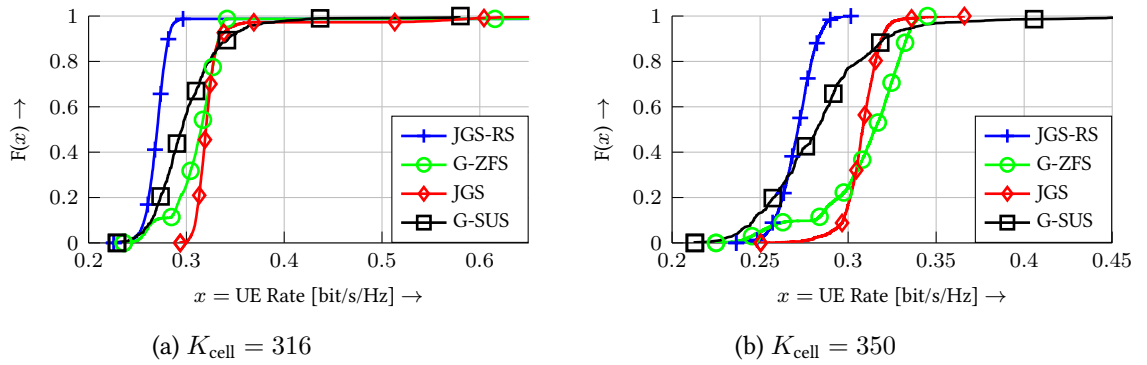Figure 4.8: Sum rate of joint grouping and scheduling algorithm.

(a) Rates for JGS

(b) Rates for JGS-RS

Figure 4.9: Group Rates for $K_{\text{cell}} = 316$ (red) and $K_{\text{cell}} = 350$ (blue).

(a) $K_{\text{cell}} = 316$

(b) $K_{\text{cell}} = 350$

Figure 4.10: Empirical CDF of individual UE rates for different grouping strategies.

4.5 Conclusions

In this last part of our work, we considered the user scheduling problem for massive MIMO IoT systems. We suggested an approach to serve all K_{cell} UEs based on user grouping. To determine the group size, we provided an approximation for K^* for correlated channels based on the Eigenvalues of the UE correlation matrix. To find the group members, we introduced a modified SUS algorithm that overcomes the disadvantages of the conventional algorithm occurring in massive MIMO systems. The presented approach results in a system throughput comparable to the computationally more intensive ZFS-based method and it is thus considered as a scheduling strategy that is very suitable for practical IoT scenarios.

5 Conclusions and Future Work

Massive MIMO transmission is considered a key technique enabling a tremendous performance improvement in future wireless communication networks. The very large number of employed BS antennas, M, in such systems offers various advantages such as increased data rates, higher energy efficiency and support of a large number of users. The promising performance gains offered by the large antenna array at the BS require favourable conditions of the propagation environment which means that the channels of the UEs are rendered orthogonal with growing M. Consequently, a considerable number of devices can be served simultaneously by the BS which makes massive MIMO technology a promising candidate enabling new applications scenarios such as IoT networks, in which a very large number of devices gains access to the wireless communication infrastructure. Recently, however, practical experiments showed that the favourable propagation conditions are not always satisfied in realistic environments, and thus, theoretical performance predictions for massive MIMO systems might not be achievable in real-world applications.

In this work, we studied massive MIMO systems under two different perspectives. The first goal of this thesis was to evaluate the influence of practical propagation conditions on the performance of massive MIMO systems. As a second goal, we wanted to demonstrate the application of massive MIMO transmission as an enabler for IoT scenarios in which a very large number of low data rate devices gain access to the wireless network.

The first part of our thesis is devoted to the performance evaluation of massive MIMO systems under realistic propagation conditions. To provide a better understanding of the topic, we first gave an overview of existing channel models for wireless propagation environments. We introduced the i.i.d. Rayleigh model and the closely-related Clarke model as two popular analytical channel modelling approaches which are often used in theoretical studies of massive MIMO systems. Then, we presented the traditional Kronecker model which allows adjustment of the correlation properties between the channel coefficients. Moreover, we explained the basic structure of the so-called COST 2100 model, a geometry-based stochastic channel modelling approach which has been identified as a suitable model to artificially generate realistic massive MIMO channels. As one main contribution of Chapter 2, we proposed a parameterization of the Kronecker model based on the properties of real-world propagation environments which were observed in practical measurement campaigns available in literature. The second main contribution of Chapter 2, is the comparison of the different channel modelling approaches under massive MIMO configurations in terms of pairwise and joint spatial channel correlation as well as achievable sum rates in the ZFBF downlink. We evaluated the four channel models by means of numerical simulations and compared the three metrics with the values obtained from the measurement campaigns with the following conclusions:

- The i.i.d. Rayleigh model and Clarke's model consistently overestimate the performance of realistic massive MIMO systems in terms of all three parameters as a result of the underlying modelling assumption, which does not involve any correlation among the channel coefficients.

- The COST 2100 tends to deliver inconsistent results when modelling real-world scenarios. Specifically, for a given set of parameters, it does not accurately reflect changes in joint spatial correlation and ZFBF sum rate observed in practical systems over varying M. Furthermore, besides the high computational model complexity, the number of model parameters is very large and a properly chosen parameter set is difficult to obtain from measurement results.

- Our proposed Kronecker model facilitates an accurate and consistent modelling of real-world propagation environments in terms of the three evaluated metrics: pairwise, joint spatial correlation, and ZFBF sum rate performance. Due to the low computational model complexity and the complete characterization by only two parameters, our proposed Kronecker model serves as a suitable approach for simulation of massive MIMO systems under realistic propagation environments.

Our work in Chapter 2 could be extended by the introduction of large-scale parameters in the channel models, which however, would require the conduction of extensive measurement campaigns. As another point of future research, we suggest to tie the correlation parameters used in our model to actual user locations.

In Chapter 3 of this thesis, we examined the effect of different channel models on the performance of massive MIMO channel estimation techniques by means of numerical simulations. We investigated a mix of traditional techniques such as LS and MMSE estimation, and techniques specifically invented for massive MIMO systems such as blind channel estimation. The experiments were conducted in a multi-cell environment in which the training signals are subject to pilot contamination. Our studies showed that the performance of channel estimation techniques derived under massive MIMO systems experience a performance degradation under realistic propagation conditions as a result of the correlation among the channel coefficients. The work in Chapter 3 can be extended in several ways. First, future studies should investigate more parameters, such as varying number of BS antennas, UEs and different UE distributions. Second, it is worth to investigate the influence on the detection accuracy after channel estimation and the influence of the estimation error on the achievable sum rates in the downlink. Moreover, large-scale parameters should also be included in future studies.

In the last part of our work, we investigated the application of massive MIMO systems in IoT scenarios. We considered the fair user scheduling problem in the downlink, and as a main contribution we suggested an approach to serve all K_{cell} UEs based on user grouping. Our approach takes advantage of the fact that typical IoT devices require only low data rates which enables us to split the data transmission interval into sub-intervals and serve several groups of UEs in succession. We proposed to determine the group size based on a large system approximation for correlated channels and select the group members by a modified SUS algorithm. As an important contribution of this chapter, we identified and explained the shortcomings of SUS when applied to massive MIMO systems and suggested an easy modification to the algorithm to overcome its drawbacks. We evaluated our proposed method by means of numerical system simulation and compared its performance with user scheduling approaches available in literature. Our investigations demonstrated that the proposed method significantly outperforms the original iterative application of SUS and performs almost equally as well as the computational more costly ZFS strategy. Furthermore, the new method provides a better fairness among the UEs than the available approaches. As pointers for future research, we suggest to investigate the proposed method under imperfect channel knowledge at the BS. Moreover, the application of widely-linear precoding techniques should be

investigated to further increase the number of UEs supported by this method.

List of Figures

List of Tables

List of Algorithms

Bibliography

[1] A. Zanella, N. Bui, A. Castellani, L. Vangelista, and M. Zorzi, "Internet of things for smart cities," *IEEE Internet of Things Journal*, vol. 1, no. 1, pp. 22–32, Feb 2014.

[2] Erricson, "Cellular Networks for Massive IOT - Delivering New Value in the Networked Society," January 2016, white Paper.

[3] M. R. Palattella, M. Dohler, A. Grieco, G. Rizzo, J. Torsner, T. Engel, and L. Ladid, "Internet of Things in the 5G Era: Enablers, Architecture, and Business Models," *IEEE Journal on Selected Areas in Communications*, vol. 34, no. 3, pp. 510–527, March 2016.

[4] A. Ijaz, L. Zhang, M. Grau, A. Mohamed, S. Vural, A. U. Quddus, M. A. Imran, C. H. Foh, and R. Tafazolli, "Enabling massive IoT in 5G and beyond systems: PHY radio frame design considerations," *IEEE Access*, vol. 4, pp. 3322–3339, 2016.

[5] J. Andrews, S. Buzzi, W. Choi, S. Hanly, A. Lozano, A. Soong, and J. Zhang, "What will 5G be?" *IEEE Journal on Selected Areas in Communications*, vol. 32, no. 6, pp. 1065–1082, 2014.

[6] S. Dama, V. Sathya, K. Kuchi, and T. V. Pasca, "A feasible cellular internet of things: Enabling edge computing and the IoT in dense futuristic cellular networks," *IEEE Consumer Electronics Magazine*, vol. 6, no. 1, pp. 66–72, Jan 2017.

[7] Y. Mehmood, N. Haider, W. Afzal, U. Younas, I. Rashid, and M. Imran, "Impact of massive MIMO systems on future M2M communication," in *Communications (MICC), 2013 IEEE Malaysia International Conference on*, Nov 2013, pp. 534–537.

[8] F. Rusek, D. Persson, B. K. Lau, E. G. Larsson, T. L. Marzetta, O. Edfors, and F. Tufvesson, "Scaling up MIMO: Opportunities and challenges with very large arrays," *IEEE Signal Processing Magazine*, vol. 30, no. 1, pp. 40–60, Jan 2013.

[9] L. Lu, G. Y. Li, A. L. Swindlehurst, A. Ashikhmin, and R. Zhang, "An overview of massive MIMO: Benefits and challenges," *IEEE Journal of Selected Topics in Signal Processing*, vol. 8, no. 5, pp. 742–758, Oct 2014.

[10] T. L. Marzetta, "Massive MIMO: An introduction," *Bell Labs Technical Journal*, vol. 20, pp. 11–22, 2015.

[11] O. Edfors and F. Tufvesson, *D1.2 MaMi Channel Characteristics: Measurement Results*, MAMMOET Std., July 2015.

[12] J. Hoydis, C. Hoek, T. Wild, and S. ten Brink, "Channel measurements for large antenna arrays," in *Wireless Communication Systems (ISWCS), 2012 International Symposium on*, Aug 2012, pp. 811–815.

[13] X. Gao, "Massive MIMO in real propagation environments," Ph.D. dissertation, Lund University, 01 2016.

[14] M. Kuerbis, N. Mysore Balasubramanya, L. Lampe, and A. Lampe, "On the use of channel models and channel estimation techniques for massive MIMO systems," in *24th European Signal Processing Conference (EUSIPCO)*, 2016.

[15] Y. Wang and X. You, "Massive MIMO channel modeling," Master's thesis, Lund University, 2015, student Paper.

[16] M. Ozcelik, N. Czink, and E. Bonek, "What makes a good MIMO channel model?" in *2005 IEEE 61st Vehicular Technology Conference*, vol. 1, May 2005, pp. 156–160 Vol. 1.

[17] S. Krupa. (2016, April) Multichannel fading. Online. Last time accessed: March 24, 2017. [Online]. Available: https://www.slideshare.net/ShreeKrupa1/multichannel-fading

[18] K. Haneda, J. Poutanen, F. Tuvfesson, L. Liu, V. Kolmonen, P. Vainikainen, and C. Oestges, "Development of multi-link geometry-based stochastic channel models," in *Antennas and Propagation Conference (LAPC), 2011 Loughborough*, Nov 2011, pp. 1–7.

[19] J. Poutanen, "Geometry-based radio channel modeling: Propagation analysis and concept development," Ph.D. dissertation, Aalto University, 2011.

[20] K. Zheng, S. Ou, and X. Yin, "Massive MIMO channel models: A survey," *International Journal of Antennas and Propagation*, vol. 2014, 2014.

[21] S. Payami and F. Tufvesson, "Channel measurements and analysis for very large array systems at 2.6 GHz," in *2012 6th European Conference on Antennas and Propagation (EUCAP)*, March 2012, pp. 433–437.

[22] E. Björnson, E. G. Larsson, and T. L. Marzetta, "Massive MIMO: 10 myths and one grand question," *IEEE Communications Magazine*, 2015.

[23] L. Cottatellucci, R. Muller, and M. Vehkapera, "Analysis of pilot decontamination based on power control," in *Vehicular Technology Conference (VTC Spring), 2013 IEEE 77th*, June 2013, pp. 1–5.

[24] E. G. Larsson and B. Q. Ngo, "EVd-based channel estimation in multicell multiuser MIMO systems with very large antenna arrays," in *Acoustics, Speech and Signal Processing (ICASSP), 2012 IEEE International Conference on*, 2012, pp. 3249–3252.

[25] K. Zheng, S. Ou, J. Alonso-Zarate, M. Dohler, F. Liu, and H. Zhu, "Challenges of massive access in highly dense lte-advanced networks with machine-to-machine communications," *IEEE Wireless Communications*, vol. 21, no. 3, pp. 12–18, June 2014.

[26] X. Gao, O. Edfors, F. Rusek, and F. Tufvesson, "Massive MIMO performance evaluation based on measured propagation data," *IEEE Transactions on Wireless Communications*, vol. 14, no. 7, pp. 3899–3911, July 2015.

[27] W. Weichselberger, M. Herdin, H. Ozcelik, and E. Bonek, "A stochastic MIMO channel model with joint correlation of both link ends," *IEEE Transactions on Wireless Communications*, vol. 5, no. 1, pp. 90–100, Jan 2006.

[28] R. H. Clarke, "A statistical theory of mobile-radio reception," *The Bell System Technical Journal*, vol. 47, no. 6, pp. 957–1000, July 1968.

[29] J. Sorensen, E. de Carvalho, and P. Popovski, "Massive MIMO for crowd scenarios: A solution based on random access," in *Globecom Workshops (GC Wkshps), 2014*, 2014, pp. 352–357.

[30] H. Yin, D. Gesbert, and L. Cottatellucci, "Dealing with interference in distributed large-scale MIMO systems: Astatistical approach," *Selected Topics in Signal Processing, IEEE Journal of*, vol. 8, no. 5, pp. 942–953, Oct 2014.

[31] C. Xiao, Y. R. Zheng, and N. C. Beaulieu, "Statistical simulation models for rayleigh and rician fading," in *Communications, 2003. ICC '03. IEEE International Conference on*, vol. 5, May 2003, pp. 3524–3529 vol.5.

[32] L. Hentilä, P. Kyösti, M. Käske, M. Narandzic, and M. Alatossava, *IST-WINNER D1.1.2 WINNER II Channel Models*, Std., 2007.

[33] L. Correia, *Mobile Broadband Multimedia Networks: Techniques, Models and Tools for 4G*. Elsevier Science, 2010. [Online]. Available: https://books.google.ca/books?id=pSOLTRn0B84C

[34] L. Raschkowski, P. Kyösti, and K. T. J. Kusume, *METIS Channel Models*, Std., 02 2015.

[35] X. Gao, F. Tufvesson, and O. Edfors, "Massive MIMO channels - measurements and models," in *Signals, Systems and Computers, 2013 Asilomar Conference on*, Nov 2013, pp. 280–284.

[36] L. Liu, C. Oestges, J. Poutanen, K. Haneda, P. Vainikainen, F. Quitin, F. Tufvesson, and P. Doncker, "The cost 2100 mimo channel model," *Wireless Communications, IEEE*, vol. 19, no. 6, pp. 92–99, December 2012.

[37] X. Gao, O. Edfors, F. Rusek, and F. Tufvesson, "Massive MIMO performance evaluation based on measured propagation data," *CoRR*, vol. abs/1403.3376, 2014. [Online]. Available: http://arxiv.org/abs/1403.3376

[38] J. Medbo, K. Borner, K. Haneda, V. Hovinen, T. Imai, J. Jarvelainen, T. Jamsa, A. Karttunen, K. Kusume, J. Kyrolainen, P. Kyosti, J. Meinila, V. Nurmela, L. Raschkowski, A. Roivainen, and J. Ylitalo, "Channel modelling for the fifth generation mobile communications," in *Antennas and Propagation (EuCAP), 2014 8th European Conference on*, April 2014, pp. 219–223.

[39] J. Flordelis, X. Gao, G. Dahman, F. Rusek, O. Edfors, and F. Tufvesson, "Spatial separation of closely-spaced users in measured massive multi-user MIMO channels," in *IEEE International Conference on Communications (ICC)*. IEEE, 2015.

[40] X. Gao, O. Edfors, F. Rusek, and F. Tufvesson, "Linear pre-coding performance in measured very-large MIMO channels," in *Vehicular Technology Conference (VTC Fall), 2011 IEEE*, Sept 2011, pp. 1–5.

[41] J. Li and Y. Zhao, "Channel characterization and modeling for large-scale antenna systems," in *Communications and Information Technologies (ISCIT), 2014 14th International Symposium on*, Sept 2014, pp. 559–563.

[42] A. O. Martinez, E. D. Carvalho, and J. O. Nielsen, "Towards very large aperture massive MIMO: A measurement based study," in *2014 IEEE Globecom Workshops (GC Wkshps)*, Dec 2014, pp. 281–286.

[43] R. Muller, L. Cottatellucci, and M. Vehkapera, "Blind pilot decontamination," *IEEE Journal of Selected Topics in Signal Processing*, vol. 8, no. 5, pp. 773–786, 2014.

[44] F. Fernandes, A. Ashikhmin, and T. Marzetta, "Inter-cell interference in noncooperative TDD large scale antenna systems," *IEEE Journal on Selected Areas in Communications*, vol. 31, no. 2, pp. 192–201, 2013.

[45] H. Yin, L. Cottatellucci, D. Gesbert, R. Müller, and G. He, "Pilot decontamination using combined angular and amplitude based projections in massive MIMO systems," in *SPAWC 2015, IEEE 8th Workshop on Signal Processing Advances in Wireless Communications, 28 June-1 July 2015, Stockholm, Sweden*, Stockholm, SWEDEN, 06 2015.

[46] A. V. Zelst and J. S. Hammerschmidt, "A single coefficient spatial correlation model for multiple-input multiple-output (MIMO) radio channels," in *URSI XXVIIth General Assembly*, 2002.

[47] S. L. Loyka, "Channel capacity of MIMO architecture using the exponential correlation matrix," *IEEE Communications Letters*, vol. 5, no. 9, pp. 369–371, Sept 2001.

[48] J. Choi and D. J. Love, "Bounds on eigenvalues of a spatial correlation matrix," *IEEE Communications Letters*, vol. 18, no. 8, pp. 1391–1394, Aug 2014.

[49] X. Zhu, Z. Wang, L. Dai, and C. Qian, "Smart pilot assignment for massive MIMO," *IEEE Communications Letters*, 2015, early Access.

[50] T. Vu, T. A. Vu, and T. Quek, "Successive pilot contamination elimination in multiantenna multicell networks," *IEEE Wireless Communications Letters*, vol. 3, no. 6, pp. 617–620, 2014.

[51] N. Shariati, E. Björnson, M. Bengtsson, and M. Debbah, "Low-complexity polynomial channel estimation in large-scale MIMO with arbitrary statistics," *IEEE Journal of Selected Topics in Signal Processing*, vol. 8, no. 5, pp. 815–830, 2014.

[52] H. Yin, D. Gesbert, M. Filippou, and Y. Liu, "A coordinated approach to channel estimation in large-scale multiple-antenna systems," *IEEE Journal on Selected Areas in Communications*, vol. 31, no. 2, pp. 264–273, 2013.

[53] E. G. Larsson, O. Edfors, F. Tufvesson, and T. L. Marzetta, "Massive MIMO for next generation wireless systems," *IEEE Communications Magazine*, vol. 52, no. 2, pp. 186–195, February 2014.

[54] K. Zheng, L. Zhao, J. Mei, B. Shao, W. Xiang, and L. Hanzo, "Survey of large-scale MIMO systems," *Communications Surveys Tutorials, IEEE*, vol. 17, no. 3, pp. 1738–1760, thirdquarter 2015.

[55] O. Elijah, C. Y. Leow, T. A. Rahman, S. Nunoo, and S. Z. Iliya, "A comprehensive survey of pilot contamination in massive MIMO 5G system," *IEEE Communications Surveys Tutorials*, vol. 18, no. 2, pp. 905–923, Secondquarter 2016.

[56] T. Yoo and A. Goldsmith, "On the optimality of multiantenna broadcast scheduling using zero-forcing beamforming," *IEEE Journal on Selected Areas in Communications*, vol. 24, no. 3, pp. 528–541, March 2006.

[57] R. Couillet, S. Wagner, and M. Debbah, "Asymptotic analysis of correlated multi-antenna broadcast channels," in *2009 IEEE Wireless Communications and Networking Conference*, April 2009, pp. 1–6.

[58] T. Yoo and A. Goldsmith, "Optimality of zero-forcing beamforming with multiuser diversity," in *IEEE International Conference on Communications, 2005. ICC 2005. 2005*, vol. 1, May 2005, pp. 542–546 Vol. 1.

[59] S. Dierks and N. Juenger, "Scheduling for massive MIMO with few excess antennas," in *WSA 2016; 20th International ITG Workshop on Smart Antennas*, March 2016, pp. 1–5.

[60] R. Couillet and M. Debbah, *Random Matrix Methods for Wireless Communications.* New York, NY, USA: Cambridge University Press, 2011.

[61] X. Liu and X. Wang, "Efficient antenna selection and user scheduling in 5G massive MIMO-NOMA system," in *2016 IEEE 83rd Vehicular Technology Conference (VTC Spring)*, May 2016, pp. 1–5.

[62] H. Liu, H. Gao, S. Yang, and T. Lv, "Low-complexity downlink user selection for massive MIMO systems," *IEEE Systems Journal*, vol. PP, no. 99, pp. 1–12, 2015.

[63] S. Huang, H. Yin, H. Li, and V. C. M. Leung, "Decremental user selection for large-scale multi-user MIMO downlink with zero-forcing beamforming," *IEEE Wireless Communications Letters*, vol. 1, no. 5, pp. 480–483, October 2012.

[64] G. Dimic and N. D. Sidiropoulos, "On downlink beamforming with greedy user selection: performance analysis and a simple new algorithm," *IEEE Transactions on Signal Processing*, vol. 53, no. 10, pp. 3857–3868, Oct 2005.

[65] S. Huang, H. Yin, J. Wu, and V. C. M. Leung, "User selection for multiuser MIMO downlink with zero-forcing beamforming," *IEEE Transactions on Vehicular Technology*, vol. 62, no. 7, pp. 3084–3097, Sept 2013.

[66] M. Handte, S. Foell, S. Wagner, G. Kortuem, and P. J. Marrón, "An Internet-of-Things enabled connected navigation system for urban bus riders," *IEEE Internet of Things Journal*, vol. 3, no. 5, pp. 735–744, Oct 2016.

[67] A. Khanna and R. Anand, "IoT based smart parking system," in *2016 International Conference on Internet of Things and Applications (IOTA)*, Jan 2016, pp. 266–270.

[68] L. Catarinucci, D. de Donno, L. Mainetti, L. Palano, L. Patrono, M. L. Stefanizzi, and L. Tarricone, "An IoT-aware architecture for smart healthcare systems," *IEEE Internet of Things Journal*, vol. 2, no. 6, pp. 515–526, Dec 2015.

[69] J. Hoydis, K. Hosseini, S. T. Brink, and M. Debbah, "Making smart use of excess antennas: Massive MIMO, small cells, and TDD," *Bell Labs Technical Journal*, vol. 18, no. 2, pp. 5–21, Sept 2013.

[70] L. Zhao, H. Zhao, F. Hu, K. Zheng, and J. Zhang, "Energy efficient power allocation algorithm for downlink massive MIMO with MRT precoding," in *2013 IEEE 78th Vehicular Technology Conference (VTC Fall)*, Sept 2013, pp. 1–5.

[71] C. Kong, C. Zhong, M. Matthaiou, and Z. Zhang, "Performance of downlink massive MIMO in ricean fading channels with ZF precoder," in *2015 IEEE International Conference on Communications (ICC)*, June 2015, pp. 1776–1782.

[72] T. E. Bogale, L. B. Le, and A. Haghighat, "User scheduling for massive MIMO OFDMA systems with hybrid analog-digital beamforming," in *2015 IEEE International Conference on Communications (ICC)*, June 2015, pp. 1757–1762.

[73] G. Lee and Y. Sung, "Asymptotically optimal simple user scheduling for massive MIMO downlink with two-stage beamforming," in *2014 IEEE 15th International Workshop on Signal Processing Advances in Wireless Communications (SPAWC)*, June 2014, pp. 60–64.

[74] J. Mao, J. Gao, Y. Liu, and G. Xie, "Simplified semi-orthogonal user selection for MU-MIMO systems with ZFBF," *IEEE Wireless Communications Letters*, vol. 1, no. 1, pp. 42–45, February 2012.

[75] M. Benmimoune, E. Driouch, W. Ajib, and D. Massicotte, "Joint transmit antenna selection and user scheduling for massive MIMO systems," in *2015 IEEE Wireless Communications and Networking Conference (WCNC)*, March 2015, pp. 381–386.

Eigenständigkeitserklärung

Hiermit erkläre ich, dass ich die vorliegende Arbeit selbstständig und nur unter Verwendung der angegebenen Literatur und Hilfsmittel angefertigt habe.

Stellen, die wörtlich oder sinngemäß aus Quellen entnommen wurden, sind als solche kenntlich gemacht.

Diese Arbeit wurde in gleicher oder ähnlicher Form noch keiner anderen Prüfungsbehörde vorgelegt.

Vancouver, 24. März 2017   _____

                                                                              Unterschrift